GENERATION OF PATIENT-SPECIFIC FINITE-ELEMENT MESH FROM 3D MEDICAL IMAGES

TONG CHENCHEN

(B.Eng.), Huazhong University of Science and Technology

A THESIS SUBMITTED FOR THE DEGREE OF

DOCTOR OF PHILOSOPHY

DEPARTMENT OF BIOENGINEERING

NATIONAL UNIVERSITY OF SINGAPORE

2013

DECLARATION

I hereby declare that this thesis is my original work and it has been written by me in its entirety.

I have duly acknowledged all the sources of information which have been used in the thesis.

This thesis has also not been submitted for any degree in any university previously.

TONG CHENCHEN

August 13, 2013

Acknowledgements

First and foremost I offer my sincerest gratitude to my advisor Prof. Ong Sim-Heng for his support and patience during my PhD candidature. I want to thank him for introducing me to this interesting project, giving me the opportunities to try different things. He gave me a lot of useful suggestions during the process while also allowing me the time and freedom to work in my own way. One simply could not wish for a better and nicer supervisor.

I would also like to thank my coworkers Dr. Yohan Payan and Dr. Marek Bucki from CNRS, France, who provided me with most of the research data. This work is basically completed based on their foundations. I still remember that they came all the way from France to help me start on this project. Although we cannot meet often, they gave me tremendous help throughout the project as well as during the writing of the journal paper. I am grateful for their time and those inspiring instructions and suggestions.

Many thanks go to Dr. Sun Ying for her patient and detailed review of the journal paper. She also gave me a lot of useful suggestions about the paper content and taught me many useful writing skills. I also want to thank Prof. Kelvin Foong Weng Chiong for providing me with the head MR images.

In my daily work I have been blessed with a friendly and cheerful group of fellow students. Many thanks go to them also.

Last but not the least, I would like to thank my family who always support me no matter what. Their love provided my courage and was my driving force. I owe them everything and wish I could show them just how much I love and appreciate them. To my boyfriend who was by my side while I was writing this, I am so lucky to have you in my life. Thank you for your encouragement and accompanying me along this journey.

Contents

Summary

Fast and automatic finite element (FE) mesh generation remains an important issue for patient specific biomechanical modeling in clinical applications such as computer assisted planning and computer aided surgery. While some techniques make automatic mesh generation possible, in most existing procedures, patient image segmentation is required, which is tedious and time consuming. We present a novel patient-specific FE mesh morphing scheme which automatically generates patient-specific FE mesh from patient medical images without resorting to image segmentation. The proposed method is an extension of existing surface or landmark registration based FE mesh morphing methods. Within our scheme, a robust anisotropic filtering strategy with automatic parameter value selection is also proposed to effectively de-noise and enhance the magnetic resonance (MR) image.

MR images are often corrupted by severe Rician noise, which should be removed before they can be used in our image registration based FE mesh generation scheme. In this thesis, we present a general strategy for AD filtering of MR images using an automatic parameter selection method. The basic idea is to estimate the parameters through an optimization step on a synthetic image model, which is different from traditional analytical methods. This approach can be

easily applied to more sophisticated diffusion models for better de-noising results. We conducted a systematic study of parameter selection for the AD filter, including the dynamic parameter decreasing rate, the parameter selection range for different noise levels, and the influence of the image contrast on parameter selection. The proposed approach was validated using both simulated and real MR images. The model image generated using our approach was shown to be highly suitable for the purpose of parameter optimization. The results confirm that our method outperforms most state-of-the-art MR image de-noising methods in both quantitative measurement and visual evaluation. By testing on real images with different noise levels, we demonstrated that our method is sufficiently general to be applied to a variety of MR images.

To extend current surface or landmark registration based FE mesh morphing methods, we propose to automatically generate patient-specific FE meshes by deforming an atlas FE mesh using a 3D transformation derived from patient-to-atlas image registration. This brings patient-specific FE mesh generation one step closer to full automation by skipping the tedious and often difficult image segmentation step. The approach utilizes intensity information in the images to achieve a more accurate anatomical representation and, furthermore, it can be easily adapted to multi-modal imagery. To reduce the distortion caused by the mesh deformation, an effective smoothness term is also proposed in our scheme. By testing the proposed method on 3 different clinical cases with totaling 36 patients datasets involving synthetic image, mono-modal image and multi-modal image registration, we demonstrated that our method is sufficiently general to be used in differently clinical situations. Our method successfully generated patient-specific FE meshes for all cases within minutes, and achieved

sub-millimetre representation accuracy with less than 2% degradation in mesh element quality. Results show that our method outperforms state-of-the-art surface-based mesh morphing methods in both mesh representation accuracy and quality.

List of Tables

LIST OF TABLES

List of Figures

LIST OF FIGURES

Chapter 1

Introduction

The thesis describes an approach for the automatic generation of patient-specific FE mesh from 3D medical images of different modalities, which includes image and atlas mesh pre-processing as well as mono-modal and multi-modal image registration based mesh morphing. Section 1.1 briefly introduces the motivation for the automatic generation of patient-specific FE mesh. The scope and contributions of the thesis are highlighted in Section 1.2. Section 1.3 gives an overview of the organization of this thesis.

1.1 Motivation

FE models are physical models that are widely used to represent the geometrical and mechanical behaviors of human organs. They were first introduced to the medical imaging field mainly for the purpose of research and education. FE models can be used to better understand and validate a given surgical treatment, to model physiological behaviors and to provide virtual simulators for

clinicians. In these frameworks, models are limited to a single generic model for each study (the terminology "atlas" is often used). More recently, applications in the domain of computer assisted planning and computer aided surgery have boosted the need for patient-specific FE models representing the geometry of modeled organs reconstructed from patient medical image data, such as computed tomography (CT) or magnetic resonance imaging (MRI).

In computer assisted planning, FE models are used to predict the outcome of certain surgery routines. For instance, in total knee arthroplasty, prosthesis placement can be optimized to avoid periprosthetic femoral fracture using FE analysis of the stresses within the tissues (Zalzal *et al.*, 2008). In Chabanas *et al.* (2003); Luboz *et al.* (2005), the FE analysis is used to predict the soft tissue deformations resulting from bone repositioning in maxillofacial surgery. Aesthetic and functional consequences of bone positioning can be evaluated pre-operationally with the aid of the FE model.

In computer guided surgery, FE models are often used to compensate for the intra-operative deformation of the soft tissue, e.g., the brain or liver, or to acquire real time feedback of the stress in the implant. In Lengsfeld *et al.* (2005), FE analysis is used to optimize femoral stem placement so as to minimize internal stresses and maximize the implant lifetime. In brain and liver surgery (Cash & Miga, 2005; Castellano-Smith *et al.*, 2001), FE models are used to deform the pre-operative tomography to obtain an intra-operative tomography which can provide the accurate location of tumor after the tissue deformation introduced by surgical intervention.

In these clinical applications, a generic FE model cannot model the morphological diversity across patients, and thus cannot provide accurate FE analyses

for each patient. Therefore, patient-specific FE models adapted to each patients organ geometry are required. The organ geometry is often obtained from patient 3D medical images, such as CT or MRI.

Technically the generation of patient-specific FE mesh from patient medical images can be divided into two stages: (1) patient organ geometry segmentation and (2) volume mesh generation. First, organs should be delineated from the medical images by means of manual, semi-automatic or automatic segmentation techniques that extract the shape information (3D points, contours and/or surfaces) necessary for the generation of the FE mesh representing the volume of the organ. Then a volume mesh is generated based on this geometry. For both segmentation and FE mesh generation phases, manual intervention is often required, which can make this procedure time consuming and tedious. If the mechanical features of sub-structures need to be incorporated into the model, the process could be even more complicated. The sub-structures and sub-regions should also be manually identified or segmented, and the mesh be manually refined to accurately model the mechanical behavior of these sub-structures. This hinders the application of FE analysis in real clinical situations where the pre- or intraoperative time window or clinician availability to perform these delicate tasks is limited.

Although some methods have been proposed for automatically generating patient-specific mesh from the segmented patient organ surface, i.e., the second step as described above, there are very few methods that are sufficiently general to automatically segment different patient organs from different image modalities. Correspondingly, research aimed at complete routine of automatic generation of patient-specific FE mesh from patient medical image is not well

established.

1.2 Scope and Contributions

The aim of the thesis is to propose a methodology to realize image segmentation and patient FE mesh generation in a single step rather than sequentially. In addition, we hope the complete single step routine will considerably simplify the way each step has been independently considered up to now. The goal is to achieve highly accurate and high quality patient-specific mesh generation directly from 3D medical images for different organs, which require minimal user intervention.

Based on the generalist and automatic requirements, patient-specific FE mesh generation methods can be categorized into three levels:

1. Methods generating patient-specific FE mesh based on segmented patient's geometrical features (landmarks, 3D surface or 3D binary images). Most existing methods fall into this level (see details in Section 2.2).

2. Methods generating patient-specific FE mesh from 3D medical images without segmentation, where the imaging modality is restricted, i.e., for a certain FE model, a specific patient image modality is needed. This method improves the level 1 methods by eliminating the tedious and time consuming image segmentation step.

3. Methods generation patient-specific FE mesh from 3D medical images without segmentation, where different imaging modalities can be used. This type of method is more flexible than level 2 methods, as it allows clinicians to

choose the appropriate image modality according to each patient's situation. An important merit of this method comes from substituting the need for patient CT image with patient MR image, thus, avoiding ionizing radiation (associated with CT imaging) for the subject.

In the above categories, the methods in each level are more advanced and demanding than the previous one. Most existing automatic FE mesh generation methods belong to level 1. The framework in this thesis is designed to fulfill the requirements for all these three levels, while the main focus is on level 2 and level 3.

To achieve the requirements in level 2, i.e., automatic generation of patient-specific FE mesh from patient images without segmentation, a novel image registration based mesh morphing scheme is proposed. The method can be seen as an extension of the state-of-the-art surface registration based mesh morphing method (Bucki *et al.*, 2010). We assume that a handmade generic/atlas FE mesh of the organ has already been designed by a biomechanician (see details in Section 2.2.4). Our method automatically generates the patient-specific FE mesh by deforming the atlas mesh using a 3D transformation derived from patient to atlas image registration. This method achieves patient organ segmentation and mesh generation simultaneously, as the geometry of the patient organ will be automatically delineated by the final external surface of the generated patient FE mesh. A C^1-diffeomorphic non-rigid transformation is used in our scheme to maintain a high level of smoothness inside the FE mesh so that the mesh elements after registration will not be distorted by the matching procedure. A new smoothness constraint is also proposed to avoid excessive distortion caused by the deformation. Our method is implemented with an efficient optimization

scheme that does not depend on the similarity metric, and thus can be easily extended to multi-modal image registration.

For the above scheme to work properly, an underlying assumption is that the atlas mesh should be well aligned with the atlas image. A point to surface registration method is proposed to align the atlas mesh with the atlas image and to reduce the surface representation error of the atlas mesh. To preserve mesh regularity, a multi-level diffeomorphic free form deformation is used.

To achieve the requirements in level 3, i.e., allowing different patient image modalities to be used, the patient's medical images need to be pre-processed to remove noise. Compared with CT images, MR images are of lower resolution and significantly noisier (see details in Section 2.3.2). Thus, we propose a robust AD filtering framework for MR image denoising with an optimization-based parameter selection strategy. The optimal parameter values for the filter are automatically selected on a synthetic image model with pseudo ground truth extracted from the real medical images. Results show that the proposed method outperforms state-of-the-art MR denoising methods in both noise reduction and image detail preserving. Combining this pre-processing method with the mesh generation scheme described above, our method can successfully generate patient-specific FE mesh through multi-modal image registration.

To validate the general applicability and robustness of the proposed scheme, we apply the proposed mesh generation scheme to three different clinical cases, each corresponding to a category of the problems described above. A total of 36 patient datasets involving two different organs are included in our experiments, this is, to our knowledge, the first time that an image based mesh morphing scheme has been applied to a diverse clinical database including synthetic,

mono-modal and multi-modal image cases at the same time. A quantitative study on the effectiveness of the proposed smoothness constraint is also presented, which provides useful insight for the parameter value selection in future clinical applications.

To summarize, this thesis makes the following contributions toward automatic patient-specific FE mesh generation:

1. An effective AD filtering framework with automatic parameter selection scheme for MR images denoising and enhancing before they can be used in the mesh generation.

2. An automatic atlas FE mesh calibration and refinement scheme to reduce the matching error between the external surface of atlas mesh and the organ surface in the atlas medical image.

3. A comprehensive patient-specific FE mesh generation method based on volume image registration. This innovative approach incorporates traditional image segmentation and mesh generation procedures into a single step, thus, avoiding the tedious and time consuming image segmentation step. An effective smoothness constraint is also proposed to preserve the quality of the generated mesh.

4. Three routines are proposed to solve three different real clinical cases, i.e., cases with synthetic, mono-modal and multi-modal images, which together constitute a complete solution for using our method to generate patient-specific FE mesh in different clinical scenarios.

1.3 Thesis Organization

Chapter 2 present the background knowledge about the finite element model, the medical image modalities involved in this dissertation as well as a brief review of the image registration techniques. Related works on automatic patient-specific FE mesh generation are also reviewed. Chapter 3 describes how we handle the noise in MR images before they can be used in our mesh generation procedure. Chapter 4 presents a patient-specific FE mesh generation scheme based on image registration. Chapter 5 presents the point to surface registration scheme used to calibrate and refine the atlas mesh. The approaches for applying our scheme to three different clinical cases are presented in Chapter 6, each case corresponding to a category of problems that we wish to solve as described in Section 1.2. Chapter 7 concludes this thesis.

Chapter 2

Background

This chapter provides the background for automatic patient-specific FE mesh generation. Section 2.1 introduces some basic knowledge about the principles of finite element (FE) models and their clinical applications, as well as the criteria used to evaluate the patient-specific FE mesh. Section 2.2 reviews existing patient-specific FE mesh generation method by classifying them into three categories, namely, the standard manual generation method, the automatic mesh generation method and the mesh registration method. The advantages and limitations of each category of methods will be discussed. As we wish to develop an image based FE mesh morphing method, existing image based model deformation methods are also reviewed. Since the proposed scheme is image registration based, basic knowledge about the medical image modalities that are often used to generate patient FE meshes are introduced in Section 2.3. Finally, a brief review of popular medical image registration techniques is presented in Section 2.4.

2.1 Finite Element Model

Before discussing FE mesh generation methods, we first introduce some basic knowledge about the FE model. The basic theory of the FE model is presented in Section 2.1.1. The application of FE models in clinical applications is briefly introduced in Section 2.1.2. Section 2.1.3 presents the factors that affect numerical and mechanical properties of the FE mesh that should be considered for designing the FE mesh generation scheme.

2.1.1 Principles of FE Model

To model the mechanical behavior of an actual physical system, it is idealized or simplified into a mechanical model. The mechanical model is an abstraction of the physical reality with irrelevant physical details "filtered out". This mechanical model is then solved using numerical simulations. To make the numerical simulation practical, it is necessary to reduce the degrees of freedom to a *finite* number. This process is called discretization. The finite element models (FEM) is a dominant discretization technique used for such a purpose.

The basic concept in the physical FEM is the subdivision of the mathematical model into disjoint (non-overlapping) components of simple geometry called *finite elements* or *elements* for short. The response of each element is expressed in terms of a finite number of degrees of freedom characterized by the value of an unknown function, or functions, at a set of nodal points or *nodes*. The response of the mathematical model is then considered to be approximated by that of the discrete model obtained by connecting or assembling the collection of all elements. An example of a human face FE mesh is shown in Fig. 2.1.

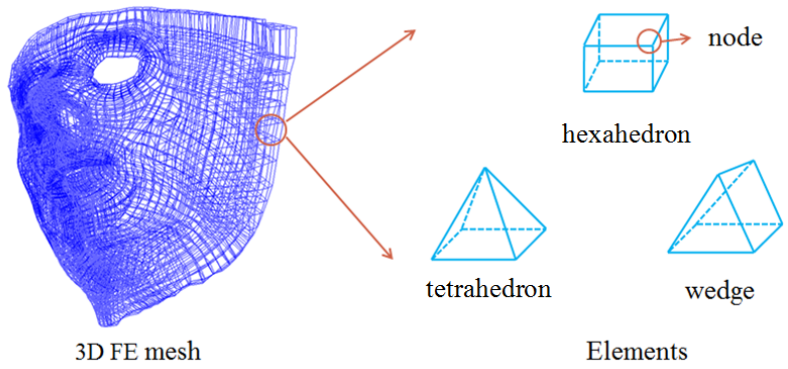

Figure 2.1: Example of human face FE mesh.

By defining appropriate material information and boundary conditions for this mesh, it can be used to simulate the mechanical behavior (deformation, stress, displacement, etc.) of the human face.

The element in the FE mesh may have different geometries, which is often referred to as "element types". In the 3D FE model, the most common shapes are the tetrahedron, pentahedron (also called wedge or prism), and hexahedron (also called cuboid or "brick"), as shown in Fig. 2.1. All these elements are linear elements, i.e., the spacing between the element nodes is linearly interpolated. Higher order elements can also be used such as the cubic Hermite meshes (Zienkiewicz & Taylor, 2000), which has become a popular choice for simulation of heart mechanics (Kerckhoffs *et al.*, 2009; Niederer *et al.*, 2010; Wang *et al.*, 2009). The element type used to build the FE mesh should be selected according to applications. However, generally speaking, hexahedral elements are preferred over tetrahedral elements because of numerical considerations (Benzley *et al.*, 1995) as well as on the fact that for incompressible materials, e.g., face tissue and brain, a 4-node tetrahedral with linear shape functions tends to lock and become overly stiff (Hughes, 1987).

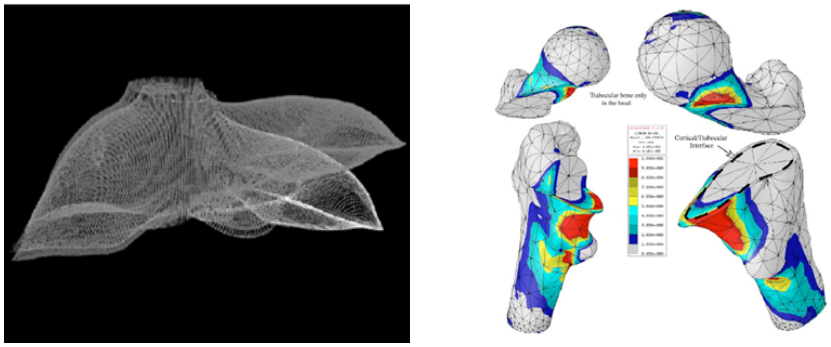

(a) (b)

Figure 2.2: Examples of FE models used in clinical applications. (a) Liver FE mode is used intra-operation to model liver deformation under surgical intervention (Cash & Miga, 2005). (b) Femur FE model is used to asses the stress in the femur neck under certain load (Yosibash *et al.*, 2007).

2.1.2 FE Model in Clinical Applications

FE models can be used in clinical applications to simulate the deformation, stress and displacement of the patient organ under certain surgical routines (examples are shown in Fig. 2.2). Thus, as aforementioned (Section 1.1), they have become a promising tool in computer assisted surgery planning (pre-operative) and image guided surgery (intra-operative). From the FE mesh generation perspective, these two applications do not differ significantly, as the patient-specific FE meshes are often generated pre-operatively by using pre-operative medical images. Compared to pre-operative medical images, patient data acquired intra-operatively is sparse and less accurate. Although generating patient-specific FE mesh from the intra-operative data is possible (Bucki *et al.*, 2010), in intra-operative applications, the patient FE mesh are often generated pre-operatively and then aligned with the patient by using the sparse patient data acquired during the operation (Carter *et al.*, 2005).

2.1.3 FE Model Adequacy

In this section, we introduce the criteria to evaluate the adequacy of the FE mesh, which can then be used to evaluate different FE mesh generation methods.

2.1.3.1 Representation Accuracy

As aforementioned, the FE model is an abstraction of a real physical system, e.g., the patient organ in clinical applications. The more accurate it models the geometrical and mechanical properties of the original object, the more accurate the simulation results that will be obtained from this model. The representation accuracy of the FE model can be assessed from the following aspects:

1. Geometry accuracy. The external surface of the FE mesh should accurately match the external geometry of the patient organ.

2. Control over element types. As mentioned in Section 2.1.1, different element type have different degrees of freedom; thus, for more accurate representation, substructures in the mesh can be assigned with specific element types according to their mechanical properties.

3. Control over element number. The FE mesh can be made finer in regions where more accuracy is required, and coarser elsewhere to achieve a fast and accurate simulation. For example, for the face model in Fig. 2.3, the mesh is made finer in the lips and mouth region, which also subject to complicated movements.

4. Element labeling. Elements in the mesh can be labeled and assigned with specific mechanical properties and group actions to better simulate substruc-

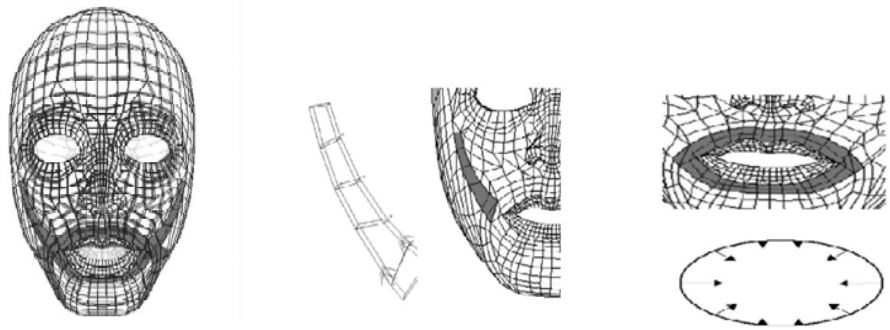

Figure 2.3: Example of a human face FE model with manual substructure refinements (Chabanas *et al.*, 2003).

tures in the organ. For example, in the face model in Fig. 2.3, some elements around the mouth are labeled as muscles and assigned with specific actions.

5. Layer construction. Elements in the mesh can be grouped into layers with non-constant thickness. For example, in the face model in Fig. 2.3, the elements are grouped into two layers; a thin layer represent the dermis, while a thicker layer represents the hypodermis.

The first criterion, i.e., the external geometry accuracy, is the most important requirement for all FE mesh generation methods. Although it may vary across applications, generally, sub-millimeter accuracy is required. Among these representation accuracy criteria, criteria 2-5 are called substructure refinements. To achieve this refinements, regions associated with anatomical sub-structures inside the 3D FE mesh should be identified (e.g. the ventricles, the tumor and the hemispheres of the brain FE mesh proposed by Wittek *et al.* (2007)). These subregions are then associated with specific element types and boundary conditions. In real clinical applications, the patient-specific FE mesh with substructure refinements is preferred for better representation of patient-specific geometries

and mechanical properties and for providing accurate prediction of surgical outcomes. For example, the study in Miga *et al.* (1999) demonstrated that brain substructures played important roles when predicting brain shift.

2.1.3.2 Invalid and Poor Quality Elements

Apart from representation accuracy, the regularity of the FE mesh is also important in evaluating the adequacy of the FE meshes. Both automatic meshing techniques (Knupp, 2000b) and mesh morphing techniques (Section 2.2.4) can generate an FE mesh with *invalid* or *poor quality* elements which will make FE analysis impossible (Luboz *et al.*, 2005) or lead to lower accuracy (Field, 2000; Kwok & Chen, 2000; Shewchuk, 2002). Hence, it is important that FE mesh generation methods generate patient-specific FE meshes with as few such elements as possible. If unavoidable (which is true of most of the cases for the mesh morphing method), these elements should be identified and corrected by a post-preprocessing step. In this section, we explain the concepts about the invalid and poor quality elements. The details of qualitative evaluation and correction of these elements are presented in Section 4.5.

As mentioned earlier, in the framework of the FE method, the response of the mechanical model is approximated by the summation of numerical integration on each element of the mesh. To simplify this integration, a reference element with regular shape is defined in a reference parent coordinate system (Zienkiewicz & Taylor, 1989), i.e., with coordinates (ξ_1, ξ_2, ξ_3) in the range $[-1, 1]$ or $[0, 1]$. For each element of the mesh, the numerical integration is performed in the reference element, then mapped back to the actual element using a mapping function F that maps coordinates (ξ_1, ξ_2, ξ_3) in the reference parent

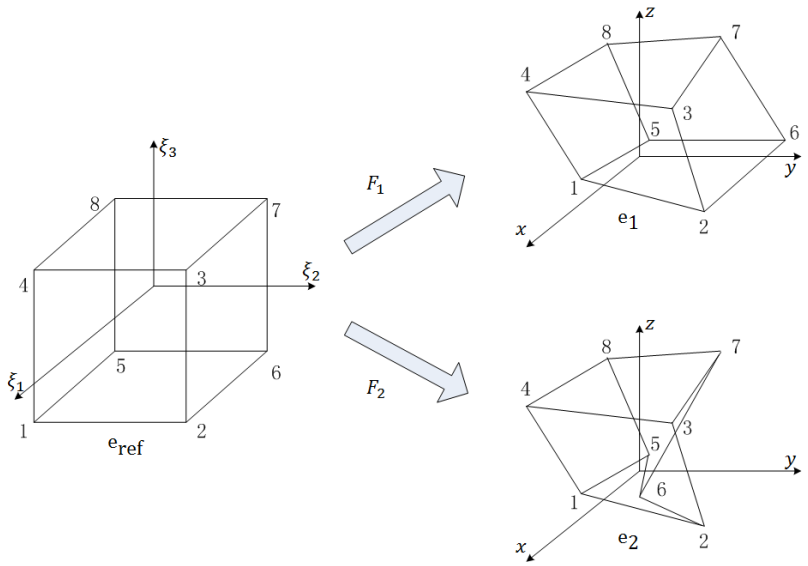

Figure 2.4: Shape function F_1 maps reference parent coordinates (ξ_1, ξ_2, ξ_3) to the actual coordinates (x, y, z) of element e_1. Shape function F_2 cannot be calculated due to distortions of element e_2.

system to the actual coordinates of the element (x, y, z), as shown in Fig. 2.4.

FE analysis cannot be carried out on a FE mesh if it is not possible to define a mapping function F that maps the reference element to any element e of the underlying mesh, as show in Fig. 2.4. Mathematically, that happens when the Jacobian matrix J of the mapping function F is singular, i.e., the determinant of the Jacobian matrix $|J|$ (often referred to as Jacobian value) is equal to zero. The Jacobian value inside an element is calculated by interpolation between its values on each node of the element. Hence, it is never zero if its value on each node has the same sign and is not equal to zero. Thus, the condition for element "regularity" is that the Jacobian value remains strictly positive at each node of the element. If not, the corresponding element is considered "irregular" or "invalid", and thus, by extension, the entire FE mesh is also "invalid".

The Jacobian value measures the distortion of the actual mesh element with

respect to its reference configuration at a given point but does not carry overall distortion information. Thus, the element "quality" is defined to measure the conformity of the element shape, which reflects the evenness of the discretization of the modeled domain. There is a great variety of quality measures and their relevance is dependent on the considered element type and computations to be carried out (Field, 2000; Kwok & Chen, 2000; Lobos *et al.*, 2007; Shewchuk, 2002), among which the Jacobian Ratio (JR) (Kwok & Chen, 2000) is a popular quality measure for FE meshes made of hexahedra and wedges.

2.2 FE Mesh Generation

In this section we first introduce the standard procedures for FE model generation (Section 2.2.1), then focus on the mesh generation step. We present a review of existing patient-specific FE mesh generation methods by classifying them into three categories (Section 2.2.2 to Section 2.2.4). Since the scheme proposed in this thesis is similar to the idea in image based model deformation, related works are also reviewed and compared to illustrate the rationality for us to choose the mesh generation scheme proposed in this thesis (Section 2.2.5).

2.2.1 Standard Procedures

The generation of FE model often consists of three steps:

1. The organ segmentation and reconstruction step. In this step the external surface of the organ of interest is extracted from the patient's medical images by using manual or automatic segmentation methods. In order to generate the

FE mesh with substructure refinements (Section 2.1.3.1), the inner surface for substructures should also be segmented, for example, the ventricle in the brain model or the muscles in the face model.

2. The 3D meshing step. A volume mesh with inner nodes is generated to match with the extracted external surface or landmarks. Substructure refinements can be included if necessary (Section 2.1.3.1).

3. The material assignment step. In this step each element of the mesh is assigned with specific mechanical properties based on the underlying tissue type.

Automatic medical image segmentation is a challenging task because it involves highly variable objects that have to be extracted from images of very low quality (noise, intensity inhomogeneities, and low contrast). Although extensive methods have been proposed in this area, this is no general method that can automatically segment different organs. Thus, currently, the segmentation step has becoming a bottleneck for the automation of patient-specific FE mesh generation. For the material assignment step, traditional methods include manual assignment according to average experimental values or automatically inferring from CT values (especially for bone tissue) (Taddei *et al.*, 2004). Detailed discussion about the image segmentation and material assignment steps are out of the scope of this thesis. In the following sections, we focus on the second step, i.e., the 3D FE mesh generation. Reviews are presented on existing manual or automatic FE mesh generation methods.

2.2.2 Manual Meshing

Manually building a mesh is the optimal method. Although some automatic FE mesh generation methods have been proposed, manually built meshes are still preferred in clinical applications (Chabanas & Payan, 2000; Chabanas *et al.*, 2003; Luboz *et al.*, 2004; Nazari *et al.*, 2008; Wittek *et al.*, 2007) mainly for two reasons. First, it is important to be able to identify sub-regions associated with anatomical sub-structures inside the 3D FE mesh and associate them with specific constitutive behaviors and boundary conditions (as described in Section 2.1.3.1). Second, manual meshing method can easily use hexahedral elements and control their distribution over the mesh. For example, in Nazari *et al.* (2008), a face FE model made of hexahedra and wedges are manually constructed, where the elements are grouped into 3 layers representing different tissue types, and the elements associated with muscles are identified and assigned with specific actions.

However, this method is usually limited to one specimen due to the prohibitive amount of manual labor and time required to build the mesh. For example, building a face FE model as described above can take weeks or even months. Thus, it is not practical to generate patient-specific FE meshes using this method, since both time and expert availability to perform this task is limited in clinical application.

2.2.3 Automatic Meshing

To quickly and automatically generate patient-specific FE meshes, some automatic mesh generation (AMG) methods have been proposed in the past few

years. Based on a 3D surface mesh representing the external geometry of the organ, these algorithms produce an unstructured volume mesh, i.e., sub-structures in the organ are not labeled and element in the mesh is evenly distributed.

The most commonly used AMG method is the tetrahedral meshing method, which generates a volume mesh made of 3D tetrahedra. This method is commonly used by most commercial FE packages. One of the most common approaches for tetrahedral mesh generation has been the Delaunay method (Weatherhill & Hassan, 1994). One limitation of this approach is that it allows tetrahedra to possess exceedingly small dihedral angles. Another tetrahedral mesh generation method is the iterative approach proposed by Ferrant *et al.* (2000). This method covers the object of interest with tetrahedra and systematically subdividing those on the boundary. The disadvantage of this method is that it produces a mesh with low resolution. A physics based mesh deforming technique was proposed by Molina *et al.* (2003). The region of interest is first covered with adaptive sized tetrahedra. A force is then applied to push the boundary nodes close to the known boundary. Based on above basic methods, improvements aimed at constructing tetrahedral meshes with sub-structures have been proposed (Fang & Boas, 2009; Lederman *et al.*, 2011; Mohamed & Davatzikos, 2004; Zhang *et al.*, 2005, 2008).

However, in real clinical applications, the hexahedral mesh is preferred over the tetrahedral mesh as mentioned earlier. Some attempts have been made to automatically generate hexahedral meshes. One is the "voxel mesh" method proposed by Keyak *et al.* (1990), which directly converts voxels into hexahedral elements. This method can avoid the segmentation step, but will often result in huge number of elements and abrupt changes in shape. An alternative method

has been proposed by Viceconti *et al.* (2004), which is based on grid projection. This method is able to model organs with complex shapes and has been applied to different organs. Some application oriented automatic hexahedral mesh generation methods have also been proposed (Creane *et al.*, 2010; Crouch *et al.*, 2007; Shim *et al.*, 2007), but these methods are not sufficiently general to be extended to other organs.

The application of automatic mesh generation methods in real clinical applications is restricted because of the following reasons. First, manually assembled FE meshes are preferred in clinical applications as they can provide better control over element number, types and organization in sub-regions. Second, the hexahedral structure of the FE mesh is preferred over the tetrahedral mesh method for both numerical and FE analysis consideration. In contrast to tetrahedral mesh generation, where Delaunay based approaches are widely used, hexahedral mesh generation is much more difficult and, to our knowledge, no generally applicable method has been presented in the open literature for living tissues. Most importantly, most of these methods require a well-defined 3D organ surface to work properly, e.g., sharp edges, holes or self-intersecting surfaces will cause difficulties. On the other hand, medical image segmentation rarely produces high quality models, making it hard to connect segmentation and FE mesh generation. It should be mentioned that all these methods, even the commercial ones, require knowledge in FE meshing, which can be demanding for clinicians.

2.2.4 Mesh Morphing

In order to overcome the above restrictions of FE mesh generation in real clinical application, a number of methods called "mesh morphing techniques" were recently proposed (Bucki *et al.*, 2010; Couteau *et al.*, 2000; Fernandez *et al.*, 2004; Sigal *et al.*, 2008). This method is designed to combine the merits of both the manual mesh generation method and the automatic mesh generation method as described above. The idea is to start from a manually designed atlas FE mesh which includes sub-region information and manual refinements. This mesh is then automatically deformed to patient data using 3D landmarks, contours or surfaces that were extracted from the patient's medical images. In this way, the methods can benefit from manual design inherited from the atlas mesh while automatically generating patient-specific FE meshes. Meshes generated using this kind of methods yield an accurate representation of the shape of the patient's organ and even of its sub-structures while maintaining the topology - i.e., the element layout - of the manually designed atlas mesh. This kind of method can tolerate imperfect or even incomplete 3D surfaces caused by segmentation or image acquisition, which otherwise may cause problems in automatic mesh generation methods.

The mesh registration method was first described by Couteau *et al.* (2000) as the mesh-matching algorithm. In their method, a full structured atlas mesh is first generated manually. Then, the surface nodes of the atlas FE mesh are deformed by minimizing their Euclidean distances to the patient organ surface segmented and reconstructed from CT or MRI images. The resulting transformation of the external nodes is interpolated to form the 3D transformation

field for the inner nodes of the atlas FE mesh. Finally, the atlas FE mesh is deformed using this 3D transformation to generate a patient-specific FE mesh. This method has been validated on 10 proximal human femora, and has been shown to gain satisfactory results.

In Sigal *et al.* (2008), the authors proposed two methods to register the atlas FE mesh to the patient data. For the first surface based method, the surfaces of the patient and the atlas organs are both segmented from the volume data and wrapped to an "auxiliary" surface which is selected as a "convenient shape". In this way, a correspondence between the patient and atlas surfaces can be obtained. The 3D displacement field is found by interpolation of the surface displacement. The second mesh registration method proposed in this article is based on manually selected landmarks. The transformation is found by registration of these landmarks.

One potential problem of the mesh registration method is that the atlas mesh quality after registration can be greatly reduced when the morphing algorithm induces excessive spatial distortions. This will result in the inability to maintain the regularity of some elements, which prevents FE analysis from being carried out. The second consequence of the morphing method is that the shape quality of the elements is decreased in some regions of the template mesh, which leads to lower accuracy in the numerical simulation. To address this problem, Bucki *et al.* (2010) extended the method in Couteau *et al.* (2000) by introducing regularity constraints for the deformation field and adding a mesh repair step that can restore the validity and quality of the distorted elements without too much change in the position of the registered nodes. This so called "MMRep" has been applied to both bone and soft tissue.

Recently, methods combining both mesh morphing and automatic mesh generation has been proposed, such as the one by Ji *et al.* (2011), which first rigidly registers patient 3D surface to the atlas surface, then automatically generates the volume mesh for the registered patient surface using the same script for generating the atlas mesh, and finally transforms the generated mesh back to the patient coordinates using the reverse transformation. In this way, it eliminates the need to tune the meshing parameters for every patient.

The above surface or landmark based mesh registration methods share a common limitation that a pre-segmentation step is still needed in the scheme. This step can be complicated and challenging for some anatomical structures as mentioned above. Moreover, some organs may have inner intensity differences (e.g., face muscles directions in the MR images) which can be used to achieve a more accurate volume registration. For the surface registration method, the information contained inside the object are lost. The displacement field of the inner nodes is only inferred from the interpolation, which makes the matching of inner sub-regions less accurate.

2.2.5 Image Based Model Deformation

What could be improved in the above mesh morphing methods is to use the full volumetric patient data instead of the landmarks or surfaces extracted to drive the atlas mesh deformation. Instead of deforming the atlas mesh to fit the segmented surface, it could be directly deformed to fit the features in the patient medical image. This will help avoid the previous complicated segmentation step. Moreover, all the information in the patient image can be used to achieve

a better sub-structural registration. In this section, we review existing image based model deformation methods that may be applied to the FE mesh morphing scheme.

Based on the deformation strategy, the existing image based model deformation methods can be classified into two categories: methods that deform a shape by (1) deforming the embedding space of the shape or (2) by modifying their parameters or the degrees of freedom (DOF). Deforming a shape by deforming the embedding space can be qualified as a *registration approach*, whereas modifying the parameters of a shape can be qualified as a *deformable model approach*.

2.2.5.1 Deformable Model Approach

For the deformable model method, the shape of the generic surface is directly optimized under the influence of external and internal forces. This is often done by updating the position of the vertex of the surface mesh according to the forces applied to it. The external force, also called the image force, is derived from the image features (such as edges and region statistics, etc. (Delingette, 1999; Herbulot *et al.*, 2006; Montagnat *et al.*, 1999)) and drives the deformable model toward the apparent boundary of the object of interest. The internal forces are the smoothness constraints and shape prior constraints (Foulonneau *et al.*, 2009; Leventon *et al.*, 2000; Montagnat & Delingette, 2005; Tsai *et al.*, 2003) which can keep the model from been trapped into local minima or develop into arbitrary shape due to lack of local image information.

The geometrical representation of the models is of significant importance in the deformable model method. The most popular representation methods

include level-set, spline surface and simplex mesh. The spline based active contour method (also called "snake") was first proposed by Kass *et al.* (1988). It represents the contour or surface using locally controlled spline functions. Among the splines used, the most widely used is the B-spline (Menet *et al.*, 1990). B-splines can represent smooth surfaces with a high level of geometric continuity. However, this method does not tolerate surface topological change (surface splitting and merging) when evolving. Thus, a method called the level-set was proposed (Malladi *et al.*, 1995; Osher & Sethian, 1988), which instead of representing the moving surface parametrically, represents the surface implicitly using a higher level function. In this way, the moving surface can split and merge while the level set remains a function. Both the spline and the level-set models are continuous. Recently, a discrete model called simplex mesh has become popular. It was first proposed by Delingette (1999), and further studied by Ballester *et al.* (1998) and Montagnat & Delingette (1997). It represents the surface using discrete vertices with constant connections, the main advantage being that it allows simple definitions of smoothness constraints and shape priors (Delingette, 1999).

Although successful in automatic image segmentation, the deformable model method mainly works on surface mesh deformation. Thus, it cannot generate a 3D transformation field that can be used to deform the volume FE mesh at the same time. The sequential process of traditional segmentation followed by 3D mesh generation is still required. This method only uses the local image information close to the boundary of the object. The intensity information inside the volume such as the muscles and other substructures is not used, and thus, cannot achieve an accurate registration for the inner nodes of the FE mesh.

2.2.5.2 Registration Approach

Another method to deform a model to the patient image is the registration approach as mentioned above. The basic idea of this method is to embed the model into a reference image, and then register the reference image to the patient image using intensity based non-rigid registration. The transformation field resulting from the registration is used to deform the reference model. This kind of problem can be categorized as a inter-subject image registration problem, which is used in atlas-based automatic segmentation of the heart (Li & Sun, 2009; Lorenzo-Valdés *et al.*, 2002; Wei *et al.*, 2011; Zhuang *et al.*, 2008a,b) and brain atlas-based automatic segmentation (Cachier *et al.*, 2001; Chen *et al.*, 1999; Guimond *et al.*, 2001; Hellier *et al.*, 2001; Rueckert *et al.*, 2001; Wu *et al.*, 2006).

In Lorenzo-Valdés *et al.* (2002), a method is proposed to automatically segment and track the myocardium and the left and right ventricles using 4D MR images. In this method, an atlas cardiac image is first built based on manual segmentation. Then the atlas image is registered with the patient-specific MR image by using a B-spline free-form deformation method. In this way, the labels on the atlas image can be propagated to the patient image, thus completing the segmentation.

Similarly, Wei *et al.* (2011) proposed a method to automatically segment the late gadolinium enhanced (LGE) cardiac MR images. The fact is that the segmentation of the cine MR image is fairly easy and automatic methods already exist, while the segmentation of LGE images is much more difficult due to intensity inhomogeneities. Thus, they proposed to first automatically segment the

myocardial structures in the cine image, and then propagate the contour in the cine MR image to the LGR image of the same patient by registering the cine image with the LGR image using B-spline free-form deformation.

Although the non-rigid registration methods used in these papers are different for specific applications, there are two common methods which are often used to either solve the problem or compare with the proposed new methods: the B-spline free-form deformation (FFD) method (Rueckert *et al.*, 1999) and the Demons method (Thirion, 1998). These two methods are widely used because they can compensate for large deformations between different patients and they both can produce diffeomorphic deformations. The similarity metric used in these methods are SSD, SAD and NCC for mono-modality, and NMI for both mono-modality and multi-modality. These transformations and metrics will be discussed in detail in Section 2.4.

This image registration based model deformation method can produce a 3D transformation field that can be directly used to deform the volume FE mesh. Compared to the deformable model approach described above, this method can provide a more accurate registration for the inner nodes of the FE mesh, as all the substructure information in the atlas and patient image is used to derive the transformation. Thus, this method better suits the objectives of the image based FE mesh generation that we want to develop in this thesis.

2.3 Medical Image Modalities

Medical imaging is the technique and process used to create images of the human body non-invasively for clinical purposes (medical procedures seeking to

reveal, diagnose, or examine disease). The major modalities that are often used in clinical diagnoses are projection X-ray (radiography), X-ray computed tomography (CT), the nuclear medicine imaging methods of single-photon emission computed tomography (SPECT) and positron emission tomography (PET), ultrasound, and magnetic resonance imaging (MRI). They each have their own specialties, advantages and limitations. Among all these methods, CT and MRI are the most often used image modalities for 3D modeling. Other modalities generate in 2D image (ultrasound, X-ray), or have relatively low resolution and not directly related to anatomical structures (SPECT, PET). Thus, in this section we introduce some basic knowledge about the CT and MRI modalities which can be used to generate patient-specific FE mesh.

2.3.1 Computed Tomography

CT imaging is basically X-ray imaging in 3D. It uses computer-processed X-rays to produce cross-section images (slice) of the human body. By moving the scanner along an axis and imaging at a constant step rate, it can produce a series of 2D image slices. These images are then stacked together to form a volume image of the object of interest. The intensity value of the CT image shows the X-ray intensity reduction (attenuation) when going through the tissue at the corresponding location. As different tissues often have differently attenuation coefficients, the body structures can be distinguished in the CT image. Fig. 2.5(a) shows a sample of a CT slice.

Although CT can image bone, soft tissue and blood vessels, all at the same time, it provides better details for the bony structures than for soft tissues. A

(a) (b)

Figure 2.5: Examples of CT and MR head images. (a) A sample slice of CT image of the head. (b) A sample slice of MR image of the head.

CT scan can usually be completed within 5 minutes, with the actual scan time usually less than 30 seconds. The main advantage of CT over MRI is in imaging bones and structures with air such as the lungs. It can also be used on patients who have received certain types of surgical clips, metallic fragments, cardiac monitors or pacemakers and thus cannot receive an MRI. A main disadvantage of CT imaging is the radiation exposure to the patient. The effective radiation dose from CT ranges from 2 to 10 mSv, which is about what a person receives from background radiation in 3 to 5 years.

2.3.2 Magnetic Resonance Imaging

MRI makes use of the property of nuclear magnetic resonance (NMR) to image nuclei of atoms (in particular, hydrogen nuclei, ^{1}H contained in water) inside the body. A magnetic field with a spatial gradient is applied to the human body which is used to align the magnetization of the atomic nuclei. Then radio frequency magnetic fields are applied to systematically alter the alignment of

this magnetization. This causes the nuclei to emit a rotating magnetic field detectable by the scanner. As the frequency of the signal emitted by the nuclei is proportional to the magnetic field applied on it, the spatial gradient of the magnetic field can be used to recover the location of the signal. Protons in different tissues return to their equilibrium state at different relaxation rates. Different tissue variables, including spin density, T_1 and T_2 relaxation times, and flow and spectral shifts, can be used to construct the MRI images. The collected data is reconstructed into a 2D slices of images through any axis of the body, as shown in Fig. 2.5(b).

Compared to CT, MRI gives much higher detail in the soft tissues. However, bones lack water and therefore appear as black regions. An MRI scan typically runs for about 30 minutes, which makes it more sensitive to movements such as those due to breathing. One of the greatest advantages of MRI is the ability to highlight different tissue types. Another advantage is the ability to change the imaging plane without moving the patient. The main limitation of MR is that it involves a strong magnetic field, which makes it unsuitable for patients with cardiac pacemakers, tattoos and metal implants.

Besides the above limitations, another problem with the MR image is that it is of lower resolution compared to CT, and often corrupted by severe noise, as shown in Fig. 2.5(b). Different from the commonly encountered Gaussian noise (such as found in CT images) which simplifies the denoising process, the noise in MR images follows a Rician distribution (Gudbjartsson & Patz, 1995). The noise in MRI image is primarily due to thermal noise, which appears as complex Gaussian white noise in the acquired MRI signal. The usual reconstruction procedure of the acquired MRI signal is to use the discrete Fourier transform (DFT).

After the DFT reconstruction the value of each pixel is complex. Both the real and the imaginary components of the pixel value again follow a Gaussian distribution with variance σ_n. The magnitude of the MRI signal is the square root of the sum of the squares of Gaussian distributed real and imaginary parts, and thus, the noise in MR image follows a Rician distribution. In the low intensity part, the Rician noise tends to a Rayleigh distribution, while in high intensity regions it approaches a Gaussian distribution. This not only makes the image noisy, but also reduces contrast of the image, as the estimated mean of the image is biased by the noise distribution. This noise should be removed before further processing of the MR images.

2.4 Medical Image Registration

Detailed reviews of medical image registration methods can be found in several papers (Hajnal & Hill, 2010; Maintz & Viergever, 1998; Shen *et al.*, 2005). In this section, we only provide a review of the registration methods that are related to the FE mesh generation scheme presented in this thesis. Image registration is the process of aligning two images by transforming the position of a feature in one image to the position of the corresponding feature in another image. The transformation is often found by minimizing/maximizing a similarity metric that measures the current alignment accuracy of the two images. In this section we review the medical image registration methods from both the similarity metric and transformation method aspects.

2.4.1 Similarity Metrics

As we would like to develop an intensity based mesh morphing method, we focus on intensity based similarity metrics. These metrics can be classified into two categories: mono-modal similarity metrics which can only register images of the same modality, and multi-modal similarity metrics which can register images of the same or different modality.

2.4.1.1 Mono-modal Similarity Metrics

Minimizing intensity difference. One of the simplest intensity based similarity metric is the sum of squared intensity differences (SSD). For voxel locations x_A in image A, within an overlap domain $\Omega^{\mathbf{T}}_{A,B}$, comprising voxels:

$$\text{SSD} = \frac{1}{N} \sum_{x_A \in \Omega^{\mathbf{T}}_{A,B}} \left| A(x_A) - B^T(x_A) \right|^2, \tag{2.1}$$

where x_A is the voxel position, A is the target image and B is the source image. The transform is $\mathbf{T}$. The SSD metric is widely used for serial MR registration, for example by Hajnal *et al.* (1995), and in the widely used statistical parametric mapping (SPM) software (Ashburner & Friston, 1999). It is the optimum metric when two images only differ by Gaussian noise. However, SSD cannot be used in inter-modality registration. Even for the intra-modality registration, the requirement of this metric is too strict, e.g., the noise in MRI does not follow Gaussian distribution and there will be some changes in the content of the two images. Additionally, SSD is very sensitive to small numbers of pixels which have large intensity differences. One improved version of SSD is the sum of

absolute difference (SAD), which is less sensitive to "outliers" in the image:

$$\text{SAD} = \frac{1}{N} \sum_{x_A \in \Omega^{\mathbf{T}}_{A,B}} \left| A(x_A) - B^T(x_A) \right|. \tag{2.2}$$

Normalized cross correlation (NCC). This is obtained by measuring the correlations of the intensities in the corresponding location of the two images within the overlapped domain. If the two images are well aligned, the correlation between them should be large. Thus, we can find the best alignment by maximizing this metric:

$$\text{NCC} = \frac{\sum_{x_A \in \Omega^{\mathbf{T}}_{A,B}} (A(x_A) - \bar{A}) \cdot (B(x_A) - \bar{B})}{(\sum_{x_A \in \Omega^{\mathbf{T}}_{A,B}} (A(x_A) - \bar{A})^2 \cdot \sum_{x_A \in \Omega^{\mathbf{T}}_{A,B}} (B(x_A) - \bar{B})^2)^{\frac{1}{2}}}. \tag{2.3}$$

NCC requires the intensities of the two images to follow a linear relationship. This requirement is less strict than SSD or SAD. Another advantage of this metric is that the correlation can be carried out in both spatial domain and K-space. With K-space, the transform can be solved quickly without using any iterative method, but the "linear relationship" is still too strict for multi-modality registration.

2.4.1.2 Multi-modal Similarity Metrics

Image registration can be described as trying to maximize the amount of shared information in two images. Using this concept, registration can be thought of as reducing the amount of information in the combined image, which suggests the use of a measure of information as a registration metric. The most commonly used measure of information is the Shannon-Wiener entropy measure H (Shan-

non, 1949):

$$H = -\sum_{i} p_i \log p_i. \tag{2.4}$$

H is the average information supplied by a set of i symbols whose probabilities are given by $p_1, p_2, p_3, \ldots, p_i$. We can see that when the probability distribution of the i symbols is flat, the information metric H is large. When the probability distribution of the i symbols is concentrated in some value, the information metric H is small. The following three metrics are all based on this assumption, and differ only in how they deal with the overlap problem.

Joint Entropy (JE). The joint entropy of image A and B is given by:

$$H(A, B) = -\sum_{a}\sum_{b} p_{AB}^{\mathbf{T}}(a, b) \log p_{AB}^{\mathbf{T}}(a, b), \tag{2.5}$$

where $p_{AB}^{\mathbf{T}}(a, b)$ is the joint probability distribution function (PDF) of image A and B. The number of elements in the PDF can either be determined by the range of intensity values in the two images or from a reduced number of intensity "bins". This metric measures the amount of information we have in the combined image (Hill *et al.*, 1994). As discussed above, the best alignment of two images can be found when minimizing the information in the combined image. Although straightforward, this metric has an important limitation. Since $p_{AB}^{\mathbf{T}}(a, b)$ is dependent on the transform $\mathbf{T}$, there may be a trivial solution that only matches the background of the two images. In this way, all the joint probability is concentrated in $p_{AB}^{\mathbf{T}}(0, 0)$, and thus the joint entropy can be maximized in this condition. However, obviously, this is not the real solution.

Mutual Information (MI). To avoid the overlap problem, instead of just considering the information in the combined image, the information in the two images is also considered. Communication theory provides a technique for measuring the joint entropy with respect to the marginal entropies (Hill *et al.*, 1994), which is known as mutual information:

$$\begin{aligned} I(A,B) &= H(A) + H(B) - H(A,B) \\ &= \sum_a \sum_b p^{\mathbf{T}}_{AB}(a,b) \log \frac{p^{\mathbf{T}}_{AB}(a,b)}{p^{\mathbf{T}}_A(a) \cdot p^{\mathbf{T}}_B(b)}. \end{aligned} \tag{2.6}$$

Mutual information can qualitatively be thought of as a measure of how well one image explains the other, and is maximized at the optimal alignment. The mutual information is first introduced to medical image registration by Maes *et al.* (1997), and Wells *et al.* (1996), respectively. Mutual information has been widely used in multi-modal registration. However, it does not entirely solve the overlap problem, i.e. changes in the very low intensity region within the overlap can disproportionately contribute to the mutual information. Thus, another information theory based metric is proposed, which is the normalized mutual information.

Normalized Mutual Information (NMI). Three normalization schemes have so far been proposed in journal articles. The following two were mentioned by Maes *et al.* (1997):

$$\tilde{I}_1(A,B) = \frac{2I(A,B)}{H(A) + H(B)}, \tag{2.7}$$

$$\tilde{I}_2(A,B) = H(A,B) - I(A,B). \tag{2.8}$$

Studholme has proposed an alternative normalization devised to overcome the sensitivity of mutual information to change in image overlap (Studholme *et al.*, 1999):

$$\tilde{I}_3(A, B) = \frac{H(A) + H(B)}{H(A, B)}. \tag{2.9}$$

The third version of normalized mutual information has been shown to be considerably more robust than standard mutual information.

Besides the metrics based on information theory, another interesting metric named Residual Complexity was proposed recently (Myronenko & Song, 2009). Although not widely used, this metric shows promising results in the registration of images corrupted by the bias field.

2.4.2 Transformation Methods

Transformation methods control the degree of deformation a registration can make. The transforms used to simulate the deformation between different patients are often non-rigid. However, rigid and affine registrations are often used in the first step to compute the global registration, since they are easy to compute and can model large deformations. In this section, we briefly introduce rigid and affine transformations, and focus mainly on non-rigid transformations.

2.4.2.1 Rigid and Affine Transformation

Rigid transformations can be used to register objects which only differ in position, e.g. the bones from the same patient. The rigid transform can model rotation and translation. It is represented using a 4×4 matrix which contains 6 parameters; thus the rigid transformation has 6 DOFs.

Rigid registration can be slightly extended by adding stretch and screw, which becomes the affine transformation. It is represented using a 4×4 matrix which contains 12 parameters; thus the affine transformation has 12 DOFs.

2.4.2.2 Non-rigid Transformation

Transformations more flexiable than affine transformation are called non-rigid or non-linear transformation. They are often represented using a 3D displacement field instead of a single matrix. For each dimension, the displacement field is a function of position. In our image registration based FE mesh generation scheme, the registration method not only needs to accurately match the atlas image with the patient image, but also has to generate a deformation field that is smooth enough to preserve the quality of the deformed FE mesh. Thus, for this review of non-rigid registration, we focus on the method that can provide a diffeomorphic deformation field, i.e., the transformation that will not cause space folding.

B-spline free form deformation (FFD). One of the most popular transformations used in inter-subject registration is the free-form deformation (FFD) method (Rueckert *et al.*, 1999). The FFDs are based on locally controlled functions such as B-splines. The basic idea of FFDs is to deform an object by manipulating an underlying mesh of control points. The resulting deformation controls the shape of the 3D object and produces a smooth and C^2 continuous transformation. The FFD displacement field can be computed by optimizing different kinds of similarity metrics such as SAD and NMI. Some improved versions of the traditional FFD method have been proposed. Schnabel *et al.* (2001) proposed

to use multi-level grids to reduce the computational time and avoid the folding of the displacement field. Later they proposed a diffeomorphic version of the FFD method (Rueckert *et al.*, 2006). Rohlfing & Jr (2001) proposed an incompressible transform by adding an incompressible constraint to the FFD. Glocker *et al.* (2008) proposed to use linear programming to accelerate the optimization, and use the MRF method to avoid local minima.

The strength of the FFD method is that it can be optimized on different similarity metrics, from distance to intensity based ones. It is suitable for different kinds of problems. It is different from the Demons method in that it can match the objects even if they do not overlap at the initial positions. The limitation of the FFD transform is that the degree of deformation is still limited by the intrinsic smoothness constraints in the locally controlled functions like B-splines. Hence, it cannot handle extremely large displacements.

The transformation used in the surface registration based FE mesh generation method (Bucki *et al.*, 2010) is a kind of FFD. It is different from the FFD method in Rueckert *et al.* (2006), in that a locally controlled function other than the B-spline had been used. The similarity metric used in the method is the Euclidean distance. Thus, a straightforward extension of this algorithm would be to use the FFD transform and replace the distance metric with some intensity based similarity metric like the SAD or NMI.

Demons method. Another popular inter-subject registration method is the Demons method which is based on diffusion theory (Thirion, 1998). At each pixel, a velocity (movement) is defined from the intensity differences and gradient information. This velocity field is smoothed (regularized) by a Gaussian filter, and

iteratively used to transform the moving image for registering on to the static image. The intensity information used in the Demons algorithm is the intensity difference and the gradient of the two images. The velocity proposed by Thirion (1998) is:

$$\vec{v} = \frac{(m-s)\vec{\bigtriangledown}s}{(\vec{\bigtriangledown}s)^2 + (m-s)^2}, \tag{2.10}$$

where m and s are the voxel intensity in the moving image and the static image, respectively. $\vec{\bigtriangledown}s$ is the gradient of the static image. The velocity is then composited to the current displacement field $\mathbf{T}_i$ to get the new displacement $\mathbf{T}_{i+1}$:

$$\mathbf{T}_{i+1} = \mathbf{T}_i \circ \vec{v}. \tag{2.11}$$

Based on this, Wang *et al.* (2005) proposed a new velocity function which not only depends on the gradient of the static image but also the moving image:

$$\vec{v} = (m-s) \times \left(\frac{\vec{\bigtriangledown}s}{(\vec{\bigtriangledown}s)^2 + (m-s)^2} + \frac{\vec{\bigtriangledown}m}{(\vec{\bigtriangledown}m)^2 + (m-s)^2} \right). \tag{2.12}$$

This method besides being faster still work when there are missing edges in the static image. Vercauteren *et al.* (2009) proposed a diffeomorphic version of the Demons method.

The strength of the Demons method is that it is faster than the FFD method. Since the displacement of the Demons is directly defined at each voxel, it can compensate for larger displacements than the FFD. The limitation of this method is that it cannot match objects when they are initially not overlapped. Furthermore, the deformation field obtained using this method is less smooth than that of the FFD method.

Besides these two widely used methods, other diffeomorphic registration methods can also be found in the literature (Ashburner, 2007; Avants *et al.*, 2008; Beg *et al.*, 2005; Hernandez *et al.*, 2007).

Chapter 3

Pre-processing for MR Image Denosing and Enhancement

This chapter describes the pre-processing step we applied to the MR volume images to eliminate or greatly reduce the noise level in these images, before they can be used in the volume image registration step. The anisotropic diffusion filter is used as the pre-processing method due to its edge preserving and contrast enhancement ability. We propose a general AD filter framework and an novel automatic parameter value selection scheme. The method is validated on both synthetic and real MR images.

3.1 Introduction

The proposed patient-specific FE generation method is designed to be sufficiently flexible to be applied to CT and MR images. Both of these medical image modalities are widely used in reconstructing 3D organ models, i.e., the

FE models, among which CT is suited for imaging bone structures, while MR is better suited for imaging soft tissues. There are also cases where cross-modality image registration is needed, e.g., where the atlas model is constructed on one image modality while the patient volume image is in another image modality. This is because a specific imaging modality may not be available for every coming patient. For example, in clinical applications, MR imaging is considered safer than CT imaging due to its non-ionizing feature during pregnancy. However, patients with cardiac pacemakers are not allowed to get an MR scan due to the strong magnetic field used.

As mentioned earlier (Section 2.3.2), MR images are often corrupted by severe Rician noise. This will affect the accuracy of intensity based registration, especially those based on intensity differences metrics, such as the sum of absolute differences (SAD). Thus, before volume image registration, we need a robust method to remove the noise in MR images.

Rician noise may be reduced during image acquisition, but this will lead to an unacceptable increase in acquisition time (Gerig *et al.*, 1992). A more practical approach is to apply smoothing filters to the acquired images. The simplest filters are linear filters such as the Gaussian filter (Kosior *et al.*, 2007; Petersson *et al.*, 1999), which are effective but tend to blur object boundaries. Nonlinear filters, such as the anisotropic diffusion (AD) filter of Perona & Malik (1990), significantly reduce noise while simultaneously preserving edges and small features. Some other sophisticated methods such as the wavelet-based filters (Robert & Nowak, 1999) and nonlocal mean filters (Manjón *et al.*, 2008) have been proposed, but AD filtering is still widely used in the pre-processing of MR images because of its efficiency and simplicity in implementation.

The AD filter was first introduced to MR image de-noising by Gerig *et al.* (1992). Although widely used, the result of the AD filter is actually highly dependent on parameter values. There are difficulties in automatically selecting these values, especially for the conductance parameter that controls both the gradient threshold and the edge enhancement range, i.e., it determines which gradient levels are to be smoothed and which are to be enhanced. The first difficulty is that, since the parameters are also related to image contrast, we cannot simply obtain experimental optimal values for different noise levels as proposed in Manjón *et al.* (2008). Secondly, the gradient range of the edges of interest is often quite wide and overlaps with the gradient magnitudes due to noise. Therefore, an optimal threshold cannot be easily identified by examining the gradient histogram or by using other analytical methods. Further, when using Catté's regularized model (Catté *et al.*, 1992), the diffusion result is jointly determined by the conductance parameter and the Gaussian kernel sizes used for regularization. From our experiments, we find that these parameters are intrinsically related and thus cannot be selected separately.

Due to the above difficulties, existing analytical methods for determining the optimal diffusion parameter values have their limitations. In their original paper, Perona & Malik (1990) proposed an automatic method based on Canny's edge detector (Canny, 1986), where the first 80% of the cumulative histogram of the gradient is assumed to be due to noise. In a similar manner, Perona and Malik set the conductance parameter, i.e., the gradient threshold, to be 90% of the cumulative histogram. Later, Monteil and Beghdadi proposed the adaptive nonlinear anisotropic diffusion (ANAD) method (Monteil & Beghdadi, 1999), which extends Perona and Malik's method. Instead of using a constant parame-

ter throughout, they estimate the parameter at every iteration until convergence. Such methods will fail when noise and edge gradient values overlap, which is often the case.

Another widely used automatic method was proposed by Black *et al.* (1998). The assumption is that the noise in an image follows a Gaussian distribution with standard deviation (SD) σ_e. Since the conductance parameter controls the gradient threshold of the AD filter, by letting the gradient threshold equals σ_e, the conductance parameter is related to the noise SD. This was extended by Samsonov & Johnson (2004) to non-uniform noise. The parameter estimated using this method is only dependent on the noise level. However, as mentioned above, the contrast information of the image is also important in selecting the parameters. We also note that the Gaussian noise assumption of these methods is not accurate since the noise in MR images is Rician. Furthermore, the above analytical methods only work with the original diffusion model of Perona & Malik (1990) and cannot be extended to other variational models such as the regularized model (Catté *et al.*, 1992). Hence, the parameters of AD filters are still manually tuned in most applications due to the above limitations.

Recently, a method called scalar Rician noise reducing anisotropic diffusion (SRNRAD) has been proposed (Krissian & Aja-Fernández, 2009). In order to obviates the needs to manually tune the parameters of the traditional AD filter, the author proposed to replace the diffusion function based on image gradient with a function based on local statistics of the image intensity and global statistics the noise. The method is a combination of popular AD (Perona & Malik, 1990) filter and LMMSE estimator (Aja-Fernández *et al.*, 2008). According to the article, the proposed method outperforms most of state-of-the-art MR image

denoising methods in both noise removing and edge preserving aspects. One main drawback of the SRNRAD filter as emphasized in is that it relies on the assumption of a Rician distribution. Thus, for dark regions where the distribution is close to Rayleigh, the noise cannot be fully removed. Moreover, some noise points may even been enhanced. Another limitation of this method is that it does not give consistent performance in 2D images because fewer pixels are involved in the estimation of local statistics.

We propose a robust AD filtering framework for MR image de-noising with an optimization-based parameter selection strategy. The basic idea is to obtain the optimal parameter values on a synthetic image model with pseudo ground truth[1], and then use these values on the real image. We also conduct a systematic study of parameter selection for the AD filter in MR image de-noising, including the rate of decrease of the dynamic parameter model, the initial parameter selection range and the convergence properties.

An advantage of our approach is that it does not depend on analytical methods and hence is applicable to a variety of diffusion models, for example, those with sophisticated diffusion equations and functions for better noise reduction. Our model is fitted to the Rician noise distribution in MR images, whereas the noise is conventionally assumed to be Gaussian. Compared to manual parameter tuning, our approach is more efficient and systematic, with comparable diffusion results. Performance is further validated by testing on a variety of real MR images with different noise levels.

The rest of this chapter is organized as follows. Section 3.2 presents the

[1]A noise free, piecewise constant image is extracted from the noisy image to serve as the ground truth. See Section 3.3.1 for details.

anisotropic diffusion framework and a discussion of the important parameters. Section 3.3 describes the strategy to automatically determine the optimal parameter values. The results of applying the proposed method to both simulated and real MR images are presented and discussed in Section 3.4, followed by the conclusion in Section 3.5.

3.2 AD Filtering Framework

3.2.1 Standard Anisotropic Diffusion Model

The diffusion model was first proposed by Witkin (1983). He observed that the convolution of a signal with the Gaussian kernel σ is equivalent to solving a heat equation with time σ. The heat equation can be expressed as

$$\frac{\partial I(x,t)}{\partial t} = \operatorname{div}\left(D \cdot \nabla I(x,t)\right), \quad I(x,0) = I_0(x), \tag{3.1}$$

where the diffusion conductance D is a constant. The initial condition is set as the original image $I_0(x)$. This method is called isotropic diffusion since it performs the same diffusion on the entire image. A problem of this method is that while reducing noise, it also blurs edges.

To solve this problem, Perona & Malik (1990) proposed an anisotropic diffusion process, which replaces the original constant diffusion conductance with a spatially varying diffusion function

$$D = g\left(|\nabla I|\right), \tag{3.2}$$

where $g(x)$ is a monotonically decreasing function satisfying

$$\lim_{x\to\infty} g(x) = 0 \quad \text{and} \quad g(0) = 1.$$

In this way, the local diffusion conductance is related to local gradient, which is taken to be the edge indicator. By making g a monotonically decreasing function, the new method is able to reduce the diffusion at the estimated edge locations. In their paper, they presented two different diffusion equations:

$$g(|\nabla I|) = \exp\left(-\left(\frac{|\nabla I|}{\lambda}\right)^2\right), \tag{3.3}$$

$$g(|\nabla I|) = \frac{1}{1+\left(\frac{|\nabla I|}{\lambda}\right)^2}, \tag{3.4}$$

where λ, the conductance parameter, determines which gradients are to be smoothed and which are to be preserved.

3.2.2 Variational Models

As stated by Perona & Malik (1990), the original model is not suited to handling noise that is of the same gradient level as the edges. Since our approach is not restricted to specific diffusion models, we incorporate some variations proposed in the literature instead of using the original model described by Eqs. (3.1-3.4).

To avoid enhancing noise, Catté *et al.* (1992) used the Marr-Hildreth method (Marr & Hildreth, 1980) as the edge indicator, i.e., Gaussian smoothing before locating the edges, rather than a simple gradient method. In addition, unlike the original AD equation in Eq. (3.1), it guarantees the uniqueness of the solution.

The modified diffusion equation is

$$\frac{\partial I}{\partial t} = \operatorname{div}\left(g\left(\nabla G_\sigma * I\right)\nabla I\right), \tag{3.5}$$

where I is the image and G_σ is the smoothing Gaussian kernel with variance σ. Since the gradients caused by noise diminish more rapidly than those due to edges, the gradient magnitude of the noise will be significantly reduced after Gaussian smoothing. Thus, noise points are less likely to be treated as edges and preserved in the diffusion process.

For the diffusion function g, we use the one proposed by Weickert (1998):

$$g\left(|\nabla I|\right) = 1 - \exp\left[\frac{-C_m}{\left(\frac{|\nabla I|}{\lambda}\right)^m}\right], \tag{3.6}$$

which fulfills the smoothness requirement of the diffusion process while the original diffusion functions (3.3) and (3.4) do not. λ is the conductance parameter or diffusion coefficient. C_m is a constant chosen to ensure that $g(x) \cdot x$ is monotonically increasing for $x < \lambda$ and monotonically decreasing for $x > \lambda$, making λ the gradient threshold. According to Weickert (1998), $m = 4$ is optimal for most applications.

In addition to these two variations, Whitacker & Pizer (1993) have suggested that the regularization parameter σ in Eq. (3.5) should be a decreasing function of diffusion time, and Li & Chen (1994) have proposed to subsequently decrease the contrast parameter λ in Eq. (3.6). These two modifications are based on the assumption that noise gradient decreases faster than edge gradient. Hence, the parameters are set to larger values initially to significantly reduce noise levels,

and then values are subsequently decreased to preserve and enhance weak edges, thus solving the problem of noise having the same gradient magnitudes as edges. By using the dynamic parameters, the edge enhancement range is also wider (Li & Chen, 1994). A further advantage is that the diffusion process is convergent, thus removing the need to accurately control the diffusion time as in the original model. The dynamic models are:

$$\lambda = \lambda_0 \exp\left(\frac{-t}{\alpha}\right), \tag{3.7}$$

$$\sigma = R\left[\sigma_0\left(1 - \frac{t}{\beta}\right)\right], \tag{3.8}$$

where R is a ramp function defined as

$$R(x) = \begin{cases} x, & \text{if } x \geq 0; \\ 0, & \text{otherwise.} \end{cases} . \tag{3.9}$$

The rate of decrease of the parameters is controlled by α and β. If the parameters decrease too rapidly, noise cannot be fully removed, while too slow a rate will cause the weak edges to be diffused away before they are enhanced. Unfortunately, there is no discussion, in Whitacker & Pizer (1993) and Li & Chen (1994), of how to choose the appropriate rate. In Section 3.4, we propose a suitable decreasing rate for both parameters in MR image de-noising.

The adoption of these three variations to the standard model will facilitate noise removal while preserving weak edges. They will also improve the stability and ensure the uniqueness of the solution.

3.2.3 Parameters to be Determined

In our diffusion model, there are several parameters that significantly influence the results.

λ_0: the initial conductance parameter in Eq. (3.7). It influences the sensitivity of the algorithm to edges. The higher λ_0 is, the stronger the edges that will be diffused. In addition, a higher λ_0 will also provide a larger range for edge enhancement (Li & Chen, 1994).

σ_0: the initial SD of the Gaussian kernel in the regularization process (3.8). It controls the gradient levels to be smoothed in the edge estimation step. Thus, it can also be seen as a gradient threshold.

n : the total diffusion time in Eq. (3.5).

Our objective is to provide a general scheme to automatically determine the optimal parameter values. Since we adopt a dynamic parameter model, the diffusion results will automatically converge and hence the diffusion time no longer needs to be controlled. The two parameters that are left for us to set are the conductance parameter λ_0 and regularization parameter σ_0.

There is no general method to determine appropriate values of these two parameters. Existing automatic methods only analyze the selection of the constant conductance parameter λ. However, since λ and σ both influence the gradient threshold, they jointly determine the diffusion results and cannot be treated separately. As mentioned previously, analytical methods have their limitations. Hence, we propose an alternative approach that is practical and leads to optimal parameter values.

3.3 Parameter Optimization on Synthetic Image Model

Suppose we have a ground truth (noise-free) image, then the optimal parameters are found by minimizing the diffusion error between the filtered image and the ground truth image. However, in practice, the ground truth image is not available. Fortunately, the information needed to determine the parameters is limited. As discussed above, the parameters of AD filters are jointly determined by the contrast information and the noise level, which can be extracted from the real image, even with noise.

We propose to optimize the parameters on a synthetic model generated from the real image. We first extract the contrast information in the image using a noise-robust pre-segmentation method. This will form a piecewise constant noise free pseudo ground truth image. The noise level is estimated from the real image and added to the pseudo ground truth to generate the noisy model image. The synthetic model thus contains all the information needed to determine the AD filter parameters, namely the contrast and noise level. The parameters optimized on this synthetic model should also be near optimal for the real image. The overall flow chart of our strategy is presented in Fig. 3.1.

3.3.1 Extracting Contrast Information

To extract the contrast information from noisy MR images, we use the modified fuzzy C means (FCM) (Ahmed *et al.*, 2002) because of its robustness to noise and bias. The actual method to be employed here is not critical provided it can give a rough classification of the image (see Section 3.4.1.3). In Ahmed *et al.* (2002), the standard FCM is modified by introducing a term that allows

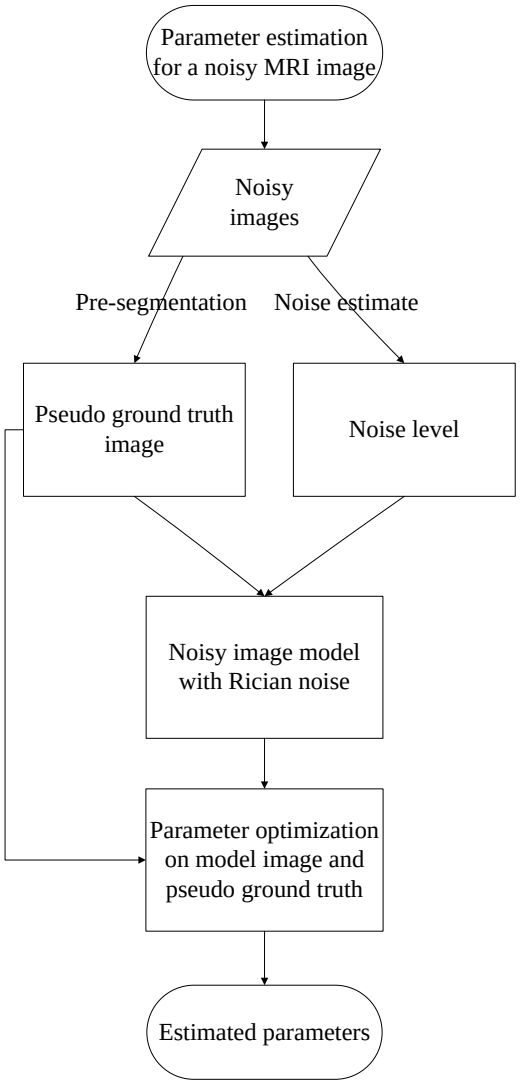

Figure 3.1: Flow chart of the proposed strategy

the labeling of a pixel to be influenced by the labels in its immediate neighborhood. The classification result of a pixel is not only determined by its own intensity but also by the class of its neighbors. This formulation tends to drive the results towards piecewise constant labeling, which increases the robustness to both noise and image inhomogeneity. The modified objective function for partitioning $\{x_k\}_N^k$ into c clusters is given by

$$\begin{aligned} J_m &= \sum_{i=1}^{c}\sum_{k=1}^{N} u_{ik}^p \|x_k - v_i\|^2 + \\ &\quad + \frac{\nu}{N_R}\sum_{i=1}^{c}\sum_{k=1}^{N} u_{ik}^p \left(\sum_{x_r \in N_k} \|x_k - v_i\|^2\right), \end{aligned} \tag{3.10}$$

where $\{v_i\}_i^c$ are the prototypes of the clusters and the array $[u_{ik}] = U$ represent the partition matrix. The parameter p is a weighting exponent on each fuzzy membership and determines the amount of fuzziness of the resulting classification. N_k stands for the set of neighbors around x_k and N_R is the cardinality of N_k. The latter part of the objective function is the newly added neighborhood term. This objective function is minimized when, for each pixel x_k, a high membership value u_{ik} is assigned if its intensity is close to the corresponding cluster center v_i and at the same time its neighboring pixels' intensity values are also close to v_i. The effect of the neighborhood term is controlled by a parameter ν. If the SNR of the image is large, ν should be chosen small as the intensity of a single pixel is reliable. On the contrary, if the SNR is low, ν should be set large to avoid the influence of noise.

With this method, we can obtain a piecewise constant image which contains the general edge information of the original image. The resulting image will

serve as the pseudo ground truth image of the synthetic image model.

3.3.2 Estimating Noise Level

After extracting the contrast information from the image, the next step is to estimate the noise level. According to Gudbjartsson & Patz (1995), the magnitude of the MRI signal is the square root of the sum of the squares of the real and imaginary parts. Since each of these follows a Gaussian distribution with the same standard deviation σ_n, the noise in MR images follows a Rician distribution. The image corrupted by Rician noise is biased, and there exists a simple relationship between the real pixel intensity and the expected pixel intensity of the noisy image (Gudbjartsson & Patz, 1995):

$$A = \sqrt{|M^2 - 2\sigma_n^2|}, \tag{3.11}$$

where A is the real pixel intensity and M is the expected pixel intensity of the noisy image.

Based on the above relationship, Nowak (1999) proposed a simple method to estimate the noise level σ_n. In this method, σ_n is estimated in the background region, for example, the air region surround the body, where $A = 0$. Therefore,

$$\sigma_n = \sqrt{\frac{E\left(I_b^2\right)}{2}}, \tag{3.12}$$

where I_b is the background region. Since a pre-segmentation has already been performed, the background region can be easily extracted. Many other methods can be used to estimate σ_n (Aja-Fernández *et al.*, 2008; Gravel *et al.*, 2004).

Since they generally give similar results, we adopt Nowak's method for convenience.

3.3.3 Synthetic Noisy Image Model

Having extracted the contrast and noise information from the real image, we can now add the noise to the pseudo ground truth image to generate the model noisy image. The Rician noise is modeled by adding Gaussian noise with σ_n to both the real and imaginary parts (Nowak, 1999). The noisy image is obtained by taking the square root of the sum of the squares of these two parts:

$$I_{\text{im}} = N\left(I\cos\theta, \sigma_n^2\right), \tag{3.13}$$

$$I_{\text{re}} = N\left(I\sin\theta, \sigma_n^2\right), \tag{3.14}$$

$$I_{\text{noisy}} = \sqrt{I_{\text{im}}^2 + I_{\text{re}}^2}, \tag{3.15}$$

where I is the pseudo ground truth image, I_{noisy} is the noisy image model, and I_{im} and I_{re} represent the imaginary and real parts, which follow Gaussian distributions. The parameter θ can be chosen to be any angle.

3.3.4 Optimization

We proceed to conduct parameter optimization on the pseudo ground truth image and the synthetic noisy image model. As discussed in Section 3.3.2, the mean value of the noisy image is biased from the ground truth. We should first remove this bias before optimization. Since AD filtering does not change the mean value of the image, a simple method can be derived from Eq. (3.11) to

obtain the bias-corrected image I_{ub} from the diffused image I_{diff}:

$$I_{ub}(x,y) = \sqrt{\left|I_{diff}^2(x,y) - 2\sigma_n^2\right|}, \tag{3.16}$$

Parameter optimization is done by minimizing an error function between the ground truth image I and the bias corrected image I_{ub}. Here, we adopt the commonly used mean square error (MSE) as the error function:

$$\text{MSE} = \frac{1}{N}\sum\left(I_{ub}(x,y) - I(x,y)\right)^2, \tag{3.17}$$

where $I(x,y)$ is the intensity at pixel (x,y) of the pseudo ground truth image and N is the number of pixels in the image. By minimizing MSE, we obtain the optimal parameters for the synthetic image model. As explained earlier, the estimated parameters should also be near optimal for the real images, which is confirmed by our experiments.

3.3.5 Post-processing

After parameter optimization, the diffusion model in Section 3.2 with the estimated parameters is applied to the noisy image. The output image is biased due to Rician noise. We obtain the un-biased output with Eq. (3.16).

We observe that noise in the homogenous regions is effectively removed, but not at the edges. This is because diffusion is prohibited at points with high gradient values. By applying a 3×3 median filter at the final stage for noisy images with $\sigma_n > 5$, we can effectively remove the noise at the edge regions without significant blurring.

3.4 Experimental Resutls

3.4.1 Synthetic Images

To validate our method, we use the simulated MRI volume for the normal brain from BrainWeb (Cocosco *et al.*, 1997). This is a T1 image with 1mm $\times$ 1mm $\times$ 1mm voxel resolution and 8 bit quantization. We conducted the experiments on 181×217 2D slices. The original noise-free data is taken as the ground truth. To simulate the noisy image we add different levels of noise to the original image using the method described in Section 3.3.

3.4.1.1 Parameter Decreasing Rate

The first experiment is conducted to find the proper decreasing rate for the dynamic parameters in Section 3.2, i.e., to select the values of α and β in Eqs. (3.7) and (3.8), respectively. In this experiment, parameters are manually tuned to be optimal. Then, we compare the MSE convergence curve for different decreasing rates. Some examples are shown in Fig. 3.2(a). When α and β are too small, the parameters will decrease too quickly to fully remove the noise, and thus the MSE will be large, as shown by the blue curve in Fig. 3.2(a). However, when α and β are too large, the parameters will decrease too slowly, which will cause over-diffusion (increase in MSE) as shown in Fig. 3.2(a) by the red curve. Therefore, the optimal decreasing rate is chosen such that they give small MSE while not causing over-diffusion. Based on this, we select the parameter values of $\alpha = 10$ and $\beta = 10$. As shown in Fig. 3.2(b), the diffusion results on different noise levels using this decreasing rate do not show any significant over-diffusion.

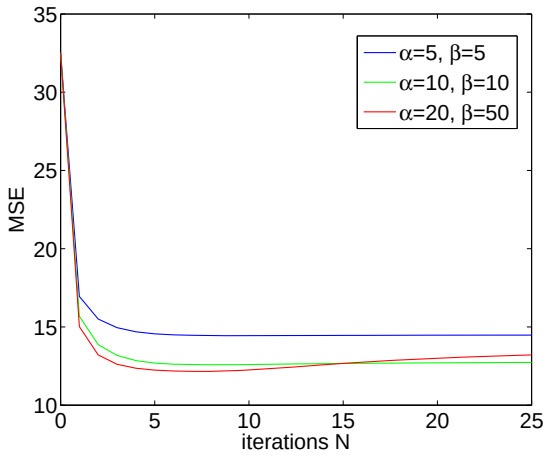

(a)

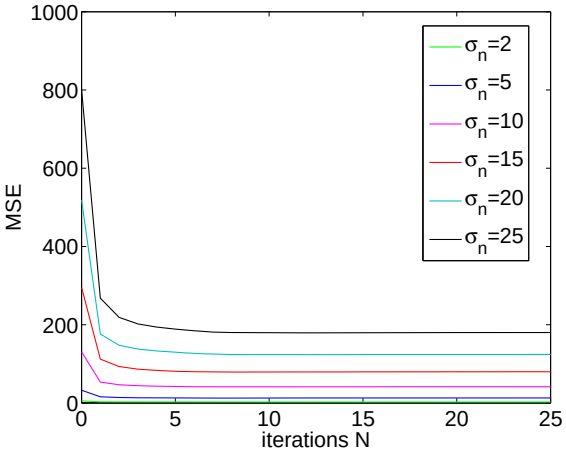

(b)

Figure 3.2: Experiments on dynamic parameter decreasing rate. (a) The MSE convergence curves with different decreasing rates on image with $\sigma_n = 5$. (b) The MSE convergence curves for different noise levels using the decreasing rate $\alpha = 10$ and $\beta = 10$.

For the convergence of our scheme, we refer to Fig. 3.2(b), which shows that for different noise levels, our method converges within 5 iterations.

3.4.1.2 Comparative Study

We also compared our method with state-of-the-art filters for MR image denoising. Specifically, we consider the following methods.

1. Automatic parameter selection anisotropic diffusion (AADM), which is the method proposed in this thesis.

2. Scalar Rician noise reducing anisotropic diffusion (SRNRAD) by Krissian & Aja-Fernández (2009), using parameters suggested by the author.

3. LMMSE estimator proposed by Aja-Fernández *et al.* (2008), using 5×5 windows for filtering and noise estimation.

4. Nonlocal means algorithm (NLM) (Buades *et al.*, 2005), using parameters suggested by Manjón *et al.* (2008).

5. Unbiased nonlocal means algorithm (UNLM) (Manjón *et al.*, 2008), using 11×11 search window, 5×5 similarity window, and parameter $h = 1.2\sigma_n$.

6. The original anisotropic diffusion algorithm by Perona & Malik (1990) (ADPM). The conductance parameter λ is set as 90% value of the histogram of image gradient magnitude as suggested in the original paper.

7. The original anisotropic diffusion algorithm by Perona and Malik, using the parameter selection method proposed by Black *et al.* (1998); Samsonov & Johnson (2004), denoted ADBL. λ is set as $c\sigma_n$, where c is decided according

to the diffusion function used. For the diffusion function used in Perona and Malik's model, $\lambda = 2\sigma_n$.

To quantitatively evaluate the restoration performance of these methods, we used three quality indexes:

1. Mean square error (MSE), which measures the pixelwise difference between the ground truth image and the de-noised image. It is the most often used index for evaluating de-noising performance.

2. Structural similarity (SSIM) index (Wang *et al.*, 2004), which is a structural degradation index. It measures luminance, contrast and structure similarity.

3. Quality index based on local variance (QILV) (Aja-Fernández *et al.*, 2006), which is another structural degradation index. Compared to SSIM, QILV is more sensitive to possible edge blurring rather than the level of noise.

Among these three indexes, MSE measures the overall similarity, SSIM the de-noising ability, and QILV the edge preserving ability. For SRNRAD and LMMSE, since they are only defined for Rician noise distribution, the background is not taken into account in the quantitative measurements.

The quantitative results are shown in Table 6.1 and Fig. 3.3, and the examples of the diffusion results in Fig. 3.4. Generally speaking, the unbiased algorithms perform better than the biased algorithms. The three biased algorithms show very similar results. Among the unbiased algorithms, we note that UNLM is the optimal filter when noise level is low, but it tends to blur the edges at higher noise levels. On the other hand, LMMSE preserves most of the edge information, but at the same time leaves some noise untouched. The scheme

σ_n	Noisy	AADM	SRNRAD	LMMSE	UNLM	NLM	ADPM	ADBL
5	32.52	14.15	14.90	18.43	**7.81**	19.614	39.16	24.00
10	131.65	31.18	38.18	58.23	**22.28**	72.59	87.37	85.47
15	290.60	48.86	62.50	101.96	**47.22**	160.74	165.83	170.02
20	513.70	**76.43**	90.18	150.36	84.09	288.95	291.55	286.53
25	808.85	**108.36**	121.38	205.78	132.80	458.36	436.47	435.50

σ_n	AADM	SRNRAD	LMMSE	UNLM	NLM	ADPM	ADBL
5	0.9768	0.9756	0.9644	**0.9871**	0.8287	0.7984	0.8210
10	0.9569	0.9457	0.8981	**0.9609**	0.7726	0.7554	0.7596
15	**0.9362**	0.9137	0.8402	0.9226	0.7208	0.7200	0.7212
20	**0.9046**	0.8804	0.7769	0.8745	0.6653	0.6848	0.6848
25	**0.8750**	0.8479	0.7196	0.8337	0.6156	0.6553	0.6510

σ_n	AADM	SRNRAD	LMMSE	UNLM	NLM	ADPM	ADBL
5	0.9983	0.9983	**0.9983**	0.9975	0.9947	0.9593	0.9965
10	0.9763	0.9953	**0.9934**	0.9872	0.9703	0.9472	0.9726
15	0.9715	**0.9887**	0.9853	0.9631	0.9131	0.9224	0.9099
20	0.9686	**0.9807**	0.9723	0.9281	0.8285	0.8127	0.8177
25	0.9549	**0.9645**	0.9479	0.8344	0.6690	0.7083	0.6746

Table 3.1: MSE, SSIM, and QILV index for the synthetic image experiments on state-of-the-art methods. The best value for each noise level is highlighted. The proposed sheme (AADM) shows ballanced results in terms of noise removal and edge preservation.

proposed in this thesis (AADM) together with SRNRAD outperforms the other techniques. Both obtain balanced results in noise removal and edge preserving. Our method gives better results than SRNRAD for both the MSE and SSIM, while SRNRAD gives slightly better results in QILV, i.e., in preserving details. From Fig. 3.4, we can see that our method gives diffusion results that are very close to the ground truth image, while the one with SRNRAD is slightly noisy.

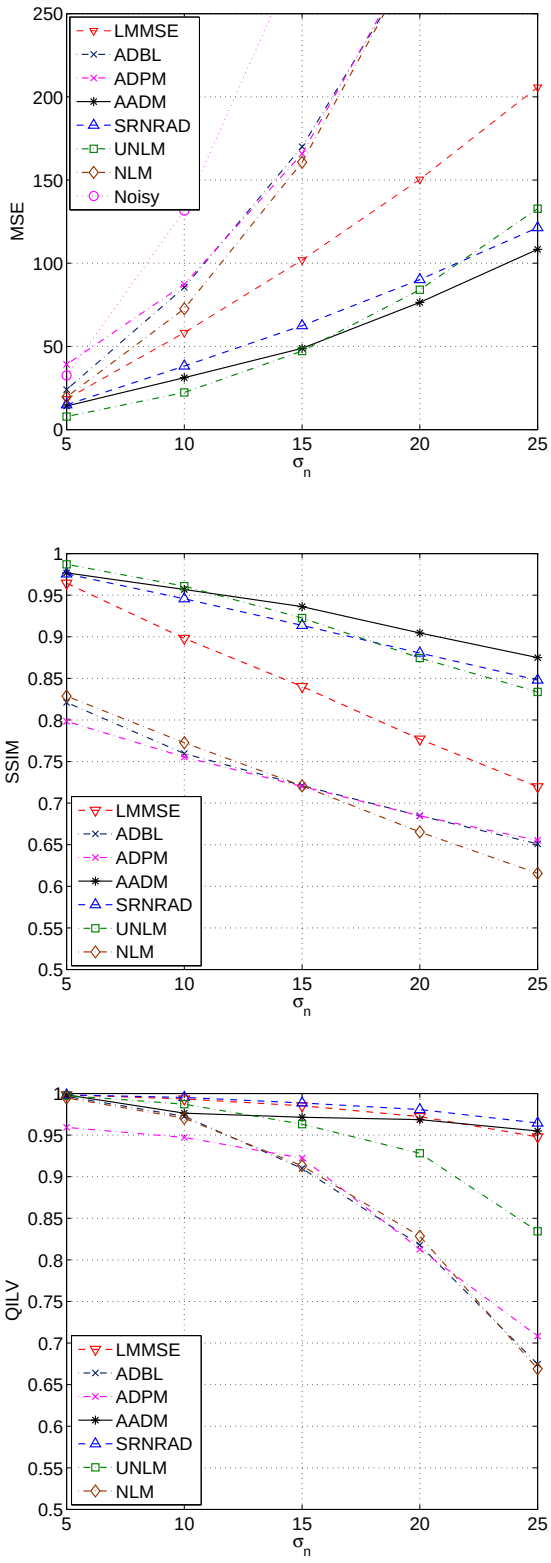

Figure 3.3: MSE, SSIM, and QILV index for the synthetic image experiments on state-of-the-art methods. The proposed scheme (AADM) shows ballanced results in terms of noise removal and edge preservation.

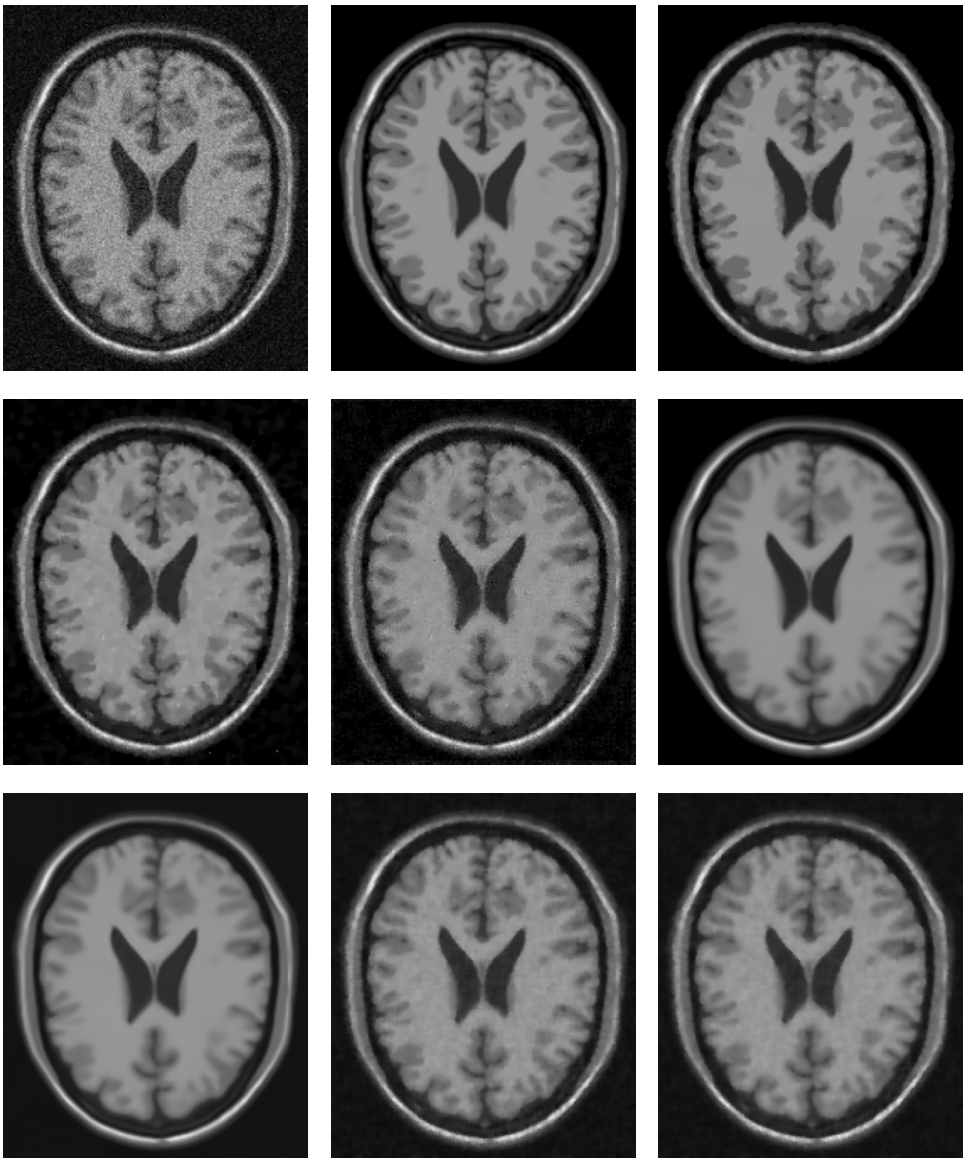

Figure 3.4: The diffusion results of different denoising filters on the synthetic image with a Rician noise of standard deviation $\sigma_n = 15$. From top to bottom and left to right, they are the noisy image, noise free image, results of AADM, SRNRAD, LMMSE, UNLM, NLM, ADPM, and ADBL.

SRNRAD has been proven successful in noise removal in MR images. It obviates the need to choose the main parameter of the AD filter and can be easily extended to structure oriented diffusion as presented by Krissian & Aja-Fernández (2009). However, in our experiments, we still find some limitations of SRNRAD. First, as emphasized in Krissian & Aja-Fernández (2009), SRNRAD relies on the assumption of a Rician distribution. Thus, for dark regions where the distribution is close to Rayleigh, the noise is not fully removed, as can be seen in both Fig. 3.4 and Fig. 3.9. For example, in Fig. 3.9, some noise points inside the colon are even enhanced, which makes the prominence of the colon wall less distinguishable. This may make further computer based analysis such as colon reconstruction difficult, while our method works well in this case. Second, SRNRAD does not give consistent performance in 2D images because fewer pixels are involved in the estimation of local statistics. Our method does not suffer from these problems. In conclusion our method performs better in noise removal and gives satisfactory results in situations where SRNRAD is likely to perform poorly, such as in 2D images and dark image regions.

We also compare our method with two traditional parameter selection methods for AD filter, i.e., ADPM and ADBL. The results show clearly that our method outperforms these two methods. The reason is that if the gradient magnitudes of edge and noise points overlap, the parameter cannot be selected using the gradient magnitude histogram. For the ADBL, the parameter is only dependent on the noise level and does not take into account edge information in the image. Thus, it is also inaccurate.

3.4.1.3 Robustness to Pre-classification Method

In this section, we will demonstrate that our method is robust to parameter selection and the results of the pre-classification method, and performs well on different MR images.

For the modified FCM method used in our scheme, there are two parameters, the neighborhood factor ν and the prototypes V (the set of initial class centers). According to the original paper (Ahmed *et al.*, 2002), $\nu = 0.7$ is optimal for most of the cases. For low-SNR images, in our case $\sigma_n \geq 25$, ν is set to 0.85. Thus, the only parameter we should consider is V. We test our method on the synthetic image with different prototype selection to show the robustness of our method.

1. Optimal parameters estimated on real ground truth image, denoted Real, which shows the best performance we can obtain using our diffusion model.

2. Parameter estimated using our method with different initial class numbers, denoted 2 classes, 3 classes, 4 classes, and 6 classes, respectively.

3. For comparison, we also show the results using SRNRAD.

Fig. 3.5 shows the quantitative results of our method with the above prototype selections. As we can see, even with very rough classification, i.e., 2 classes, our method still performs well and gives results that are consistent with previous experiments. For all the different prototype selections, the results of our method are very similar and close to the results obtained with optimal parameters, which indicates that our method is robust to parameter selection and the results of the pre-classification method.

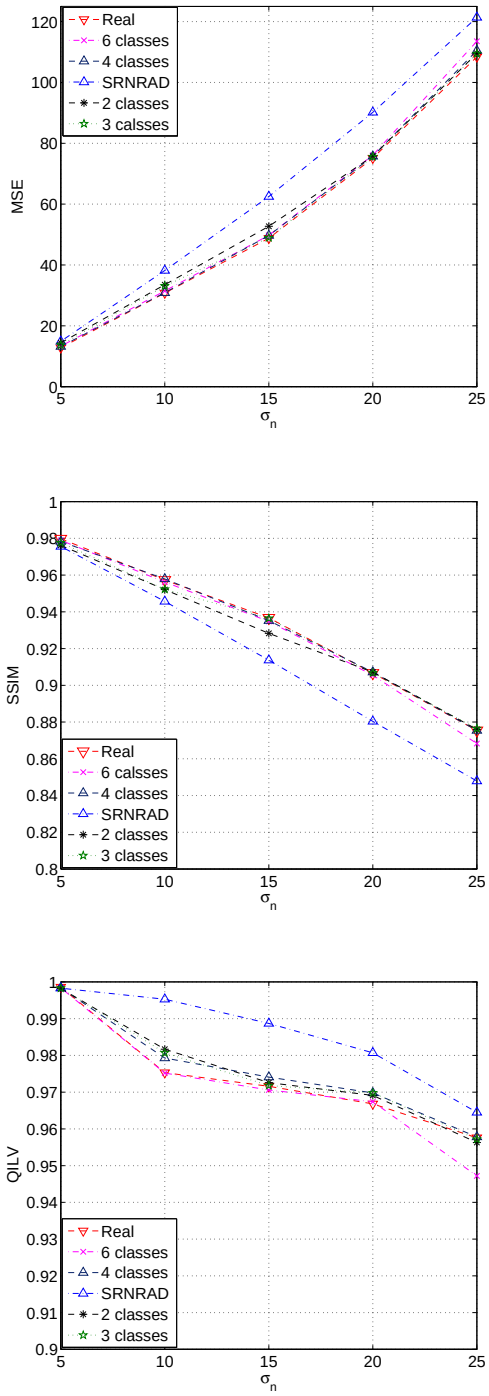

Figure 3.5: MSE, SSIM, and QILV index for results of our method with different pre-classification results. Results show that our method is robust to pre-classification results. The comparison results with SRNRAD are consistent with the conclusion in previous section.

To show that our method is well behaved on images with complicated intensity information, we test our method on the real colon MR image (Fig. 3.6). In this case, we pre-classify the image with 3, 4, and 5 classes. As we can see, the noise is removed and the details are well preserved in all cases. As stated previously, our method needs only the rough contrast information. Thus, for a complicated image, we only need to extract some major intensity levels, which is rather easy to achieve.

The reason why our method is robust to the classification results can be explained by Fig. 3.8, which shows the parameter ranges of our AD filter for the three images in Fig. 3.7 with different noise levels. One observation is that for different images the parameter range for each noise level is different, which explains why previous parameter selection methods based on noise level, such as Black *et al.* (1998), tend to fail. The other observation is that the parameter range increases with the noise level. When the noise level is low, all different segmentation methods tend to produce accurate classification results, and hence similar pseudo ground truth images. When the noise level is high, different segmentation methods may produce different classification results (i.e., some are more accurate than others) for generating the pseudo ground truth image. However, their final results can still be similar because of the wider parameter range.

In conclusion, we have demonstrated that our method is not sensitive to the result of classification. Moreover, the parameter selection for the classification method is also very intuitive. We also proved that our method can work easily on MR images with complicated intensity distributions.

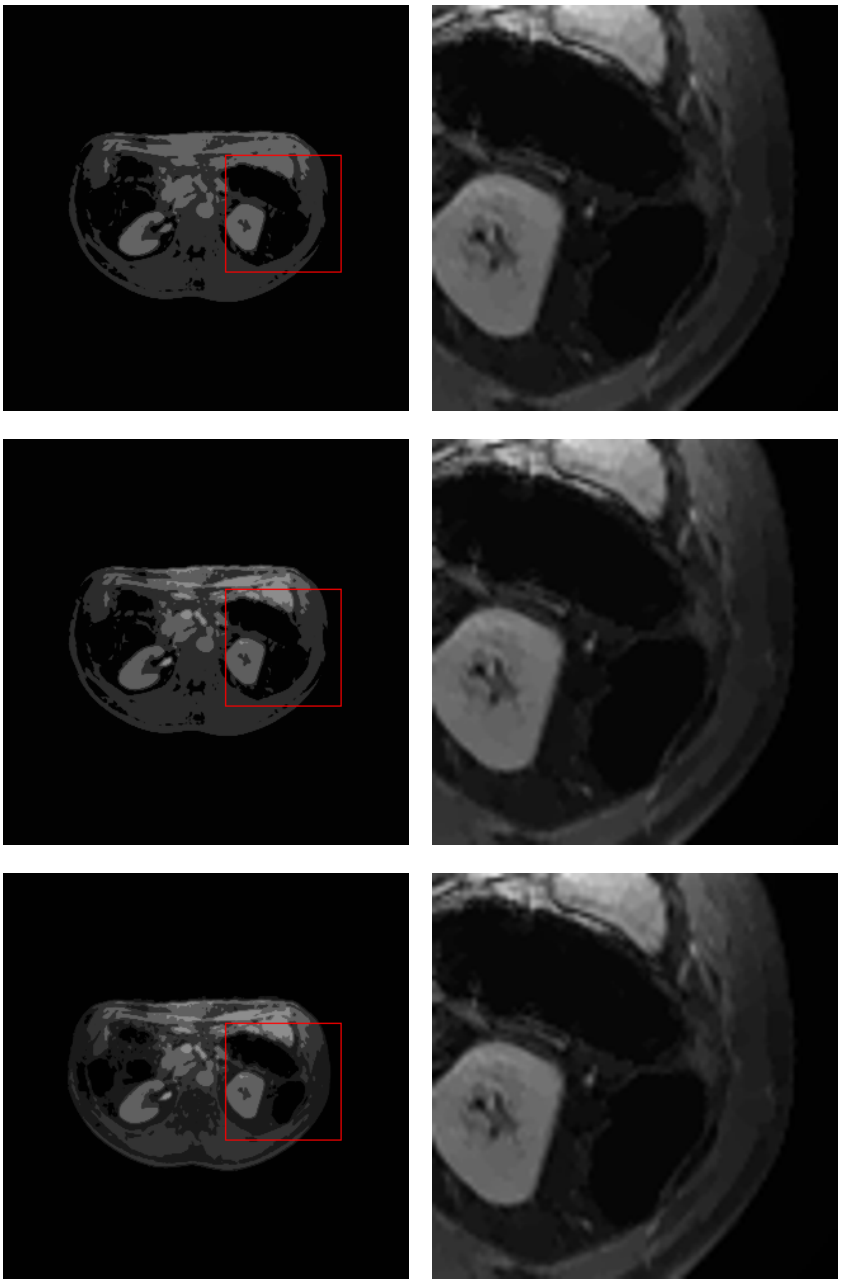

Figure 3.6: Diffusion results on the colon MR image with different pre-classifications. The first column shows the classification results with 3, 4, and 5 initial prototypes, respectively. The second column shows the zoom-in diffusion results based on corresponding classification results. See Fig. 3.9 for the original noisy image.

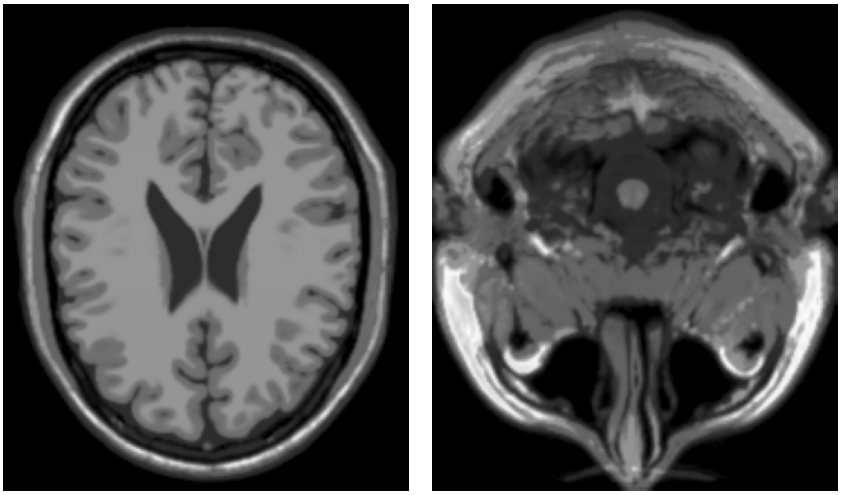

(a) (b)

(c)

Figure 3.7: Three noise free images used to test the parameter ranges for different noise level. (a) The brain slice. (b) The nose slice. (c) The Lena image.

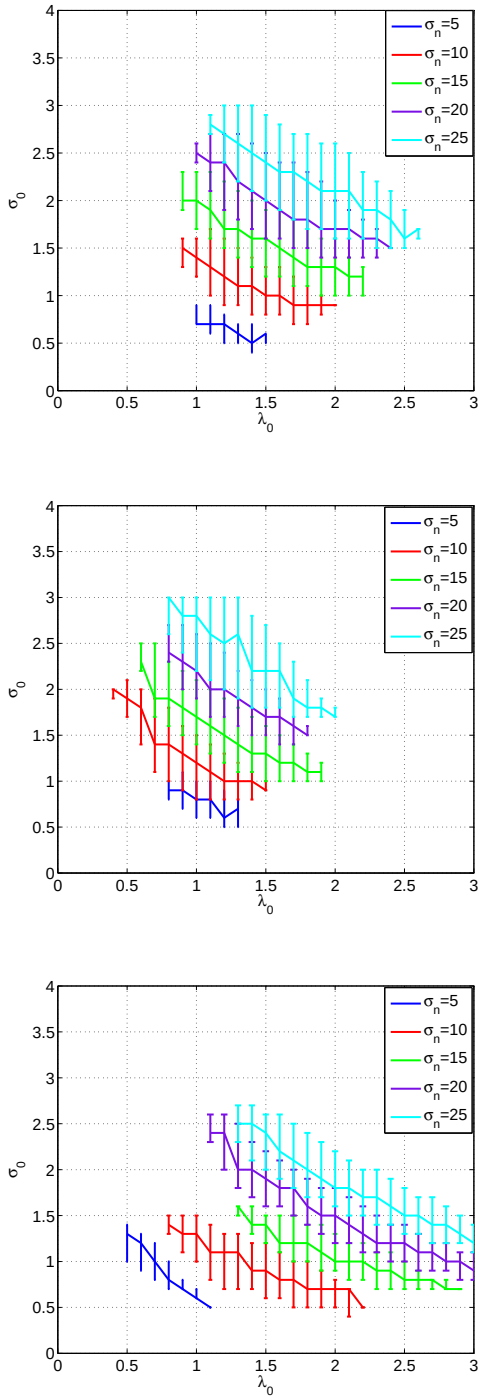

Figure 3.8: Parameter range for images in Fig. 3.7. For each noise level, the figure shows the acceptable parameter range which gives the MSE smaller than $\epsilon \times (1 + 3\%)$, where ϵ is the minimum MSE value for given noise level obtained with real ground truth image. From top to bottom is the parameter range for brain slice, nose slice, and Lena image, respectively.

3.4.2 Real Images

Besides experiments on the simulated MR images, we also validate our parameter selection method on real MR images. To show the robustness of our method with real images, in all our examples, we use the same classification parameters: neighborhood factor $\nu = 0.7$ and prototypes $V = \{0; 25; 50; 100; 150\}$. Figs. 3.9, 3.10, and 3.11 show the diffusion results of different MR images using our scheme. It is evident that most of the noise is removed without blurring of edges. As shown in Fig. 3.9, even the very faint links are preserved as highlighted by the write circles in the zoom-in images. These experiments demonstrate that the proposed method can be effectively applied to different MR images.

3.5 Conclusion

The goal of this chapter is to address the de-noising problem for MR volume images using AD filtering with automatic parameter selection strategy. Traditional parameter selection methods for AD filters are either time consuming (manually tuned) or limited to specific diffusion models (Black's method (Black *et al.*, 1998)). In our method, we extract the contrast and noise information from the noisy input image to generate a synthetic image model that is representative of the real image. We then optimize the parameters on the synthetic model. Since the synthetic model contains all the information needed to determine the parameters of the AD filter, the parameters optimized on the synthetic model are also optimal for the real image. From experiments on simulated MR images, we are also able to determine a proper decreasing rate for the dynamic parameters as well as the parameter search range.

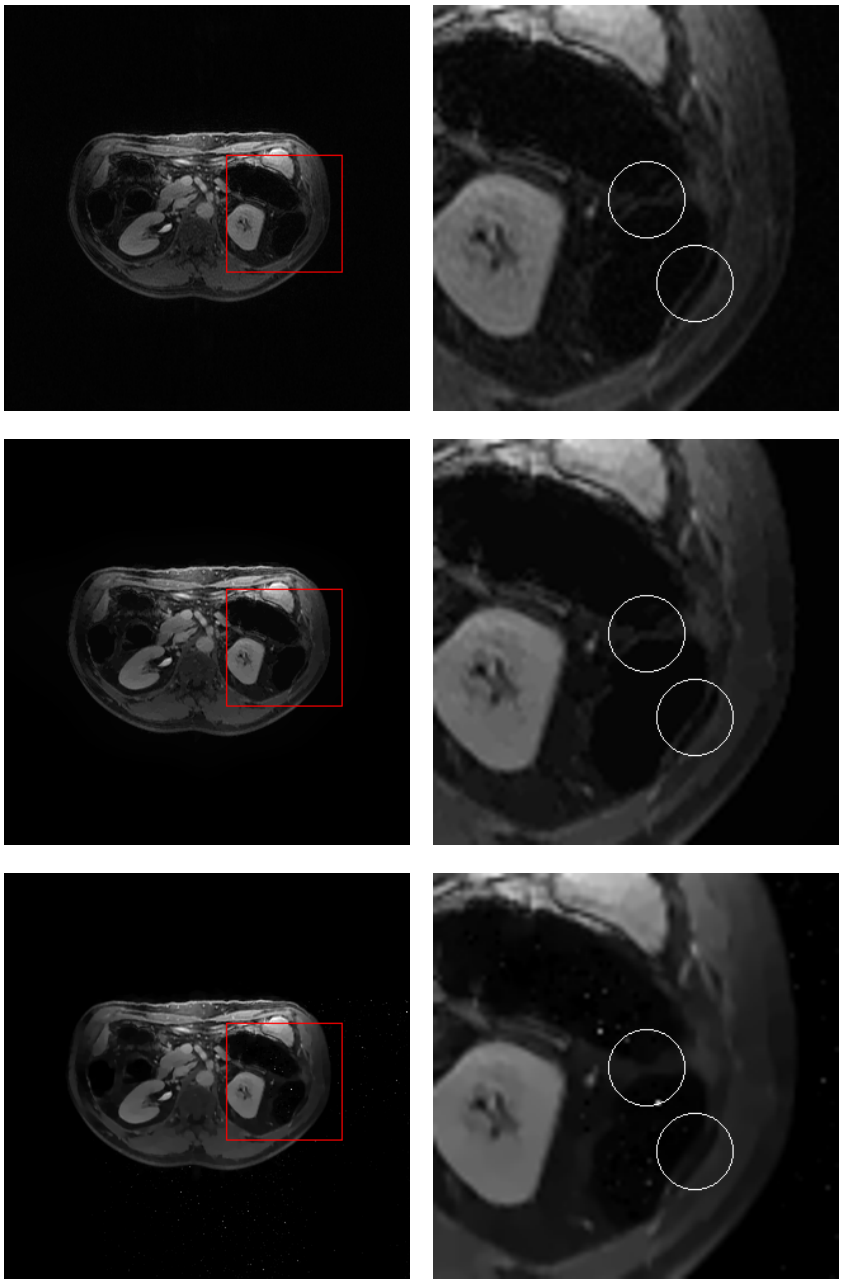

Figure 3.9: Diffusion results on the colon MR image and the zoom in images. The first column shows the noisy image, results of AADM and SRNRAD. The second column shows the zoom in image of the corresponding one. The faint links in the images are highlighted.

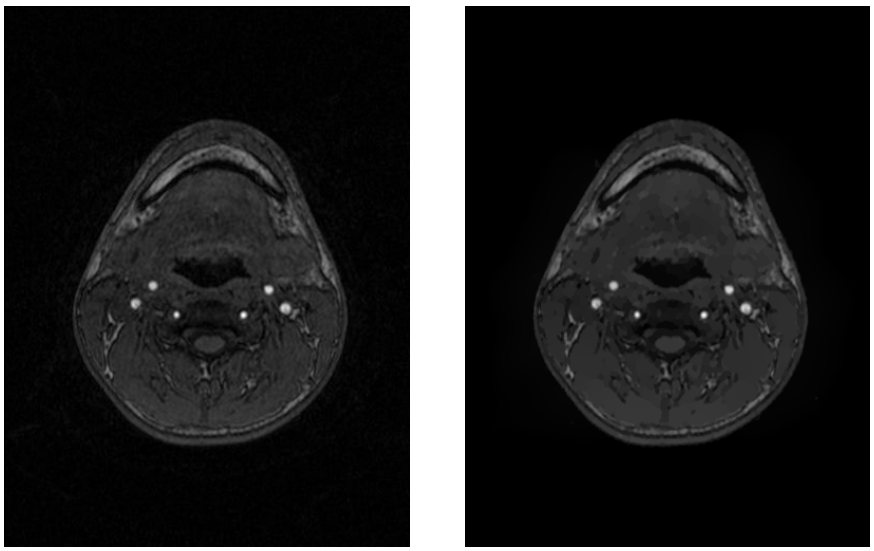

(a) (b)

Figure 3.10: Diffusion results on the mandibular MR image. (a) The noisy image. (b) The diffused image with our method.

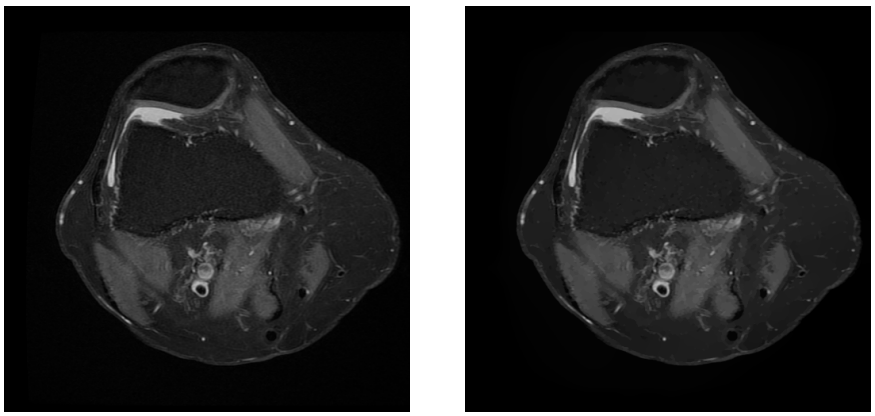

(a) (b)

Figure 3.11: Diffusion results on the knee MR image. (a) The noisy image. (b) The diffused image with our method.

The experimental results on both simulated and real images demonstrated that the results of our method is similar to those obtained with manually tuned parameters. Our diffusion scheme outperforms other MR de-noising methods both qualitatively and quantitatively. Furthermore, our diffusion results are much better than those using traditional automatic parameter selection methods. Furthermore, the proposed scheme is sufficiently general to be used with a variety of diffusion models for improved noise reduction. The diffusion results on real MR images demonstrate that our approach is suitable for MR image de-noising in different organs.

Chapter 4

Volume Image Registration Based Mesh Morphing

This chapter presents a novel solution for automatic patient-specific FE mesh generation based on volume image registration. A 3D deformation field is derived directly from the registration of the atlas and patient medical images and then used to deform the atlas mesh to fit the patients' morphology. This method improves existing methods of surface registration based mesh generation by eliminating the tedious image segmentation step. It also utilizes the rich intensity information in the volume image to achieve a more accurate substructure registration.

4.1 Introduction

The goal of this chapter is to enhance existing mesh morphing technique by developing a one step, automatic method that generates patient-specific FE meshes

directly from the patient's medical image without resorting to image segmentation. The basic idea is that instead of deforming the atlas mesh to fit the segmented patient anatomy surface, all the information in the volume images of the atlas and patient is used in the registration to derive a 3D deformation field, which is then used to deform the atlas mesh.

The main advantage of image registration based mesh morphing is that it eliminates the tedious and time consuming segmentation step, and combines the traditional segmentation and mesh morphing into a single procedure. The use of image registration instead of surface registration increases the organ representation accuracy as the deformation computation relies on the entire data range of the medical image and not only on the surface distance. Consequently, biological information carried by material intensity correspondence leads to more realistic registration compared with the surface based approach where only shape information is considered. Last but not the least, this method makes the computation of the deformation field independent of the configuration of the atlas mesh. Thus, any refinement (defining new sub-structures, etc.) on the atlas mesh structure can be automatically transferred to the patient specific meshes without altering the mesh morphing procedure itself as all the information is already contained in the 3D transformation field derived from the volume image registration. In surface or landmarks based registration schemes, if a new feature needs to be modeled in the atlas mesh, it will also have to be segmented or located in every patient's dataset in order to be properly registered, and the transformation field also needs to be re-computed.

To our knowledge, the application of intensity based volume image registration to FE mesh morphing is not well established. Image based FE mesh

morphing has recently been proposed by Barber *et al.* (2007) and Lamata *et al.* (2011). However, these methods work on either segmented binary images or idealized synthetic images and thus suffer the same limitations of existing surface based methods as none of them takes advantage of the intensity information in the real medical volume image. Their registration algorithm does not guarantee C^1-diffeomorphism transformation which is essential for preserving the quality of the deformed mesh. Moreover, given that both proposed methods rely on the sum of square of the differences of voxel intensity (SSD) cost function, they can hardly be extended to multi-modality registration.

Although the application of intensity based volume image registration methods in FE mesh generation has not been fully investigated, it has already been widely used in inter-subject atlas registration problem, for example, in cardiac (Li & Sun, 2009; Zhuang *et al.*, 2008a,b) and brain (Hellier *et al.*, 2001; Rueckert *et al.*, 2001; Wu *et al.*, 2006) segmentation. In these applications, an atlas is first constructed manually or statistically on a reference data. And different anatomical structures are labeled. By registering the reference data to the patient data, the labels are matched with the voxels of the patient data to obtain a full segmentation. Our problem is similar to this atlas based automatic segmentation problem in that both need to seek the inter-patient deformation by registering the atlas and patient volume images. In these applications the process of finding the transformation between the atlas image and the patient image can also be seen as the process of segmenting the patient image. Thus, by replacing the surface registration based mesh morphing with the image registration based method, we can combine the traditional segmentation and registration mesh morphing procedures into a single step.

The main challenge in applying image registration to FE mesh generation, which is different from other image registration applications, is that the deformation will cause distortion in the FE mesh elements as mentioned earlier. In traditional applications such as image registration based automatic segmentation, the only concern is to register organs of different subjects as accurately as possible, while the resulting deformation field is seldom used or analyzed. Transformation regularity constraints are introduced to make the registration converge to a single result. Our goals in the mesh registration process are not only to accurately match the atlas FE mesh with the patient geometries but also to preserve the quality of the mesh for finite element analysis. However, there is often a trade-off between registration accuracy and mesh quality. The higher the geometrical representation accuracy, the larger the element distortion. To reduce the distortion caused by the registration process, some constraints are needed for the deformation regularity of the non-rigid registration. In the surface based mesh registration method (Bucki *et al.*, 2010), C^1-differentiable, one-to-one and no-folding constraints were imposed on the displacement field to reduce element distortion. Apart for deformation regularization, a mechanical regularization was also used in Bucki *et al.* (2010). The change in potential elastic energy of the mesh is measured at each elementary deformation. The aim is to achieve the largest registration energy (similarity metric) decrease with the smallest increase in the potential elastic energy in the mesh. This will help preserve the mechanical stability of the FE mesh.

As an extension of existing mesh morphing techniques, in this chapter, we present a general solution for automatic patient-specific FE mesh generation based on volume image registration. The main contributions are (1) the inves-

tigation and application of a non-rigid volume image registration method to FE mesh morphing, which is efficient, fulfills all the regularity requirements for mesh morphing algorithm (Bucki *et al.*, 2010), i.e., C^1-diffeomorphism, is non-folding, and can be easily extended to different similarity metrics; and (2) the introduction of a smoothness constraint that reduces FE mesh distortion caused by the registration, thus resulting in an even better mesh quality than that yielded by surface based registration.

The rest of the chapter is arranged as follows. Section 4.2 describes the overall scheme of the proposed method. Section 4.3 presents the volume image registration method, which includes multi-level affine pre-registration, B-spline free-form deformation, and the deformation regularity constraints used to avoid excessive distortion in the generated FE mesh, followed by the optimization method used to achieve fast registration. Section 4.4 presents the atlas mesh warping process with the obtained 3D deformation field from the image registration to generate patient specific FE meshes. Section 4.5 describes the method to correct the irregular or low quality elements in the generated patient meshes resulting from the deformation so that they can be used in further FE analysis.

4.2 Overview

The overall scheme of the proposed mesh morphing method is illustrated in Fig. 4.1. An atlas mesh is first manually generated from a typical medical image representing the target organ so as to include any necessary sub-regions using specific element types, with the desired density, orientation and refinement. However, there are some cases where the atlas meshes are not directly generated

from a specific subject's anatomies. For example, the atlas meshes can also be generated from anatomical knowledge and/or from post-mortem data (such as the data from the Visible Human project). In these cases, step 1 in Fig. 4.1 needs to be inverted. A synthetic binary image can be generated from the atlas mesh by using a surface voxelization method such as the one used in Section 6.2. If sub-structures are considered, more sophisticated synthetic medical image generation methods should be used. Although capable of handling both situations (with or without original medical images), the main strength of our method compared to traditional surface based mesh morphing lies in these situations where the medical images for both the atlas and patient are available, which is often the case for clinical applications.

After obtaining the medical images for both the atlas and the patient, instead of segmenting the patient medical image to obtain the patient organ surface and then deforming the atlas mesh to fit it, we propose to first derive the 3D displacement field implicitly from the volume image registration of the atlas image and the patient image, and then deform the atlas mesh according to the 3D displacement field. The manual assembly of an atlas mesh is beyond the scope of this thesis. We will mainly discuss step 2 and step 3, namely the volume registration of the images and deformation of the atlas mesh.

In this scheme, no patient image segmentation is required. This method not only registers the outer anatomical surfaces but also moves the material points within the image volume according to the image content (gray level values) thus providing a more realistic displacement for the inner nodes of the mesh.

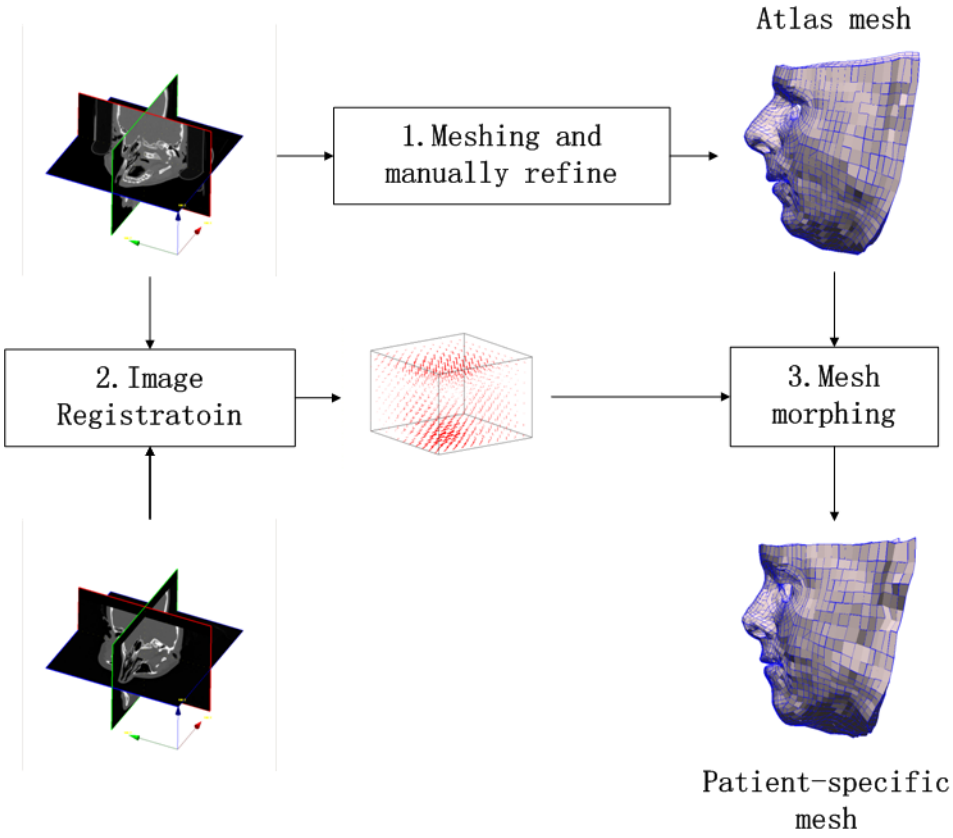

Figure 4.1: Overview of image based FE mesh morphing.

4.3 Volume Image Registration

The volume image registration process in our scheme, i.e., step 2 in Fig. 4.1, consists of two steps: a global alignment by rigid or affine registration followed by a local alignment by non-rigid registration. The two images are first pre-aligned using a global transformation, for example, multi-level affine transformation, to remove the position and scale difference of the two subjects. Then, a non-rigid registration is used to compensate for local inter-patient morphological differences.

The displacement field produced by image registration is backward transformation, which means that by deforming the image features in image A to fit the features in image B, we are actually moving the physical points in image B to the corresponding points in image A. Thus, in order to deform the atlas mesh toward the patient geometry, we set the patient image as the source (moving) image and the atlas image as the target (fixed) image. Therefore, by deforming the patient image to the atlas image we can obtain the deformation field that deforms the nodes of the atlas mesh towards the patient geometry. The deformed image resulting from the global transformation is used as the input image for non-rigid registration.

4.3.1 Intensity Based Multi-level Affine Registration

To compensate for the global position and scaling differences between the atlas and the patient image data, we first conduct global pre-registration. The pre-registration can be image intensity based or landmark based (chosen automatically or manually by the clinicians). The simplest choice for the transformation

is a rigid transformation which is parameterized by 6 degrees of freedom. A more general class of transformation is affine transformations, which have 6 additional degrees of freedom, describing scaling and shearing. The selection of the pre-registration method can be flexible according to the specific clinical application. For example, in some clinical cases, some feature points in the organ of interest can be easily identified across patients, and thus, landmark based registration method may be preferred as it requires less time than image intensity based methods.

In our scheme, we chose a general method which is applicable to different clinical situations, i.e., the multi-level intensity based affine registration. The affine transformation can be written as

$$T_G(x, y, z) = \begin{pmatrix} \theta_{11} & \theta_{12} & \theta_{13} \\ \theta_{21} & \theta_{22} & \theta_{23} \\ \theta_{31} & \theta_{32} & \theta_{33} \end{pmatrix} \begin{pmatrix} x \\ y \\ z \end{pmatrix} + \begin{pmatrix} \theta_{14} \\ \theta_{24} \\ \theta_{34} \end{pmatrix}, \tag{4.1}$$

where the coefficients θs parameterize the 12 degree of freedom of the transformation.

The parameters of the affine transformation are optimized on some similarity metric which measures the similarity or matching accuracy of the target image and the source image deformed by the current transformation. The similarity metrics used here are image intensity based and are the same as the one used in the non-rigid registration (Section 4.3.2.2). As the parameter number is small, the parameters are optimized on the similarity metric using traditional gradient descent.

When computing the image similarity metric, we used a Gaussian pyramid

for the image data. For each pyramid level, the images are smoothed with a Gaussian kernel and then re-sampled by a factor of 2^{N-i}, where N is the total pyramid level number, and i is the current pyramid level number. Typically, three image levels are sufficient for most of the case. Thus, in all our experiments three image levels are used. The affine transformation is first optimized on the smallest image (highest image level) to obtain rough estimation of the parameter values. When it reaches the optimal point, larger images are used and more image details are included to achieve a more accurate estimation of the transformation parameters. By using a multi-level method, we can reduce the computational time, as the parameter optimization on a small image is much faster. Furthermore, by removing details at the beginning the optimization can be kept from been trapped in local minima.

Rigid and affine transformations are intrinsically regular, i.e., they will not cause space folding, and thus will not generate irregular elements in the patient FE mesh. Therefore, we do not need to add any regularization in this part.

4.3.2 Non-rigid Volume Image Registration

The anatomical variability between subjects cannot be sufficiently explained by the above affine transformation which only accounts for differences due to position, orientation and size of the anatomy. To capture the inter-patient local morphological variability, it is necessary to employ a non-rigid transformation. Unlike the affine transformation, a non-rigid transformation will often cause space distortion, which will result in irregular or low quality elements in the generated patient FE mesh, which makes it unsuitable for further FE analysis.

The goals of mesh registration are not only to accurately match the atlas FE mesh with the patient morphology but also to preserve the regularity and quality of the mesh for subsequent FE analysis. It is accepted that, to prevent excessive FE mesh distortion, the registration algorithm used in mesh morphing should be a C^1-diffeomorphism (Bucki *et al.*, 2010). In medical image registration, there are two popular non-rigid diffeomorphic registration methods: the diffeomorphic B-spline free-form deformations (FFDs) (Rueckert *et al.*, 2006) and the diffeomorphic demons (Vercauteren *et al.*, 2009).

To implement our scheme, a time efficient implementation of the diffeomorphic FFDs proposed in Glocker *et al.* (2008) is chosen. The reasons are: (1) it is a natural extension of our previous surface based algorithm which is also FFD based; (2) the transformation field of the FFD is more regular than the transformation field from the fluid like demons as it is controlled by the underlying interpolation function; (3) the implementation method can encode any similarity measure without customization of the optimization method, which makes it convenient to extend our scheme to multi-modality registration. The details of the diffeomorphic FFDs, the implementation method and the optimization method are presented in Rueckert *et al.* (2006), Glocker *et al.* (2008), and Komodakis *et al.* (2007), respectively. Here we provide a summary of the methods with an emphasis on their specific application to our FE mesh morphing scheme.

4.3.2.1 Free-Form Deformation

We set the atlas image as the target (fixed) image g and the patient image deformed by the above affine transformation as the source image (moving) f. A virtual deformable grid G is superimposed onto the target image, i.e., the atlas

image. This grid is used to manipulate the movement of the points in the atlas image. The deformation space is parameterized in this way to reduce the degrees of freedom, thus reducing computation complexity. The transformation of the image pixel $\mathbf{x} = (x, y, z)$ in the target image can be expressed using the B-spline interpolation of the displacement of the grid control points as

$$T_N(\mathbf{x}) = \mathbf{x} + D(\mathbf{x}) \tag{4.2}$$

with

$$D(\mathbf{x}) = \sum_{l=0}^{3}\sum_{m=0}^{3}\sum_{n=0}^{3} B_l(u)B_m(v)B_n(w)\mathbf{d}_{i+l,j+m,k+n}, \tag{4.3}$$

where $i = \lfloor x/\delta_x \rfloor - 1$, $j = \lfloor y/\delta_y \rfloor - 1$, $k = \lfloor z/\delta_z \rfloor - 1$, $u = x/\delta_x - \lfloor x/\delta_x \rfloor$, $v = y/\delta_y - \lfloor y/\delta_y \rfloor$, $w = z/\delta_z - \lfloor z/\delta_z \rfloor$ and δ_x, δ_y, δ_z denote the control point spacing and where $\mathbf{d}_{i,j,k}$ is the displacement of the grid control point with index $[i, j, k]$, which is also known as the transformation parameter, B_l is the lth B-spline basis function measuring the contribution of the control point to the dense displacement field D, and T is the transformation.

The performance of the FFD registration method is limited by the resolution of the control point grid. A coarser control point spacing models a more global and smoother deformation while a finer control point spacing models a more localized and less smooth deformation. In order to cover a wide range of transformations, multi-level FFDs are used. The deformation starts with a coarser control point spacing. When the algorithm reaches its optimum for the current grid configuration, the control point spacing is reduced by a factor of two (in each dimension) to form a finer grid. For each level of control point spacing, several optimization cycles are performed to model a large deformation. Af-

ter each optimization cycle, an elementary transformation field is obtained and the control points return to their original position. The final transformation is obtained by the composition of all the elementary deformations as

$$T_N(\mathbf{x}) = \underbrace{T_J^{N_J} \circ \cdots \circ T_J^1}_{G_J} \circ \cdots \circ \underbrace{T_1^{N_1} \circ \cdots \circ T_1^1}_{G_1}, \tag{4.4}$$

where G_j, $j = 1, \cdots, J$ are successive grid levels, and T_j^i, $i = 1, \cdots, N_j$ are elementary deformations obtained in each optimization cycle at grid level j. Such a multi-level compositional FFDs allows us to use the diffeomorphic constraints in Section 4.3.2.3. The grid levels and the initial control point spacing determine the overall deformation scale and smoothness thus should be customized according to different applications. For the images that are properly pre-aligned by a global transformation, a initial spacing of 20mm and 3 refinement levels can be sufficient for an accurate local registration (Glocker *et al.* (2008)).

4.3.2.2 Similarity Metric

The optimal transformation is found by minimizing a similarity metric which represent the current similarity of the deformed image and the target image w.r.t. the transformation parameters, i.e., the displacements of the grid control points. The implementation of our method does not depend on the similarity metric and different similarity metrics can be used. There are generally two kinds of image similarity metric: one is mono-modality metric such as the squared intensity differences (SSD), sum of absolute difference (SAD) and normalized cross-correlation (NCC). The other is the multi-modality metric such as the normalized mutual information (NMI) (Studholme *et al.*, 1999). The mono-modality

metrics are used to register images with the same modalities, such as CT to CT and MRI to MRI. While the multi-modality methods are used to register images with different modality such as CT to MRI. Since our method is meant to be applicable in both situations, two metrics are used in our experiments.

For mono-modality registration or same modality registration, the absolute difference (SAD) is used, which can be expressed as

$$E_{data}(T_N) = \sum_{\mathbf{x}\in\Omega} |g(\mathbf{x}) - f(T_N(\mathbf{x}))|, \tag{4.5}$$

where Ω is the domain of the target image g and $\mathbf{x}$ is a pixel inside this domain, f is the deformed patient image resulting from the global registration. The symbol $|\cdot|$ is the absolute value of the intensity difference of two corresponding points. Compare with the squared intensity difference (SSD) metric, the SAD metric is less sensitive to noise and outliers.

For multi-modality registration or different modality registration, the NMI metric is used, which is defined as

$$E_{data}\left(A, B\right) = \frac{H\left(A\right) + H\left(B\right)}{H\left(A, B\right)}, \tag{4.6}$$

where $H\left(A\right)$, $H\left(B\right)$ denote the marginal entropies of image A, B (target image g and deformed source image f^{T_N}) and $H\left(A, B\right)$ denotes their joint entropy, which is calculated from the joint histogram of A and B. This normalization form is devised to overcome the sensitivity of mutual information to change in image overlap (Studholme *et al.*, 1999).

4.3.2.3 Diffeomorphism and Regularization

As mentioned earlier, meshes deformed by non-rigid registration are often prone to element distortion. One adverse effect is that it may cause some elements to loss their regularity, thus preventing FE analysis from being carried out (Luboz *et al.*, 2005). Another effect is that it may decrease the element shape quality for some elements, which leads to lower accuracy in numerical simulations (Field, 2000; Kwok & Chen, 2000; Shewchuk, 2002). For a detailed description of element regularity and quality, readers can refer to Section 2.1.3.2, or Section 4.5. Although the irregular and low quality elements can be untangled by manual reparation or automatic relaxation procedures (Bucki *et al.*, 2011), when the distortion is large, the element may become irreparable, or even if reparable it may greatly change the current morphology of the mesh, thus reducing the representation accuracy. Therefore, in our scheme, it is very important to control the distortion of the generated patient mesh when computing the deformation field. In a previous surface based method (Bucki *et al.*, 2010), several smoothness requirements have been proposed for the deformation field produced by the mesh morphing algorithm: C^1-differentiable, non-folding and invertible, i.e., C^1-diffeomorphism. In this scheme, the C^1-differentiable requirement is inherently satisfied by the B-spline basis function used. This formulation of shape functions also guarantees the differentiability of the deformation function throughout the domain. To achieve the diffeomorphic requirement, i.e., bijection and differentiable, we adopt the hard constraint proposed in Rueckert *et al.* (2006). For each elementary deformation T_j^i in Eq. (4.4), we restrict the displacement of control points to 0.4 times the current control point spac-

ing (Rueckert *et al.*, 2006). This ensures the diffeomorphic nature of each elementary deformation, and since we compose the elementary deformations (and the composition of two diffeomorphisms produces a diffeomorphism), the final transformation is a diffeomorphism as well.

However, the non-folding constraint of the transformation field does not preserve the mesh elements from potential distortions. In fact, it is a local property ensuring that the local space at every point is not folded. For a linear FE mesh defined on a larger scale, this property does not hold. Thus, irregular and low quality elements may still appear in the patient-specific FE mesh after the registration process. In order to further reduce space distortions, we introduce an additional regularization term for the deformation field as

$$E_{smooth}(T_N) = \sum_{\mathbf{p} \in G} \sum_{\mathbf{q} \in N(\mathbf{p})} |\mathbf{d_p} - \mathbf{d_q}|^2, \tag{4.7}$$

where $\mathbf{d_p}$ is the displacement for control point $\mathbf{p}$ and N represent the set of control points in the neighborhood of $\mathbf{p}$. This neighborhood is defined as the set of points connected by an edge of the control grid to point $\mathbf{p}$. This regularization term ensures that the displacements applied to two neighboring control points tend to move in a similar direction. Here we impose this regularization term on the entire displacement field instead of the current elementary displacement field to ensure the smoothness of the final deformation field. The details are described in Section 4.3.2.4.

The complete cost function associated with our registration problem is then

defined as the sum of the data and smoothness terms in Eq. (4.5) and Eq. (4.7):

$$E_{total}(T_N) = E_{data}(T_N) + \lambda E_{smooth}(T_N), \tag{4.8}$$

where λ is a weighting parameter which controls the influence of the regularization term. The transformation parameters are then optimized on this cost function by an appropriate optimization method such as the widely used gradient-descent (Rueckert *et al.*, 1999) or quasi-Newton (Klein *et al.*, 2007). Both optimization methods require the computation of the derivative of the cost function with respect to the transformation parameters, which makes the optimization process dependent on the form of the cost function, i.e., it needs to be customized when using a different similarity metric. Furthermore, calculating the derivative can be time consuming. It usually takes hours for a volume image registration by using these optimization methods (Glocker *et al.*, 2008), which becomes a major drawback for the application of the FFD image registration method in a clinical environment, where the time window for FE mesh generation is short.

4.3.2.4 Optimization Through Markov Random Field Formulation

To address the above problems, we adopt a recently proposed optimization method for FFD registration (Glocker *et al.*, 2008), which does not require derivative of the cost function, while makes it independent of similarity metrics and much more computationally efficient than traditional optimization methods. The idea of this method is to project both parts of the cost function in Eq. (4.8) back to the level of control points, so that it becomes a function dependent di-

rectly on the displacements of the control points instead of pixels. Then by quantizing the displacement space for each control point and associating the quantized displacement vectors with labels, the cost function minimization problem becomes an optimal labeling problem, which then can be efficiently solved by an existing optimization technique. In this section we will briefly introduce the link between the minimization problem in Eq. (4.8) and the labeling problem, as well as the specific parameter setting used in our scheme. Details of the reformulation and the optimization method are given in Glocker *et al.* (2008); Komodakis *et al.* (2007).

First of all, the continuous displacement space for the control points is sampled to form a discrete set of displacement vectors $\Theta = \{\mathbf{d}^1, \ldots, \mathbf{d}^i\}$, which is associated with a discrete set of labels $L = \{l^1, \ldots, l^i\}$. In this way, assigning a label $l_{\mathbf{p}}$ to a control point $\mathbf{p}$ is associated with displacing this control point by the displacement vector $\mathbf{d}^{l_{\mathbf{p}}}$. In our scheme, a sparse sampling method is used. The displacements along the main axis x, y, z are sampled by a factor of n from the zero displacement up to the maximum displacement, i.e., 0.4 times the current control point spacing, thus, resulting in $6n + 1$ labels (including the zero-displacement vector).

To reformulate the energy minimization problem in Eq. (4.8) into a multi-labeling problem, the similarity function defined on the image pixel level in Eq. (4.5) should be projected back to the control points level by a weighting function

$$\hat{\eta}(|\mathbf{x} - \mathbf{p}|) = \frac{\eta(|\mathbf{x} - \mathbf{p}|)}{\sum_{\mathbf{y} \in \Omega} \eta(|\mathbf{y} - \mathbf{p}|)}, \tag{4.9}$$

where $\hat{\eta}(\cdot)$ represents the influence of an image point $\mathbf{x}$ on control point $\mathbf{p}$, and

$\eta(\cdot)$ represents the influence of a control point **p** on an image point **x**. Specifically, the weighting function $\eta(\cdot)$ which measures the influence of the a control point **p** on an image point **x** is the B-spline function used in Eq.(4.3), while $\hat{\eta}(\cdot)$ can be seen as a kind of inverse function of $\eta(\cdot)$. Both these functions are functions of the distance between control point **p** and image pixel **x**, which means that when the distance between these points is smaller, they will have a larger influence on each other.

Taking the SAD similarity metric as an example, the data term in Eq. (4.5) projected back onto each control point **p** can be expressed as

$$V_{\mathbf{p}}(l_{\mathbf{p}}) = \sum_{\mathbf{x}\in\Omega} \hat{\eta}(|\mathbf{x}-\mathbf{p}|) \cdot |g(\mathbf{x}) - f(T^{t-1}(\mathbf{x}) + \mathbf{d}^{l_{\mathbf{p}}})|, \tag{4.10}$$

where $V_{\mathbf{p}}(l_{\mathbf{p}})$ is the data term (similarity measure) projected back onto control point **p**, which is a function of the labeling (displacement) of point **p**. T^{t-1} is the current total transformation, $\mathbf{d}^{l_{\mathbf{p}}}$ is the next elementary displacement of the control point **p** to be optimized, and the data term projected back on each control point **p** is expressed as the weighted combination of all the data cost of the pixels that have an influence on it.

Obviously, the above projection method of the data term is only valid for point-wise similarity measures, such as the SAD metric. For more complex and statistical measure, such as the NMI metric, the projection of the similarity metric on the grid points should be computed slightly differently. First, another

version of the back projection function $\hat{\eta}$ is defined as

$$\hat{\eta}(|\mathbf{x}-\mathbf{p}|) = \begin{cases} 1, & \text{if } \eta(|\mathbf{x}-\mathbf{p}|) > 0 \\ -x & \text{otherwise} \end{cases} \tag{4.11}$$

Basically, this will mask pixels influenced by a control point $\mathbf{p}$, which will result in a local image patch centered at the control point. The data term projected back on point $\mathbf{p}$, i.e., $V_{\mathbf{p}}(l_{\mathbf{p}})$, is then represented by the similarity measure (e.g. NMI) computed on this local patch.

Since the smoothness term in Eq. (4.7) is directly defined on control points, it can be simply reformulated into the labeling problem as

$$V_{\mathbf{pq}}(l_{\mathbf{p}}, l_{\mathbf{q}}) = |(R(\mathbf{p}) + \mathbf{d}^{l_{\mathbf{p}}}) - (R(\mathbf{q}) + \mathbf{d}^{l_{\mathbf{q}}})|, \tag{4.12}$$

where $V_{\mathbf{pq}}(l_{\mathbf{p}}, l_{\mathbf{q}})$ is the smoothness constraint between points $\mathbf{p}$ and $\mathbf{q}$, which is a function of the labeling (displacement) of both $\mathbf{p}$ and $\mathbf{q}$, $R(\cdot)$ projects the current total displacement field on the level of control points as

$$R(\mathbf{p}) = \sum_{\mathbf{x}\in\Omega} \hat{\eta}(|\mathbf{x}-\mathbf{p}|) D(\mathbf{x}). \tag{4.13}$$

Here, we project the current displacement field on the level of control points so that the smoothness term is imposed on the total displacement field. Thus, it will result in a more smooth final transformation.

Combining the above two parts, the energy minimization problem in Eq. (4.8)

is then reformulated into a multi-labeling problem as

$$E_{total}(\mathbf{l}) = \sum_{\mathbf{p}\in G} V_{\mathbf{p}}(l_{\mathbf{p}}) + \lambda \sum_{\mathbf{p}\in G} \sum_{\mathbf{q}\in N(\mathbf{p})} V_{\mathbf{pq}}(l_{\mathbf{p}}, l_{\mathbf{q}}), \tag{4.14}$$

where the first part corresponds to the data term in Eq. (4.8), the second part corresponds to the smoothness term in Eq. (4.8), N represents the neighboring system of the control points, λ is the weighting parameter for the smoothness term.

The multi-labeling problem in Eq. (4.14) is of the same form as the first order Markov random fields (MRFs) (Geman & Geman, 1984; Li, 2001), with $V_{\mathbf{p}}(l_{\mathbf{p}})$ corresponding to the unary potential and $V_{\mathbf{pq}}(l_{\mathbf{p}}, l_{\mathbf{q}})$ corresponding to the pair-wise potential. Since the unary potentials in MRFs are assumed to be independent, i.e., $V_{\mathbf{p}}(l_{\mathbf{p}})$ should be a function dependent only on the labeling of point $\mathbf{p}$, two approximations are used (Glocker *et al.*, 2008): (1) the elementary deformation of point x in Eq. (4.3) is simplified by direct translation of $\mathbf{d}^{l_{\mathbf{p}}}$ (the displacement of control point $\mathbf{p}$) instead of a weighted combination of the displacement of all the neighboring control points as expressed in Eq. (4.10); (2) instead of using B-spline weighting function in the computation of $\hat{\eta}$, the linear weighting function is used so that the overlapping area for each control point is smaller.

After reformulating the registration into this MRF, it is then solved by a computationally efficient optimization method called fast-PD (Komodakis *et al.*, 2007). As described in Section 4.3.2.3, in order to model large deformations while remain diffeomorphic, several optimization cycles are performed for each grid level. As fast-PD optimization generates quasi-optimal labeling on the cur-

rent discrete set of labels, usually no further improvement of the registration can be achieved using the same displacement set. Thus, after each optimization cycle, a new set of displacement vectors are used, and this is done by reducing the maximum displacement by a scaling factor α, and resampling using the same method above.

The parameters associated with the MRF optimization method are: (1) the displacement space sampling steps n, (2) the number of optimization cycles I for each grid level, and (3) the label factor α used to refine the label sets after each cycle. These parameters are used to drive the optimization process and do not relate to the content of the images used in the registration. Their values were thus fixed following the original article (Glocker *et al.* (2008)) as $n = 5$, $I = 5$, and $\alpha = 0.67$. For all the clinical cases in this section, we use the same settings.

4.4 Atlas Mesh Morphing

After volume image registration, we obtain two dense image transformation fields defined on the image grid: T_G from global registration, and T_N from the non-rigid registration. These two transformations are then composed to form the total transformation as

$$T_{total} = T_G \circ T_N. \tag{4.15}$$

As the transformation field produced by image registration is backward transformation, the two transformation fields are composed in a reversed order. The idea is illustrated in Fig. 4.2 on 2D images. To transform a feature point in the target

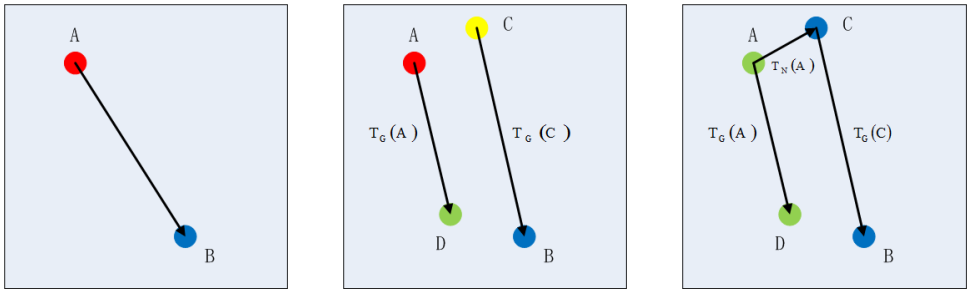

(a) (b) (c)

Figure 4.2: Illustration of the total transformation field composition. The color dots are used to represent features, while the letters are used to represent the physical positions. (a) The two image overlaid before the transformation. (b) shows the transformations obtained after the global transformation. (c) shows the images after the global transformation and the non-rigid transformation computed on these images.

image (blue dot) to match with a feature point in the source image (red dot), we are actually seeking the transformation that transforms the physical point A to point B. Notice that the blue dot is the moving feature which is in the source image, while the red dot is fixed feature which is in the target image. In Fig. 4.2, in order to show the relative position, the two images are overlaid. The images go through a global transformation and a non-rigid transformation sequentially. After the global transformation, the green dot transforms to A while the blue dot transforms to C. This new image is then used in the non-rigid transformation to compute T_N, which finally transforms the blue dot to A. Thus, the total transformation that transformed the point A to B (visually blue dot to A) can be represented as

$$B = T_G(C) = T_G(T_N(A)). \tag{4.16}$$

Thus we can see that the transformation from the global and non-rigid transformation should be composed in a reversed order.

The atlas FE meshes used in this thesis are linear meshes[1]. Therefore, mesh wrapping, i.e., step 3 in Fig. 4.1, is performed by transforming the FE mesh nodes alone according to the transformation field while keeping the same element connectivity. In our scheme, the displacement for a certain FE mesh node is found by tri-linear interpolation of the displacements of its neighboring pixels. For non-linear FE meshes, a more sophisticated mesh wrapping method can be used, such as the one proposed in Lamata *et al.* (2011) for cubic Hermite meshes.

4.5 Mesh Repair

Although the regularizations introduced in our scheme strongly limits space distortion, the generated mesh may exhibit irregular or low quality elements that need to be untangled before proceeding to FE analysis.

4.5.1 Mesh Quality Measurements

The FE mesh quality is assessed at two levels: mesh regularity and mesh quality (see Section 2.1.3.2), which are measured by the determinant of the Jacobian matrix $|J|$, called "Jacobian" and the "Jacobian Ratio" (JR), respectively (Knupp, 2000a). The Jacobian is used to assess mesh regularity i.e. the ability to use a given mesh for FE analysis. A Jacobian value can be computed for each mesh node within each "parent" element, i.e., a mesh element involving the considered node. Note that a node usually has different Jacobian values

[1]The mesh domain is defined by linear interpolation of the nodes, i.e., nodes are connected by straight lines.

throughout its parent elements. If the FE mesh contains a node having a zero or negative Jacobian within an element, the element, and by extension, the entire mesh, is said to be "irregular". Finite element analysis can only be carried out on regular meshes, where all nodes have strictly positive Jacobians within all parent elements.

Among the many available mesh quality indicators we have chosen to work with the Jacobian Ratio (Knupp, 2000a) for its versatility to assess shape conformity. The Jacobian Ratio (JR) is also considered for each FE mesh node within its parent elements. The JR for node n within parent element e is defined as follows:

$$\mathrm{JR}_{\mathrm{n}}^{e} = \frac{|J|_{\mathrm{n}}^{e}}{|J|_{max}^{e}}, \tag{4.17}$$

where $|J|_{\mathrm{n}}^{e}$ is the Jacobian value for node n in element e, and $|J|_{max}^{e}$ is the maximum nodal Jacobian value among all nodes in element e. The JR values range in $[0, 1]$. If $\mathrm{JR}_{\mathrm{n}}^{e} = 1$ then all nodes in element e share the same Jacobian value as the one measured at node n. Such an element is well suited for FE analysis. Lower JR values indicate a higher mesh distortion. Finite element analyses carried out on meshes featuring excessively low JR values are prone to numerical instability and the final solution accuracy is uncertain. The commercial FE software ANSYS defines a minimal JR value of $1/30$ (Kelly, 1998). Any mesh with a quality lower than this threshold will be rejected by the solver.

4.5.2 Automatic Mesh Repair

Automatic methods can be used to untangle the small amount of problematic elements generated by our scheme (Bucki *et al.*, 2011). The basic idea of the

method is to relax the position of the problematic FE mesh nodes or if necessary their surrounding nodes to recover the regularity and quality of the corresponding elements.

The method mainly consists of 4 steps:

1. Irregular and low quality elements detection. The irregular and low quality elements in the generated mesh are first detected according to the quality measures described above.

2. Irregular and low quality region definition. A large number of nodes in a mesh can make the repair procedure computationally prohibitive. Thus, the irregular and low quality elements are grouped into local regions. The nodal correction is then performed separately in each of these regions, leaving the nodal position outside the region unchanged.

3. Irregular elements repair. For each irregular region R, the node positions inside this region are adjusted so that all the Jacobians in R, i.e., $\{J_j\}_{j\in R}$, are positive. This nodal correction is done by maximization a "regularity energy" E_R defined as the weighted sum of all Jacobians within R

$$E_R = \sum_{j\in R} \varphi_k(J_j), \tag{4.18}$$

where $\varphi_k(t) = 1 - \exp(-kt)$ is a weighting function which gives negative Jacobian values a higher weight thus favoring a solution where all Jacobians in the sum are positive. The parameter k is increased during the optimization process.

4. Low quality elements repair. After all the irregular elements are repaired in

step 3, the low quality elements are recovered using similar energy maximization method so that all the JRs in a region R are above a pre-defined level JR_{min}, i.e., 0.03 (Kelly, 1998). The "quality energy" E_Q is defined as the weighted sum of all JRs within R

$$E_Q = \sum_{j \in R, e \in R} \Psi_k(\text{JR}_j^e), \tag{4.19}$$

where $\Psi_k(t) = 1 - \exp(k(\text{JR}_{min} - t))$ is a weighting function which gives JR values below the threshould JR_{min} a higher weight, thus favoring a solution where all JRs in the sum are above the threshould. The parameter k is increased during the optimization process.

Both regularity and quality optimizations are carried out by gradient descent. The amplitude and number of iteration for each region are limited so as to restrict loss of surface representation accuracy. In our scheme, a maximum of 50 iterations are used, and nodal displacement at each step is restricted to 0.1mm.

Although irregular and low quality elements in the generated mesh can be repaired by using post-processing method, it will also compromise the mesh accuracy established in prior mesh registration. Moreover, when the mesh distortion is large, there is no formal proof that an acceptable configuration exists and can be found by the relaxation procedure within limited iterations and amplitude of nodal displacement. Thus, the deformation regularity constraints proposed in Section 4.3.2.3 is of greatly importance. According to our experiments on a database of diverse organ shapes and clinical cases in Chapter 6, we have demonstrated that the smoothness constraints in our scheme strongly limits spatial distortions making it possible to recover both mesh regularity and quality

for all the generated meshes without affect mesh accuracy by much.

4.6 Conclusion

The goal of this chapter is the automatic generation of patient-specific FE mesh by using 3D volume image registration. A multi-resolution intensity based affine registration is first used to approximately align the atlas data with the patient data. Then, the B-spline FFD non-rigid registration is used to compensate for the inter-subject difference. An invertible, non-folding constrain is imposed on the deformation field to avoid space folding caused by the deformations. A smoothness term is also proposed to further preserve the quality of the generated FE mesh. An efficient optimization method is used in our scheme, which allows fast non-rigid registration and can easily incorporate different similarity metrics. The 3D transformation field resulting from the image registration is then used to deform the atlas FE mesh to fit the patient specific geometries, thus generating the patient-specific FE mesh. An automatic mesh repair method is used to correct the small amount of irregular and low quality elements in the mesh caused by the deformation. This novel image registration based FE mesh morphing method improves traditional surface registration based mesh morphing method by eliminating the tedious and often difficult segmentations step, thus bringing patient-specific FE mesh generation one step closer to full automatic. Since the optimization method used in this scheme does not need to be customized for different similarity metrics, our method can also be used in multi-modal image registration based mesh morphing.

Chapter 5

Atlas Mesh Refinement

In this chapter, we present a point-to-surface registration based atlas FE mesh refinement method that can be used to improve the matching accuracy between the atlas FE mesh and the atlas medial image. This will help to reduce the representation error carried on from the atlas mesh to the patient meshes. The proposed method is validated on a face FE atlas mesh.

5.1 Introduction

In last chapter, we present an implicit atlas FE mesh deformation method. The atlas mesh is deformed according to the registration result of the atlas and patient medical images. For this scheme to work properly, an underlying assumption is that the atlas mesh should be well aligned with the atlas image, and thus the transformation field computed with the atlas image can be directly used on the atlas mesh. In clinical applications, there are generally two ways to obtain the atlas mesh and atlas image: (1) generating the synthetic atlas image from the

constructed atlas mesh (as described in Section 6.2), (2) constructing atlas mesh from the medical image of a selected subject (as described in Section 6.3). For the first case, since the atlas image is directly generated from the atlas mesh by using some voxelization methods (such as the one in Section 6.2), the atlas image fits perfectly the atlas FE model. However, for the second case, although the atlas mesh is generated from the extracted geometry in the atlas image, there are always some approximation or refinement processes during the construction of FE mesh, which will result in a fitting error between the atlas FE mesh and atlas image. This error should be reduced beforehand, or it will be carried on to the patient meshes, and increasing the registration accuracy will not help to remove this error.

In this section, we present a scheme that automatically refines the atlas mesh to reduce the representation error between the atlas mesh and the atlas image, thus improving the representation accuracy of the generated patient meshes. The method is based on point-to-surface registration. A diffeomorphic constraint is used to preserve the quality of the atlas mesh while it is deformed. The proposed method is validated on a face FE model qualitatively and quantitatively. Results on how this atlas mesh refinement may affect the accuracy of the patient mesh are also presented.

5.2 Method

To increase the representation accuracy of the atlas mesh, i.e., the geometry accuracy as in Section 2.1.3.1, the external surfaces of the atlas mesh should closely match the surfaces of the interested organ in the atlas image. This can

be done by deforming the atlas mesh to the segmented organ surfaces by minimizing the surface error. This process is similar to the surface based mesh morphing method described in Bucki *et al.* (2010). Generally speaking, this process consists of two steps: (1) atlas medical image segmentation to extract the external surface of the interested organ; (2) atlas mesh deformation by minimizing the distance between the external nodes of the atlas mesh and the segmented surface.

5.2.1 Atlas Image Segmentation

The atlas image is first segmented manually or automatically to extract the external surface of the interested organ. Different segmentation methods can be used depending on the organ to be segmented and the image modality. Due to the complexity of medical images, user interventions are often required to obtain accurate segmentation results. However, this is not a limitation to our approach. Since the atlas mesh is processed pre-operatively only once for each FE model. Thus, the processing time for this step does not count toward the patient-specific FE mesh generation time.

In our experiments, the atlas image is segmented with a medical image processing application, Mimics 10.01. The image is segmented using thresholding and region growing methods. The lower and upper intensity thresholds are interactively determined by observing the segmentation results. The obtained binary mask is refined manually to eliminate segmentation errors. A 3D triangular surface mash is then calculated from the binary mask. This surface mesh is smoothed to remove extraneous details caused by noise. The final result is

exported to an STL file, which contains the coordinates of the vertices, the triangular face connections, and the normals of the triangular faces.

5.2.2 Surface Registration Based Atlas Mesh Deformation

5.2.2.1 Diffeomorphic FFD transformation

Although the error between the atlas mesh and atlas image is small, it should still be modeled locally as a non-rigid transformation. The non-rigid transformation is used to deform a source point cloud S (the external nodes of the atlas mesh) onto a target data set D (the segmented organ surface mesh). For consistency, the same multi-resolution B-spline FFD transformation as in Section 4.3.2.1 is used.

Different from the transformation used in Section 4.3.2.1, the transformation used here is forward transformation, which means that the coordinates of the source points are directly transformed. Therefore, the atlas mesh is initially embedded in an FFD grid. We set the shape of the grid to be the bounding box of the atlas mesh, extended by a 10% margin. The displacement of a source point is found by B-spline interpolation of the displacement of its neighboring FFD control points. The control point spacing of the FFD grid is gradually refined to model more local deformations. The resulting elementary transformation fields are then composed, and used to transform all the nodes (including inner nodes) of the atlas mesh. For a detailed description of the FFD transformation, please refer to Section 4.3.2.1.

To avoid space distortion caused by the transformation and to preserve the quality of the atlas mesh, the diffeomorphic constraint (Section 4.3.2.3) is also

used. For each elementary FFD transformation, the displacement of each control point is restricted to 0.4 times the current control point spacing. Although the difffeomorphic transformation is used, a small amount of irregular or low quality elements may still appear in the deformed atlas FE mesh. These elements can be fixed by automatic mesh repair method as described in Section 4.5.

5.2.2.2 Similarity Metric

The parameters of the FFD transformation, i.e., the displacements of the control points, are found by minimizing a similarity metric which measures the matching accuracy between the deformed atlas mesh surface S and the segmented atlas organ surface D. As geometrical shape similarity is sought, we define the similarity metric as the sum of Euclidean distances between S and D:

$$E(T_N) = \sum_{\mathbf{s} \in S} d(T_N(\mathbf{s}), D), \tag{5.1}$$

where $\mathbf{s}$ is a node on the external surface of the atlas mesh, D is the segmented organ surface, and T_N is the non-rigid transformation we want to find. For some FE meshes, multiple structures are labeled and need to be accurately matched. For example, for the face FE mesh in Section 6.3.1, both the skin and skull surface is labeled on the atlas FE mesh and need to be registered with the skin and skull surface in the atlas image respectively. In this case, the similarity for each structure is computed separately as in Eq. (5.1) and then added together as the total similarity metric.

The operator d is a point-to-surface distance measure. It is computed by first identifying, for each node $\mathbf{s}$ on external surface of atlas mesh S, the closest point

d on the surface D. Then the point-to-surface distance is computed as:

$$d(\mathbf{s}, D) = \| \mathbf{d} - \mathbf{s} \| . \tag{5.2}$$

For the triangular organ surface D generated in Section 5.2.1, the closest point **d** for each node **s** is obtained by this algorithm:

1. For each node **s**, search for the closest vertex **v** to it on D.

2. Search for the triangular faces ($f_i, i = 1, \cdots, m$) associated with the closest vertex **v**.

3. Compute the point-to-surface distances from **s** to all the selected faces. For a certain face f_i, the distance is computed as $d_i = |\vec{n}_i \cdot (\mathbf{s} - \mathbf{v})|$, where $\vec{n}_i$ is the normal of face f_i.

4. The closest point **d** to **s** is supposed to locate on the face f_i with the minimum point-to-surface distance d_i as computed in the last step. The specific location of **d** can be computed as

$$\mathbf{d} = \mathbf{s} - \vec{n}_i \times (\vec{n}_i \cdot (\mathbf{s} - \mathbf{v})). \tag{5.3}$$

Ideally, the position of **d** should be updated at every iteration with the displacement of **s**. However, the search process for the closest vertex and the faces can be time consuming especially when the number of triangular faces in the surface D is large. Thus, in our experiment, we use an approximation method. Instead of updating the position of **d** at every iteration, we choose to update it only when the FFD grid is refined, i.e., for a certain FFD grid configuration, the

same correspondence point **d** for **s** is used throughout the optimization process, and thus, point-to-surface distance becomes point-to-point distance, which can be quickly computed. This approximation can be used mainly because the initial matching error between the atlas mesh and the organ surface is already small (sub-millimeter accuracy on average).

Another method to speed up the point-to-surface distance computation is to generate a complete distance map for the surface D (Saito & Toriwaki, 1994). The space containing the surface D is discretized into voxels of $1\text{mm} \times 1\text{mm} \times 1\text{mm}$ in order to achieve submillimetric surface representation accuracy. The distance from each voxel to surface D is computed beforehand. A positive distance is recorded in the distance map for points lying outside the closed surface, and a negative distance is recorded for points lying inside. At registration time, point-to-surface distance is computed by trilinear interpolation within the signed distance map and the absolute value of the result is retained.

5.2.2.3 Optimization

The optimization procedure is done by L-BFGS-B method (Zhu *et al.*, 1997), which is a limited-memory quasi-Newton method for bound-constrained optimization. It can be used to solve minimization/maximization problems with constraints of the form $l \leq x \leq u$. Thus, it enables us to incorporate the diffeomorphic constraint in our scheme which is setting the upper bound of the parameters (the displacement of the FFD grid control points) to be 0.4 times the current control point spacing.

5.3 Experimental Results

5.3.1 Data Description and Experimental Settings

We validate the proposed atlas mesh refinement method on a face atlas FE mesh. The results are presented both qualitatively and quantitatively. To show how the accuracy of the atlas mesh may affect the accuracy of the generated patient FE mesh, we also present qualitative and quantitative results for 20 patient meshes generated from the original and refined atlas meshes. Detailed description of the data used and the patient-specific FE mesh generation procedure can be found in Section 6.3.1 and Section 6.3.2, respectively.

In this experiment, the FFD configuration with initial spacing of 25mm and three grid refinement levels is used. For each FFD grid level, three FFDs with the same control point spacing are used to model large deformation. Therefore, totally nine FFDs are used for the non-rigid transformation. These resulting elementary FFD fields are composed to form the total non-rigid transformation field as in Eq. (4.4). For each FFD, twenty L-BFGS-B optimization iterations are used.

5.3.2 Results for Atlas Mesh

The results for the atlas mesh before and after the refinement are shown in Fig. 5.1 and Table 5.1. From Fig. 5.1 we see that the atlas mesh matches the skin surface in the atlas image better after the refinement. From Table 5.1 we see that by using the proposed method, both the skin and skull surface accuracy of the atlas mesh has been improved.

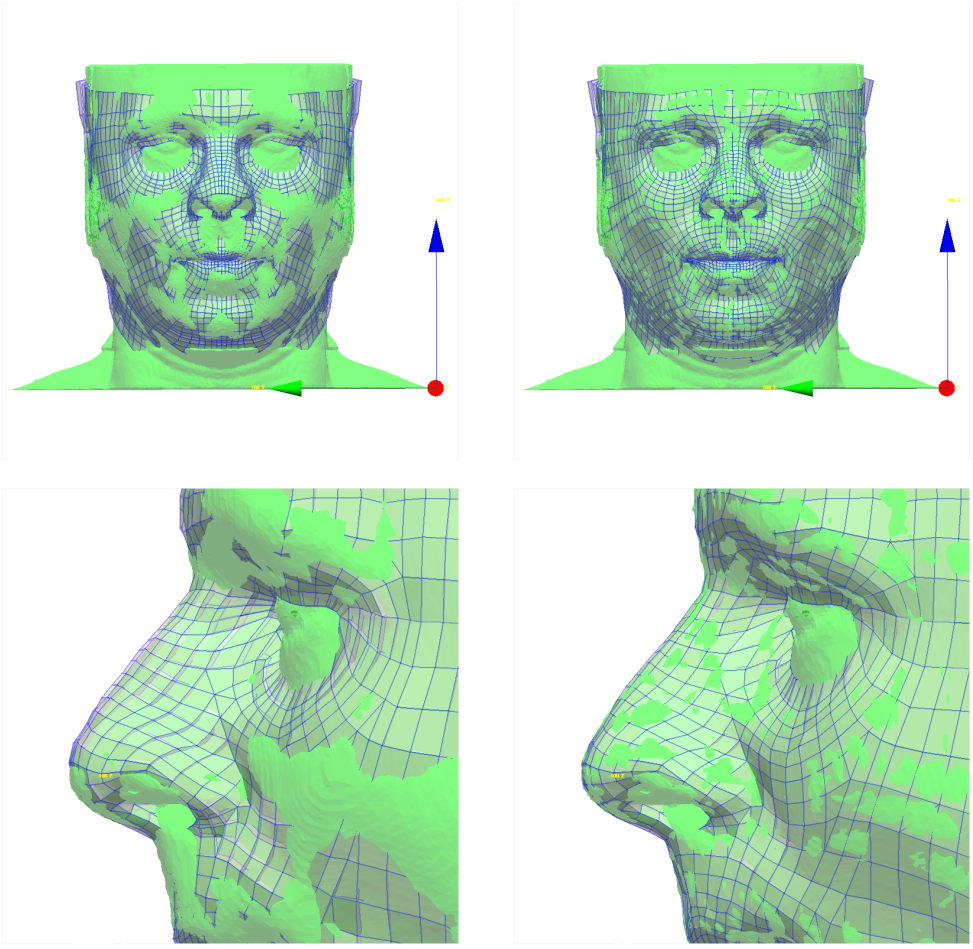

Figure 5.1: Atlas FE mesh before and after the refinement. The transparent atlas FE mesh is shown together with the segmented skin surface (green). For clarity the skulls are omitted. The left column shows figures of the face atlas mesh before the refinement. The right column shows figures of the face atlas mesh after the refinement.

	Mean	Max	σ
Skin error (mm)			
Atlas before	0.5	2	0.4
Atlas after	0.1	2.6	0.2
Bone error (mm)			
Atlas before	0.7	2	0.5
Atlas after	0.3	4.6	0.4

Table 5.1: Surface accuracy for atlas mesh before and after the refinement. Both the skin and skull surface errors are shown.

5.3.3 Results for Patient Mesh

To show how the atlas FE mesh refinement may affect the accuracy of the generated patient-specific FE meshes, we perform our patient-specific FE mesh generation method on 20 patient data sets with both the original and refined atlas mesh. Detailed descriptions of the patient data sets and the mesh generation procedures can be found in Section 6.3.1 and Section 6.3.2, respectively. Surface accuracy statistics for the generated 20 patient FE meshes are shown in Table. 5.2. Samples of generated patient meshes are shown in Fig. 5.2 and Fig. 5.3. From Fig. 5.2, we see that patient meshes generated from the refined atlas mesh match better with the patient skin surface. The results in Table 5.2 show that by using the refined atlas mesh, both the skin and skull surface accuracy of the patient meshes has improved.

In traditional surface registration based mesh morphing methods (Bucki *et al.*, 2010), the atlas mesh is directly deformed to fit with the patient organ surface. Thus, the matching error of the generated patient mesh only comes from the registration error. However, in our scheme, the atlas mesh is deformed implicitly using the transformation derived from atlas and patient image registration.

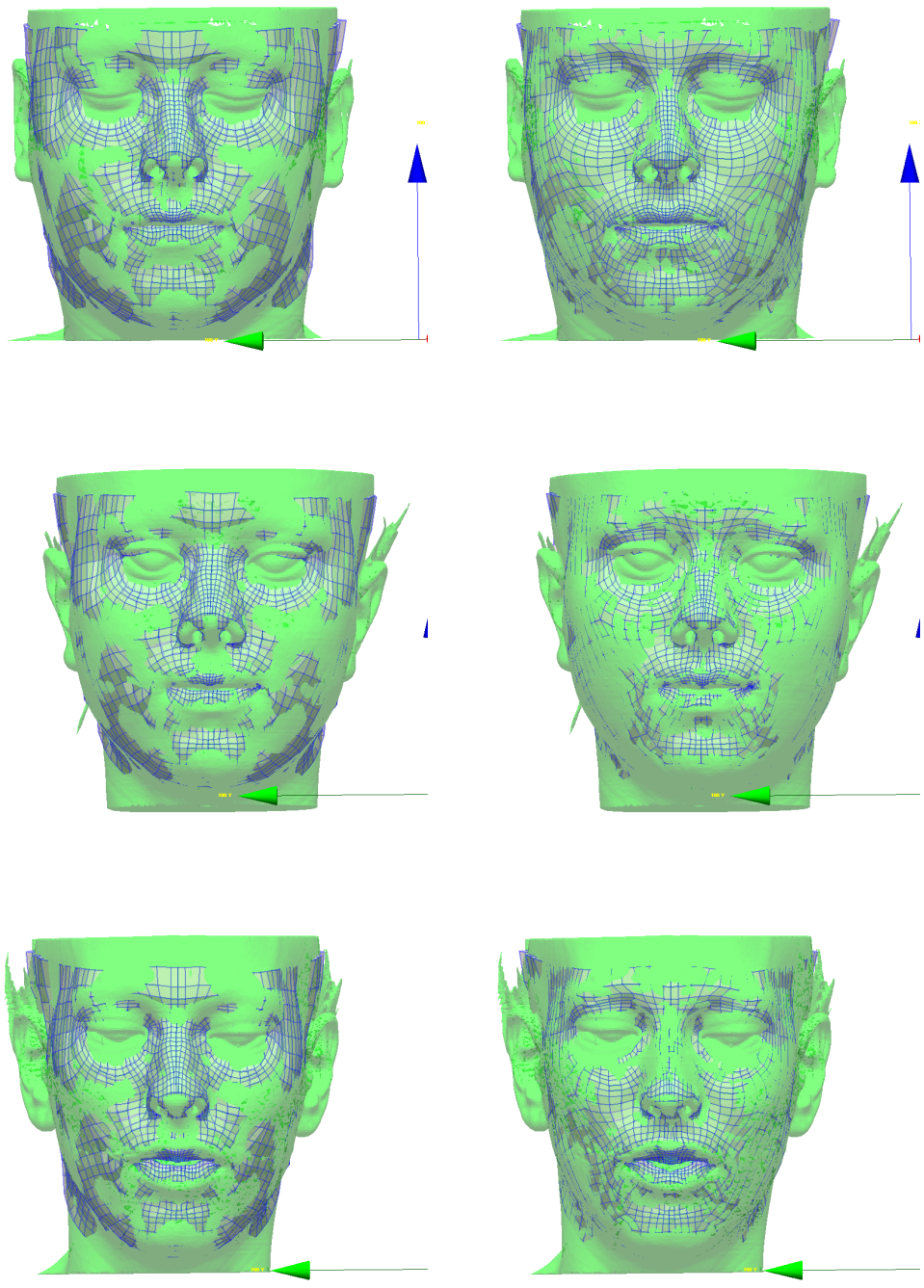

Figure 5.2: Samples of patient FE meshes generated using the original and refined atlas mesh. The transparent patient FE meshes are shown together with the segmented skin surfaces (green). For clarity the skulls are omitted. The left column shows figures of the patient meshes generated using the original atlas mesh. The right column shows figures of the patient meshes generated using the refined atlas mesh.

	Mean	Max	σ
Skin error (mm)			
Patient before	0.6	8.9	0.6
Patient after	0.4	8.7	0.5
Bone error (mm)			
Patient before	0.9	11.4	0.7
Patient after	0.6	10.6	0.6

Table 5.2: Surface accuracy statistics for the 20 patient meshes generated using atlas mesh before and after the refinement. Both the skin and skull surface errors are shown.

Thus, the matching error of the generated patient mesh comes from both the registration error and the atlas matching error. Therefore, with the same degree of registration accuracy, the patient meshes generated with our scheme may have larger surface error. This limitation can be improved by reducing the matching error of the atlas mesh. From Table 5.2 we can see that by using the atlas refinement method in this section, the average skin and skull surface errors of the patient meshes have been reduced to 0.4mm and 0.6mm, respectively, which is the same as that obtained by surface registration based mesh morphing methods as in Bucki *et al.* (2010). This demonstrates that by properly aligning the atlas mesh with the atlas image, our implicit mesh morphing scheme can achieve the same accuracy level as traditional surface registration methods.

From Fig. 5.3, we can see that the patient meshes resulting from the refined atlas mesh are also smoother than results obtained from the original atlas mesh. This is because by closely matching the atlas mesh with the organ surfaces, it is bounded by the real patient skin and skull surfaces which are supposed to be smooth. This will help to improve the jagged mesh surface resulting from the manual mesh generation procedure.

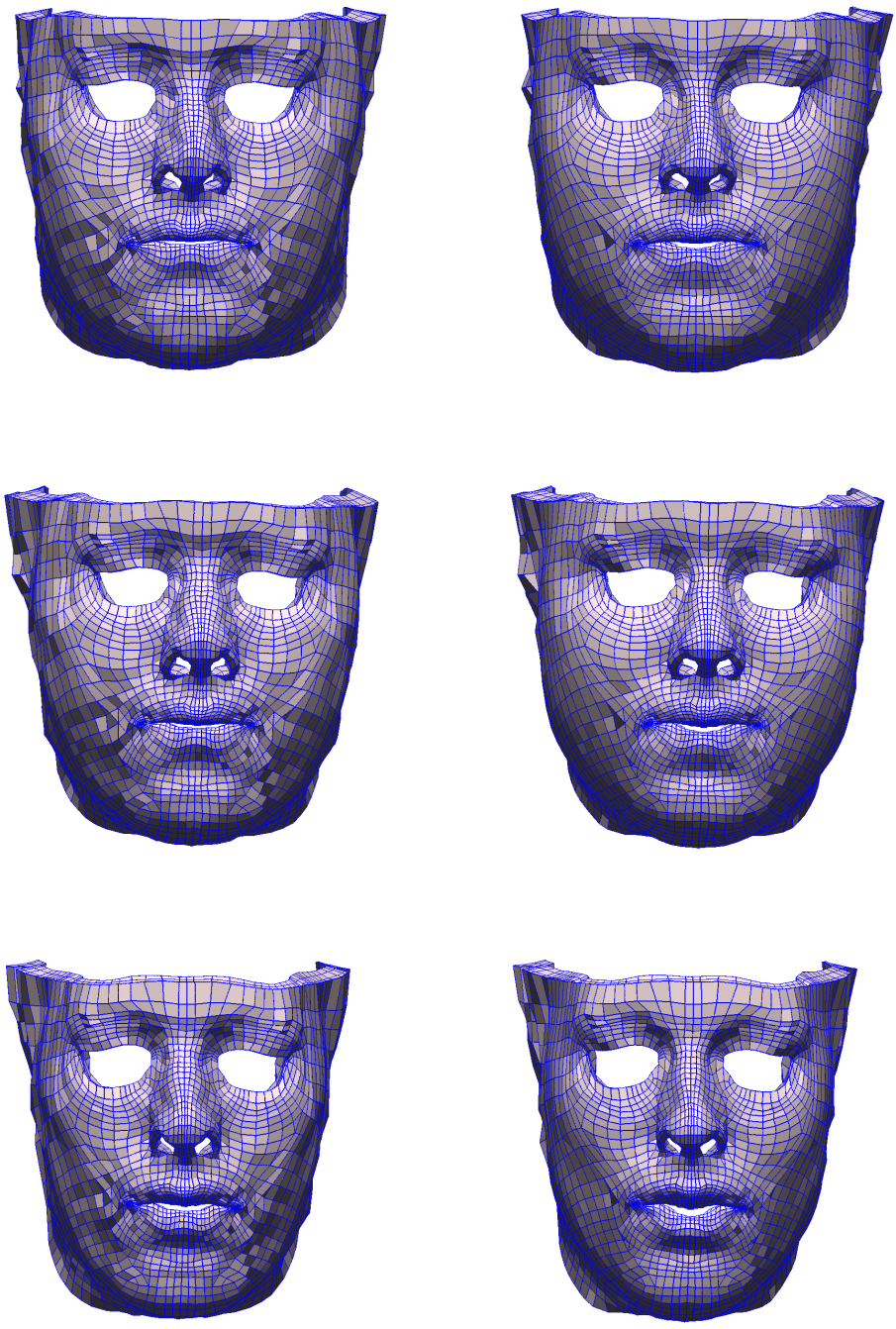

Figure 5.3: Samples of patient FE meshes generated using the original and refined atlas mesh. The left column shows figures of the patient meshes generated using the original atlas mesh. The right column shows figures of the patient meshes generated using the refined atlas mesh.

5.4 Conclusion

In this chapter a point-to-surface registration based atlas FE mesh refinement method is proposed. The method is designed to deform the atlas FE mesh toward the corresponding features in the atlas image in order to reduce the matching error between the atlas mesh and atlas image. This will help to reduce the error carried on from the atlas mesh to the patient meshes. By evaluating the method on a face atlas FE mesh, we demonstrated that the proposed method can effectively improve the representation accuracy of the atlas mesh. We have also shown that with the refined atlas FE mesh, the accuracy of the patient meshes is also improved and achieves the same accuracy level obtained by the direct mesh matching method of Bucki *et al.* (2010).

Chapter 6

Application to Real Clinical Cases

In this chapter, we present the procedures of applying the proposed image registration based mesh morphing scheme to three different clinical cases. Each of these three cases represents a category of problems as described in Section 1.2. The generated mesh accuracy and quality are quantitatively and qualitative evaluated. A comparative study between the results of the proposed scheme and that of the state-of-the-art surface based method is present in Section 6.2.4.3. A quantitative validation of the effectiveness of the proposed regularization term in our scheme is presented in Section 6.2.3.

6.1 Quantitative Assessment Index

In following experiments, the effectiveness of the generated patient-specific FE meshes is quantitatively assessed for two criteria: representation accuracy of the patient's morphology and mesh quality for FE analysis (see definition in Section 6.1.2).

6.1.1 Mesh Accuracy

A subset of the atlas mesh nodes are labeled as anatomical features which need to fit with the anatomical features in the patient data. For example, for the femur model in Section 6.2, the surface mesh nodes are labeled as "bone surface" which need to be matched with the cortical surface of the femur bone in the patient data.

There are also meshes which consist of multiple structures. For example, in the face model in Section 6.3, two groups of mesh nodes are labeled: the exterior surface nodes are labeled as "skin" which are registered onto the patient's face skin, and the interior surface nodes are labeled as "bone" which are registered onto the patient's skulls.

To evaluate the representation accuracy of the generated patient-specific FE mesh, we define a mesh accuracy metric μ, which measures the mean Euclidean distance between the labeled nodes of the generated patient-specific FE mesh and the corresponding patient anatomy surface segmented from patient data. μ is defined as

$$\mu = \sum_{n \in N_{labeled}} d(n, S), \tag{6.1}$$

where n is a node belonging to the labeled nodes collection $N_{labeled}$, S is the corresponding segmented patient anatomy surface, and $d(\cdot, \cdot)$ is the point-to-surface Euclidean distance measure. For meshes with multiple structures, the accuracy of each structure is measured separately.

6.1.2 Mesh Quality

The mesh **regularity** and **quality** are measured as described in Section 4.5 using $|J|$ and JR respectively. In this chapter, in order to measure the patient FE mesh quality w.r.t. the atlas mesh, we introduce another index for each element (Lamata *et al.*, 2011)

$$q^e = \frac{\text{JR}^e_{\text{min/patient}}}{\text{JR}^e_{\text{min/atlas}}}, \tag{6.2}$$

where $\text{JR}^e_{\text{min/patient}}$ is the minimum JR value in element e in the patient mesh, and $\text{JR}^e_{\text{min/patient}}$ is the minimum JR value in element e in the atlas mesh. By defining this index, we choose the minimum JR value for each element to represent its quality, and then compare it with that of the corresponding element of the original undeformed atlas mesh.

Based on above index, we define a single value index measuring the overall mesh quality degradation caused by the registration process as

$$\epsilon = 1 - \bar{q}, \tag{6.3}$$

where $\bar{q}$ is the mean q^e value for all elements e in the FE mesh.

6.2 Femur Model with Synthetic Image Registration

In this section, we evaluate the performance of our scheme on the generation of patient-specific femur FE models. The patient-specific femur FE models can be

used in the context of total knee arthroplasty (TKA) to optimize the prosthesis placement in order to avoid unsealing or femur fracture (Zalzal *et al.*, 2008).

The aim of this section is to validate the application of the proposed method on the clinical cases in level 1 as described in Section 1.2. In these cases, the patient images are first segmented to obtain surfaces or binary images, which are then used in the mesh morphing process. In some clinical situations, the original medical image for the atlas mesh may not be available. For example, the atlas meshes can also be generated from anatomical knowledge and/or from post-mortem data (such as the free available data of the Visible Human project). Thus, to solve this kind of problem using our method, synthetic volume image should be generated from the atlas mesh and then registered with the segmented patient image.

This is the kind of cases discussed in most of existing mesh morphing literatures, where the patient image needs to be segmented before registration. Thus, by validating our method on this case, it also provides a fair basis for comparing the mesh accuracy and quality generated using the proposed scheme with that generated using the state-of-the-art surface based scheme, which is presented in Section 6.2.4.3.

Since the synthetic image is less complex than the real medical image (no noise, intensity inhomogeneities and surrounding organs), the effectiveness of the smoothness term proposed in our scheme is also evaluated on this case in Section 6.2.3.

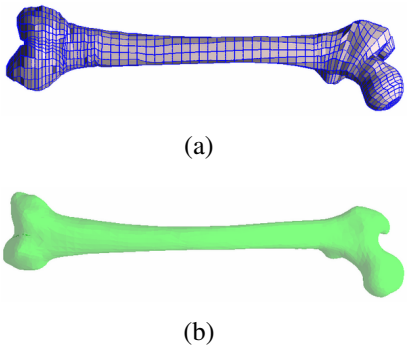

(a)

(b)

Figure 6.1: Femur atlas mesh and segmented patient femur surface. (a) Femur atlas mesh from Couteau *et al.* (1998). (b) Sample of segmented patient femur surface.

6.2.1 Data Description

The manually assembled right femur atlas mesh (Couteau *et al.*, 1998) shown in Fig. 6.1(a) was used in this section. It is made of 4052 nodes forming 3018 elements: 2960 hexahedrons and 58 wedges. The elements are organized so as to reflect the bony structure such as the femoral diaphysis cortex which is discretized by a single layer of elements. The 12 patients' data used in this study are right femur surfaces segmented from CT images as shown in Fig. 6.1(b).

6.2.2 Mesh Generation Procedure

6.2.2.1 Synthetic Volume Image Generation

In this case, the original CT images for the atlas mesh and the patients are not available. To generate patient-specific FE model from the surfaces using our scheme, synthetic binary images with 1mm $\times$ 1mm $\times$ 1mm voxel dimension are generated from both the atlas mesh and the patient surface using surface voxelization method (Patil & Ravi, 2005). Then a $3 \times 3 \times 3$ Gaussian filter is

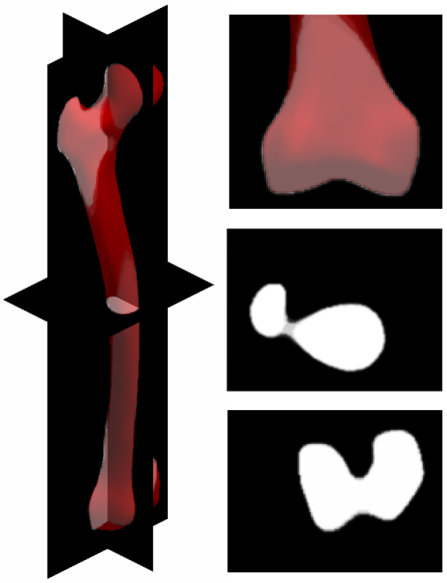

Figure 6.2: Synthetic binary images generation from atlas mesh and patient surface. The left and the top right figures show the samples of patient surface overlaid with generated 3D binary image. The right middle and bottom figures show sample slices of the generated binary images of the femur head and great trochanter respectively.

applied to the generated binary image for antialiasing. A sample of generated binary images are shown in Fig. 6.2.

6.2.2.2 Volume Image Registration

Same voxel size and image resolution for the atlas image and patient image are required in our image registration scheme. Thus, the generated binary images of the atlas and patient are then padded to the same size by adding zero valued voxels after the last array element along each dimension. The resolution of the padded image is determined by choosing the larger resolution among the atlas image and the patient image along each dimension.

The padded images are then pre-aligned by multi-level intensity based affine

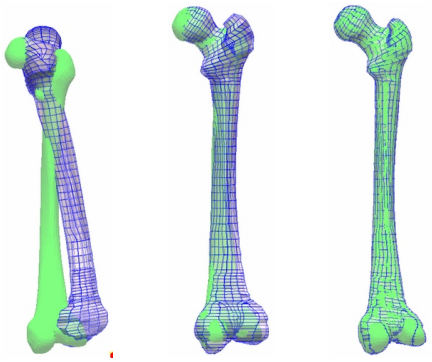

(a) (b) (c)

Figure 6.3: Sample of patient-specific femur FE meshes generation. (a) The atlas mesh and segmented patient femur surface. (b) Deformed mesh fitting the patient femur surface after global affine registration. (c) Deformed mesh fitting the patient femur surface after the non-rigid local registration.

registration as described in Section 4.3.1, where 3 image pyramid levels are used to achieve a faster and more robust registration. After that the non-rigid registration described in Section 4.3.2 is applied, where the patient image serves as the moving image and the atlas image as the fixed image. In both global and non-rigid registration, the SAD similarity metric is used. The 3D displacement field resulting from the registration is then used to deform the atlas mesh to fit with the patient geometry. A sample result of the procedure is shown in Fig. 6.3.

6.2.3 Smoothness Term Effectiveness Evaluation

We first perform a parameter study on the femur model to demonstrate the effectiveness of the proposed smoothness term (Eq. (4.7)) in preserving the quality of the generated mesh. Both the generated mesh accuracy and quality are evaluated w.r.t. different smoothness term weighting parameter λ values in Eq. (4.8),

which also provides information for parameter value selection in future clinical applications.

The experiment is performed on the femur model as it uses a synthetic image and thus, because this image contains only one homogeneous object, the registration will not be affected by surrounding organs, noise and intensity inhomogeneity. Most importantly, since the atlas image has been generated from the atlas mesh (and not the other way around, as illustrated in Section 6.3 on the face model) the atlas image fits perfectly the atlas FE model which makes it possible to assess the effects of non-linear registration alone, i.e., without the combined errors introduced by a possible mismatch between the atlas FE model and the atlas image.

There are two regularity constraints in our scheme for preserving the quality of the generated mesh. The diffeomorphic constraint is used to prevent the generated deformation field from folding while the smoothness term in Eq. (4.7) is used to limit excessive space distortion. The smoothness parameter λ in Eq. (4.8) constrains the weighting of the smoothness term and thus the smoothness of the overall displacement field.

The experiments were conducted on 4 randomly selected patients. The FFD configuration is set to be optimal with 15mm initial control point spacing with 3 FFD grid refinement levels. The value of λ is dependent on the similarity metric used. For the SAD metric used in this section, we consider 9 different values for lambda $\{0, 10, 25, 50, 100, 200, 400, 600, 800\}$. The overall accuracy and quality of the generated mesh is measured using μ in Section 6.1.1 and ϵ in Eq. (6.3), respectively. Fig. 6.4 shows the mesh surface error and quality degradation for the 4 patients w.r.t. different λ values.

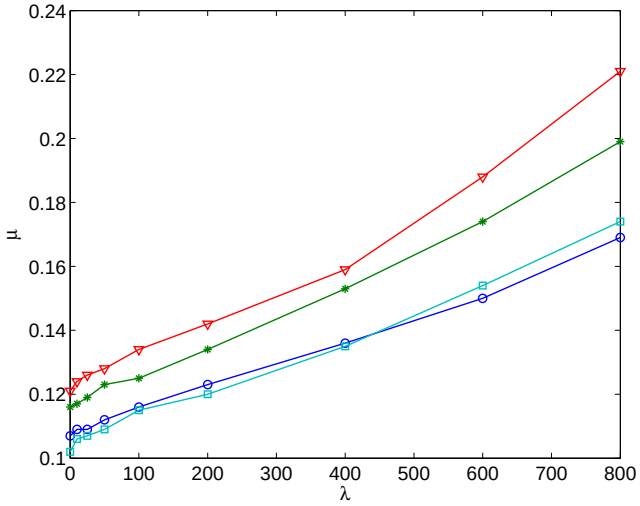

(a)

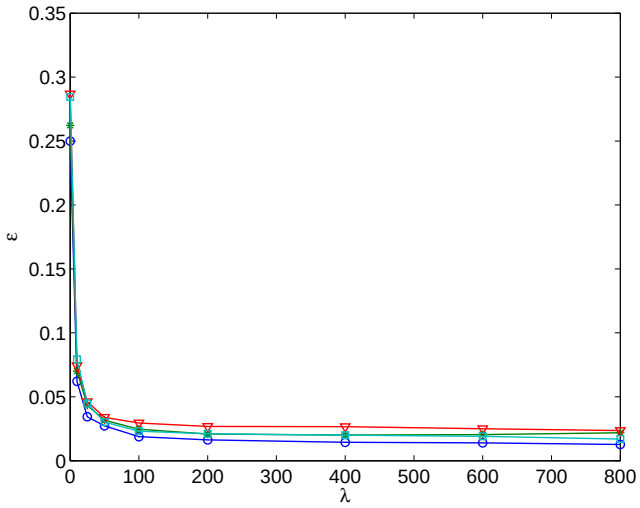

(b)

Figure 6.4: The results for 4 patients w.r.t. different smoothness parameter λ values. (a) Surface error μ for 4 patients. (b) Mesh quality degradation ϵ for 4 patients.

The higher the value of λ is, the smoother the deformation field, and thus better mesh quality. However, when the deformation tends to be smooth, it will not be able to model some local morphological differences, resulting in less accurate representation of organ shape. From the results, we can see that the surface error increases linearly with λ while the mesh degradation drops quickly at first and then tends to stabilize at $\lambda = 100$ around a value close to zero, which means the mesh quality of the generated patient mesh is quite close to the mesh quality of the atlas mesh. This suggests that the optimal λ value should be the *threshold* value (in this case, $\lambda = 100$) that make the mesh quality degradation converge.

By using the proposed smoothness term with appropriate weighting, results show that the proposed smoothness term in our scheme can effectively reduce **unnecessary mesh distortion**, i.e., the part of distortion that is not required for an accurate mesh matching. By choosing the optimal smoothness parameter, the quality degradation index value drops more than 90% compared to no smoothness constraint and there is little influence on the mesh accuracy (less than 0.02mm). Fig. 6.5 shows a sample of how the smoothness term affects the generated mesh quality visually. As can be seen, the distortion of the generated mesh is well controlled due to this smoothness term.

6.2.4 Results

6.2.4.1 Quantitative Evaluation

The proposed scheme is evaluated on 12 patients. The smoothness parameter $\lambda = 100$ and 15mm initial control point spacing with 3 grid refinement levels

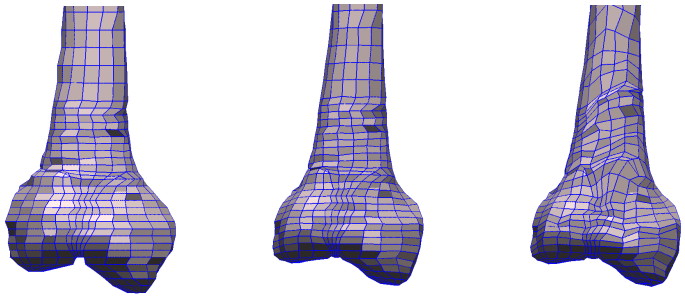

(a) (b) (c)

Figure 6.5: Sample of how the smoothness term affects the generated mesh quality. (a) The atlas mesh. (b) The generated patient-specific mesh with optimal smoothness parameter $\lambda = 100$ as in Section 6.2.3. (c) The generated patient-specific mesh without smoothness constraint. Both (b) and (c) use the same FFD configuration and other parameters. Through the proposed smoothness term, the unnecessary mesh distortion is well controlled.

are used. The generated meshes are quantitatively evaluated from both accuracy and quality aspects. The statistical results are shown in Table 6.1, Table 6.2 and Fig. 6.7.

For each external FE node the surface representation error is estimated as the minimal Euclidean distance from the considered node to the pre-segmented surface of the patient femur. The mean surface representation error is computed as the mean value of all surface representation errors for all surface nodes in a given mesh. The results demonstrated that our scheme can achieve submillimetric representative accuracy. The reported mean and maximal errors are the mean and maximal error computed for the entire patient's dataset.

The most time-consuming step in our mesh morphing scheme is the non-rigid image registration step. The computational time of this step is mainly affected by the size of images and the FFD configuration. In this experiment, we used images with a resolution of $170 \times 170 \times 550$, along with 15mm initial

	Mean	Max	σ
Error_image (mm)	0.1	2.6	0.2
Non-rigid registration (s)	329	408	51
Error_surface (mm)	0.3	6.6	0.5

Table 6.1: The accuracy and registration time statistics for the 12 patient-specific meshes generated by image based method proposed in this thesis. For comparison, the accuracy of the meshes generated by the surface based method (Bucki *et al.*, 2010) are also shown as Error_surface.

control point spacing and 3 refinement levels for the FFD configuration. The non-rigid registration process for each patient is completed within 4-7 minutes, which is acceptable for real clinical applications. The subsequent atlas mesh morphing process takes less than 10 seconds.

The quality of the generated FE meshes is measured using the Jacobian Ratio indicator, as discussed in Section 4.5. The minimum nodal Jacobian Ratio for each element is chosen to represent the quality of that element. The mean element quality distribution for the 12 patient-specific FE meshes is reported in Table 6.2 and Fig. 6.7. For this study, it was decided to classify the elements into 6 quality intervals (Table 6.2, Table 6.4, Fig. 6.7 and Fig. 6.11). Elements with Jacobian Ratio smaller than 0.03 are considered problematic (if JR < 0 the element is irregular; $0 <$ JR < 0.03 means that the element is in poor quality) and are not suitable for FE analysis. The quality of the generated patient FE meshes is compared with that of the atlas mesh. From the results we can see that the patient-specific femur FE meshes generated using the proposed method show only a slight quality degradation compared to the atlas mesh, i.e., 0.5% problematic elements (irregular and poor quality) and less than 2% changes in each Jacobian Ratio interval.

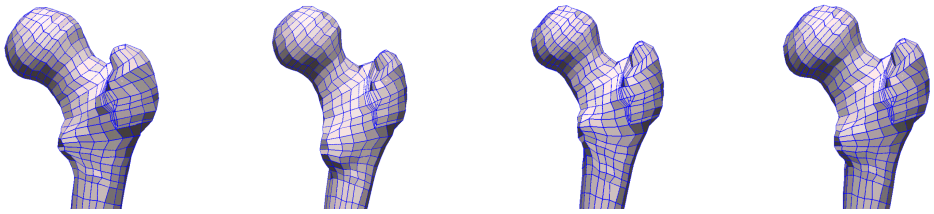

Figure 6.6: Four examples of the generated femur models. The zoom-in images on femur head are shown to illustrate the variety of patient in the data base.

6.2.4.2 Qualitative Evaluation

Fig. 6.6 shows samples of zoom-in images on femur heads of four generated patient-specific femur FE meshes. As we can see, the proposed method successfully generated patient-specific FE meshes for patients with very different local morphologies, which demonstrated that our method can effectively adapt to the anatomical variety of patients.

6.2.4.3 Comparative Study

This experiment is segmentation based, and thus can also be solved using existing surface registration based methods. The surface registration based mesh morphing scheme has been tested on 60 clinical cases (Bucki *et al.*, 2010), and proved successful in automatic generating high quality patient-specific FE meshes. Since we used the same atlas femur FE mesh as in Bucki *et al.* (2010), we compare the accuracy and quality of the FE meshes generated using the new image based scheme with the original surface based scheme. The results are shown in Table 6.1, Table 6.2 and Fig. 6.7. Generally speaking, the proposed image based scheme outperforms the surface based scheme in both mesh ac-

JR	< 0.03	$0.03 - 0.2$	$0.2 - 0.4$	$0.4 - 0.6$	$0.6 - 0.8$	$0.8 - 1.0$
Atlas (%)	0.0	4.6	21.0	38.3	22.7	13.4
Image (%)	0.5	5.1	21.0	38.4	23.2	11.7
Surface (%)	0.8	5.2	22.1	38.0	24.1	9.8

Table 6.2: Mesh quality distribution for atlas mesh, the patient-specific meshes generated by the surface based method (Bucki *et al.*, 2010) and the image based method proposed in this thesis. For the patient meshes, the mean ratio is shown for each quality interval.

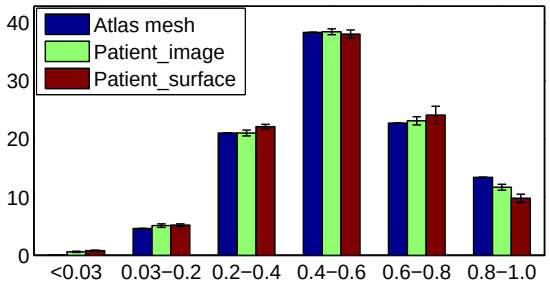

Figure 6.7: Mesh quality distribution for atlas mesh, the patient-specific meshes generated by the surface based method (Bucki *et al.*, 2010) and the image based method proposed in this thesis. For the patient meshes, the mean ratio is plotted for each quality interval, along with the standard deviation among the patients.

curacy and quality. In our scheme, the proportion of elements in each quality interval is closer to that in the atlas mesh, thus showing less degradation compared to Bucki *et al.* (2010). This improvement is more obvious for the high quality elements, i.e. the interval $[0.8 - 1.0]$.

6.3 Face Model with Mono-modal Image Registration

Patient-specific face FE model can be used in orthognathic surgery, where FE analysis helps predict the consequences of the intervention on the patient's fea-

ture and facial expressions by simulating the effects of the repositioning of the jaw, maxillary or malar bones (Chabanas *et al.*, 2003; Luboz *et al.*, 2005).

The second experiment demonstrates the application of the proposed scheme in generating patient-specific face FE models directly from patient CT images without segmentation. This kind of problem corresponds to the problems in level 2 as described in Section 1.2, where volume medical images for both the atlas patient are available and of the same modality.

In this case the approach is different from the first experiment and previous surface or landmarks based method, as in this experiment we generate patient-specific FE meshes directly from actual patient CT images without resorting to CT image simulation from the segmented surface as we did for the femurs. (see Section 6.2). This case illustrates perfectly our approach as the patient anatomical surfaces do not need to be segmented (In this experiment, the skin and bone surfaces of the patients are only segmented for the quantitative evaluation of the representation accuracy of the generated patient meshes.) A set of 20 patients' head CT images was used in this experiment to embrace the variety of different morphologies.

6.3.1 Data Description

In this experiment, we used a manually assembled (Nazari *et al.*, 2008) 3-layer atlas mesh (Fig. 6.8). It is constructed from a selected atlas CT image. This atlas mesh is designed to replicate the anatomical structure of the face epidermis, dermis and fat/muscle layer using only hexahedrons and wedges and takes into account boundary conditions (attachment of the inner nodes to the corre-

sponding skull bones). It comprises 8720 nodes forming 6342 elements: 6024 hexahedrons and 318 wedges. As we wish to model the interaction between face bones, muscles and features, the patient-specific FE model must fit both the skin and bone surface in the CT images. Therefore, the atlas external and internal layer nodes are labeled as "skin" and "bone" which fit to the skin and bone surface in the atlas CT image, respectively. The mesh was designed for orthognathic surgery, and thus some irrelevant areas such as the ears are absent from the atlas mesh, and the sphenoid bone and zygomatic process regions have very approximative representations in the mesh.

In this experiment, the original atlas and patient CT images are used in mesh generation without segmentation. The resolution of the atlas CT image is $512 \times 512 \times 150$ with a voxel spacing of $0.49\text{mm} \times 0.49\text{mm} \times 1.29\text{mm}$. The resolution of the patient images is $512 \times 512 \times N$, where N is number of the axial slices, which varies according to patient head size. The voxel spacing of the patient images is $0.48\text{mm} \times 0.48\text{mm} \times 0.75\text{mm}$.

6.3.2 Mesh Generation Procedure

In the first step, the regions of interest in the atlas and patient CT images are manually selected to make sure that both images share similar content and cover the region of the mesh that we want to generate (the face region in this case). Here, the full head CT image is used, except that the upper part of the head that is removed as it does not include the face. Since a too large region of interest will result in longer registration time, the image can be further trimmed to just enclose the anterior part of the head image, and a mask generated from

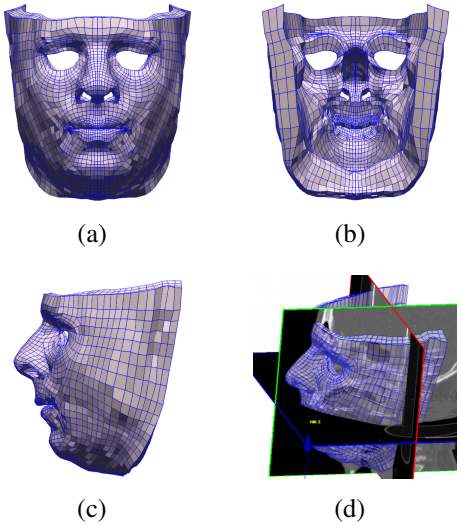

Figure 6.8: Face atlas FE mesh. (a) Anterior view. (b) Posterior view. (c) Lateral view. (d) Atlas mesh shown with atlas CT image.

the atlas mesh can also be used in the registration process so that the similarity measure is only computed in the mask region. The atlas and patient CT images are then resampled to give an isotropic voxel of dimension 0.8mm $\times$ 0.8mm $\times$ 0.8mm (i.e., the geometric mean value for the intra-plane pixel spacing and the inter-plane slice spacing of the atlas CT image), and padded to the same resolution as $339 \times 339 \times 241$. The atlas and patient images are then registered by the volume registration method described in Section 4.3, where the patient image serves as the moving image and the atlas image as the fixed image. The optimal registration parameters are set as $\lambda = 200$, and 25mm initial control point spacing with 3 grid refinement levels are used. The 3D displacement field resulting from the registration is then used to deform the atlas mesh to fit with the patient geometry. A sample result of the procedure is shown in Fig. 6.9.

Since the face FE meshes are supposed to match both skin and skull surfaces, surface representation accuracy of the generated FE meshes is measured for

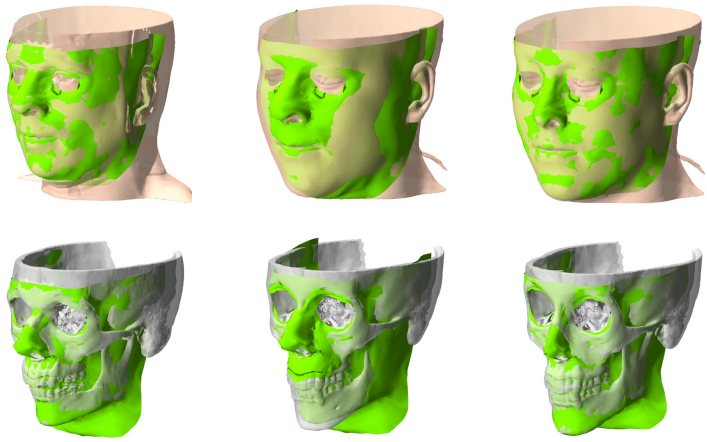

Figure 6.9: Example of a patient-specific FE face meshes. To illustrate skin and bone surface representation, external and internal surfaces (green) of the FE meshes are shown along with the patient's skin and bone surfaces segmented from the CT images. The first column shows the atlas mesh and segmented atlas skin and bone surface. The second column shows the deformed mesh fitting the patient skin and bone surface after global similarity registration. Third column shows the deformed mesh fitting the patient skin and bone surface after the non-rigid local registration.

both skin and skull. The skin surface error is measured as the mean Euclidean distance between the external surface nodes of the FE mesh and the nearest point on the patient's skin surface reconstructed from the CT images; while the skull surface errors are similarly measured as the mean Euclidean distance between the internal surface nodes of the FE mesh to the nearest point on the patient's skull surface. The quality of the generated patient-specific FE meshes is measured as described in Section 4.5.

6.3.3 Results

6.3.3.1 Quantitative Evaluation

The proposed scheme is evaluated on 20 patients. The statistical results are shown in Table 6.3, Table 6.4, Fig. 6.10 and Fig. 6.11, and the samples of gen-

erated patient-specific face FE meshes are shown in Fig. 6.12. From Table 6.3 we can see that patient-specific FE meshes generated using our scheme achieve submillimetric representation accuracy for both skin and skull surfaces. The mean surface error in this experiment is larger than that of the femur case (the mean surface error for femur model is 0.1mm). This is probably due to the fact that part of the representation error of the generated meshes is inherited from the atlas mesh.

Indeed, in the femur model case, where the images used for registration were directly generated from the atlas mesh and patient anatomy surface, there was a perfect match between the atlas mesh and the atlas image. Therefore, the error shown in the femur case is exclusively caused by the registration process, and as demonstrated using the optimal parameters, this error can be very small (0.1mm).

In the face model case, although the atlas is generated from the CT image. Since it was decided to approximate the mesh representation in some unimportant regions such as the ear, sphenoid bone and zygomatic regions, there are some errors between the surface of the atlas mesh and the surface reconstructed from the atlas CT image (Table 6.3 and Fig. 6.10). By deriving the 3D displacement field from the image registration, this error is passed on to the patient's meshes. Thus, the representation accuracy of the patient specific mesh is dependent on the representation accuracy of the atlas mesh. If an accurate and high quality atlas mesh is used, accurate and high quality patient specific meshes can be generated. A strong point of our technique is that the detailed atlas meshing process only needs to be done once, and it can be incrementally refined without altering the mesh generation process or re-computing the deformation field.

	Mean	Max	σ
Skin error (mm)			
Atlas	0.1	2.6	0.2
Patient	0.4	8.7	0.5
Bone error (mm)			
Atlas	0.3	4.6	0.4
Patient	0.6	10.6	0.6
Non-rigid registration (s)	133	139	2.5

Table 6.3: Surface accuracy and registration time statistics for the 20 patient-specific meshes. The accuracy of the generated patient meshes is compared with that of the atlas mesh.

Thus, any refinement in the atlas mesh can be immediately transferred to patient meshes with zero extra effort.

Fig. 6.10 shows the error distributions for the atlas mesh, and the average surface error distributions for the generated 20 patient meshes. The latter is computed by averaging the surface errors for the corresponding mesh surface nodes of the 20 patient meshes. Both the atlas and patient average surface error distributions are plotted on the atlas skin and skull surface for comparison of the geometrical location of the errors. Generally speaking, the error distributions of the atlas and the patient meshes are very similar. Most of the large errors in the patient meshes appear in the ear region which is normal since ears are absent from the atlas mesh (Fig. 6.8).

The image resolution in this experiment is $339 \times 339 \times 241$. The number of FFD control points is less than that of the first experiment due to larger initial control point spacing and smaller image physical region. Thus, it leads to a shorter registration time. The full process can be finished in less than 3 minutes (Table 6.3), as opposed to $4 - 7$ minutes in the case of the femur.

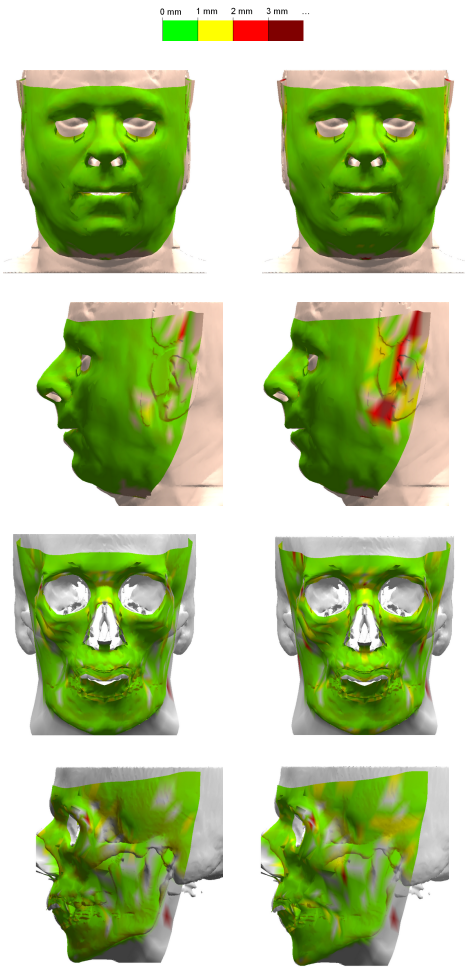

Figure 6.10: The atlas and 20 patients' average surface error (skin and skull) distributions shown as color maps on the atlas skin and skull surfaces. The left column shows the atlas skin and skull errors from anterior and lateral views. The right column shows the average skin and skull errors computed for all the 20 patients, from anterior and lateral views.

JR	< 0.03	$0.03 - 0.2$	$0.2 - 0.4$	$0.4 - 0.6$	$0.6 - 0.8$	$0.8 - 1.0$
Atlas (%)	0.0	8.4	19.3	37.5	30.7	4.1
Patient (%)	0.8	6.9	20.4	39.1	29.5	3.4

Table 6.4: Mesh quality distribution for atlas mesh and the patient-specific meshes generated by the method proposed in this thesis. For the patient meshes, the mean percentage of different JR interval is shown.

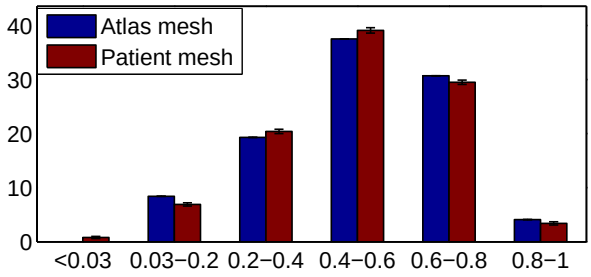

Figure 6.11: Mesh quality distribution for the atlas mesh and patient-specific meshes generated by the proposed method. For the patient meshes, the mean percentage of different JR interval is plotted, along with the standard deviation among the patients.

The quality statistics of the patient-specific meshes are compared with those of the atlas mesh (Table 6.4 and Fig. 6.11). From these results we can see that the qualities of the patient-specific meshes are very close to the quality of the atlas mesh with only a slight degradation, i.e., 0.8% irregular or poor quality (JR < 0.03) elements and less than 2% variation in the quantity of elements in each JR interval. Mesh quality indicator values measured for different patients are also consistent as the standard deviations shown are quite small ($\sigma < 1\%$).

6.3.3.2 Qualitative Evaluation

Fig. 6.12 shows the thumbnails of 20 patient-specific face FE meshes. In this database, the retrognathic cases, "average" patients as well as prognathic morphologies were included. In all cases, the patient-specific meshes were success-

fully generated and fitted within submillimetric accuracy to the patients' morphologies, which demonstrated that our scheme is sufficiently robust to tackle a wide spectrum of morphological varieties. Once the small fraction (less than 0.8%) of problematic elements are untangled (Bucki *et al.*, 2011), the generated FE meshes are suitable for FE analysis.

6.4 Face Model with Multi-modal Image Registration

The aim of this section is to validate the application of the proposed method on the clinical cases in level 3 as described in Section 1.2, where atlas and patient medical images are of different modality. In this case, multi-modal image registration is required. Due to the optimization method used, our method can encode any similarity measure without customization of optimization method, which makes it convenient to extend our scheme to multi-modality registration.

This feature is of interest, as for an atlas mesh build on a certain image modality, for example CT image, different patient image modality can be used (CT or MRI). This give the clinicians more freedom to choose the appropriate image modality for different patients, as certain image modality may not be available for some patient. For example, CT is not a preferred modality for routine anatomical imaging for structures in the head because of the X-ray exposure of the subject, while people with heart pacemakers cannot undergo MRI due to the strong magnetic field used.

The shape information contained in one image modality along with the

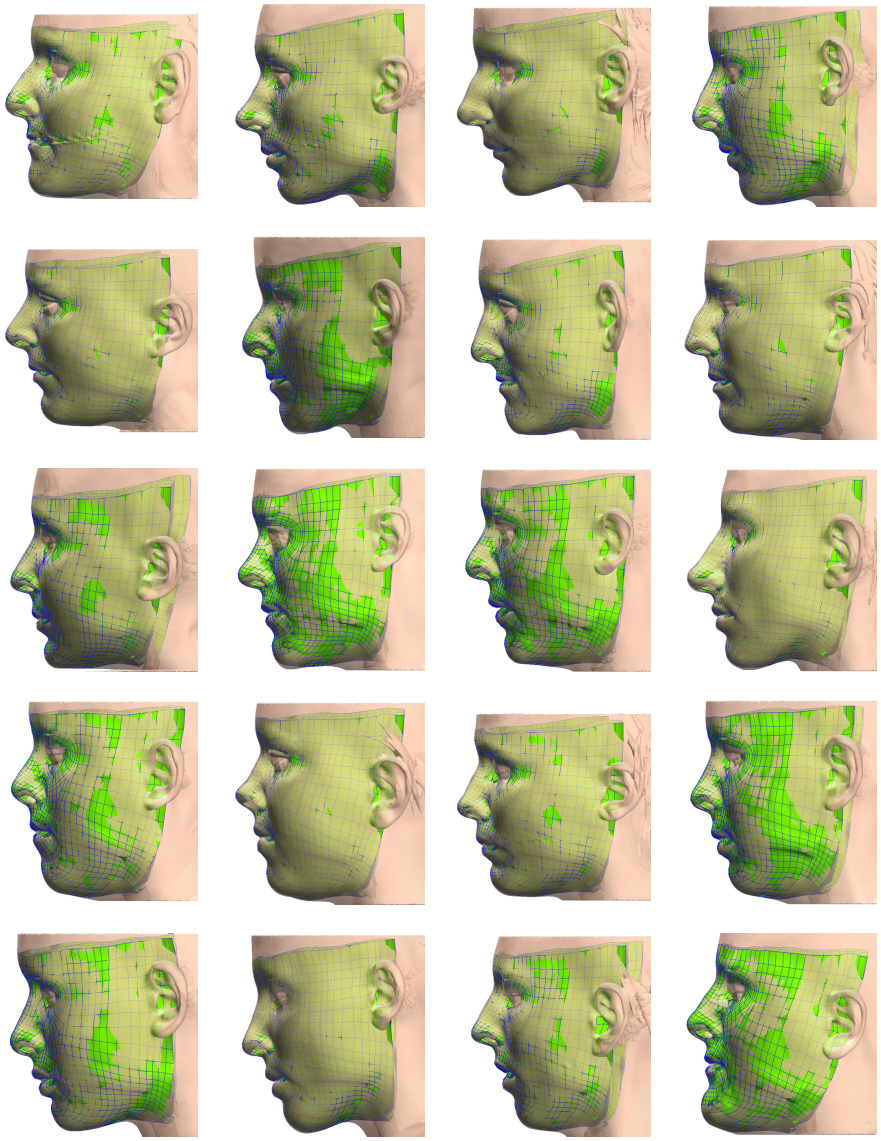

Figure 6.12: Thumbnails of 20 generated patient-specific FE meshes. The patient-specific FE meshes are shown together with the transparent skin surface of the patient. For clarity the skulls are omitted.

smoothness constraints in the registration scheme may also help to define the shape in another image modality which is otherwise hard to obtain. For example, for the face model in this experiment, it is almost impossible to generate patient mesh based on MR image of the patient using traditional methods, as it is quite difficult to get a clear segmentation of the skull from the MR image due to the weak MR signals produced in bone. However, in our scheme, by register the CT image of the atlas with the MR image of the patient using multi-modality similarity metric, the patient mesh can be generated.

6.4.1 Data Description

In this experiment, the atlas mesh and atlas image are the same as described in Section 6.3.1. The resolution of the patient MR images is $352 \times 512 \times 160$ with voxel spacing of 0.4883mm $\times$ 0.4883mm $\times$ 1mm.

6.4.2 Mesh Generation Procedure

6.4.2.1 MR Image Denoising and Enhancement

As mentioned in Section 2.3.2, MR images are often corrupted by severe Rician noise. Thus, before volume image registration, the patient images are first pre-processed using the method in Chapter 3. Assuming that the Rician noise is evenly distributed in the volume image, the automatic parameter estimation in Section 3.3 is performed on a 2D slice selected from the volume image to reduce the optimization time. In this case, an axial slice located at the mandible region is selected as it contains bone, muscle and fat tissue, thus can serve as a good simulation for the volume image. The classification parameters in the

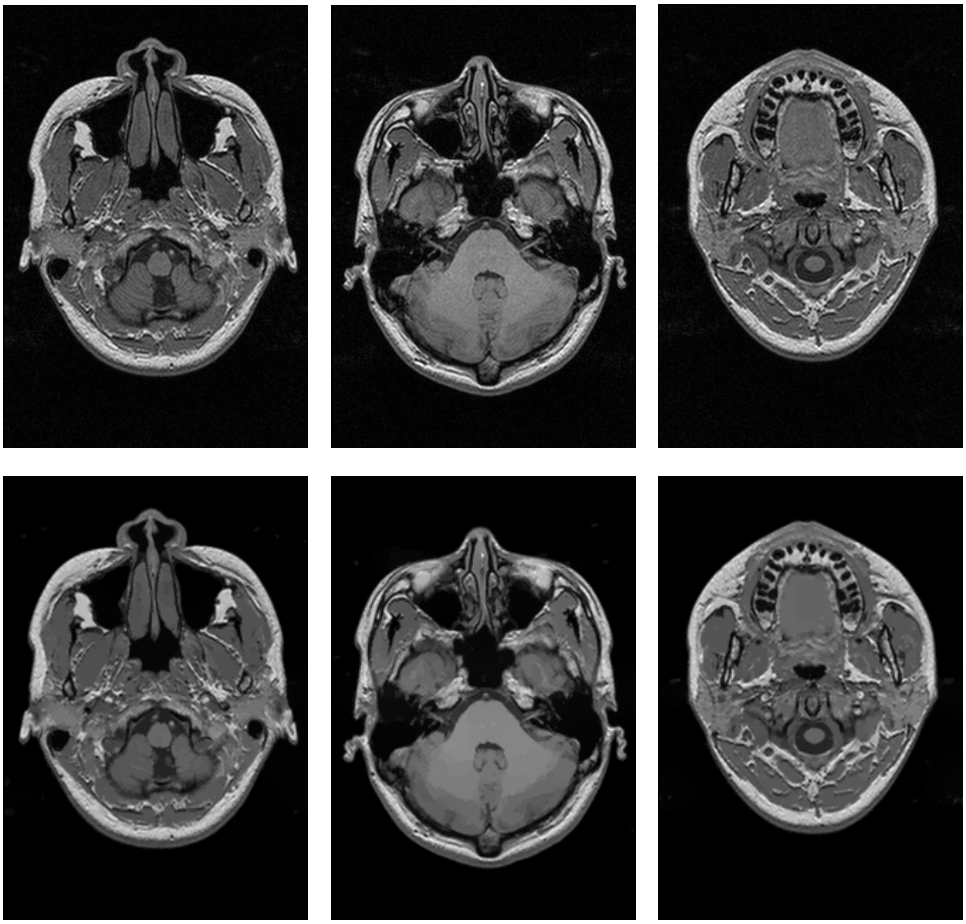

Figure 6.13: Samples of preprocessing results of the patient MR images. The upper row shows the orginal image. The lower row shows the images after the preprocessing.

paramter optimization scheme are set as follows: neighborhood factor $\nu = 0.7$ and prototypes $V = \{0; 40; 100; 150; 200\}$ based on the observation of the main intensity groups in the image. The de-noising method is then applied to the entire volume image with the estimated parameter values. Sample results are shown in Fig. 6.13. We can see that, through the proposed method, the noise in the MR images are effectively removed, and the contrast of the images is also improved.

6.4.2.2 Volume Image Registration

The regions of interest in the atlas CT image and patient MR image are manually selected as described in Section 6.3.2. The images are then resampled to give an isotropic voxel of dimension 0.8mm $\times$ 0.8mm $\times$ 0.8mm, and padded to the same resolution $339 \times 339 \times 241$.

Unlike the previous two experiments, the atlas and patient images used in this experiment are of different modalities. Thus, the multi-modal similarity metric NMI in Eq. 4.5 is used. The number of intensity bins used for the estimation of probabilities is set as 64. The images are first globally registered using a multi resolution affine registration method, with the gradient descent optimization scheme described in Section 4.3.1. The calculation of the mutual information is based on the method introduced by Mattes *et al.* (2001); Thevenaz & Unser (2000). The resulting images are then registered by the non-rigid registration scheme described in Section 4.3.2, where $\lambda = 0.1$ and 40mm initial control point spacing with 3 grid refinement levels are used. The 3D displacement field resulting from the registration is used to deform the atlas mesh.

6.4.3 Results

6.4.3.1 Quantitative Evaluation

The proposed scheme is evaluation on four MRI datasets. The statistical results are shown in Table 6.5, Table 6.6, Fig. 6.14. As it is quite difficult to get a clear segmentation of the skull from the MR images due to the weak signals produced in bone, the accuracy of this case is only evaluated on the skin surface. From Table 6.5, we can see that patient-specific meshes generated using multi-modal

	Mean	Max	σ
Skin error (mm)			
Atlas	0.1	2.6	0.2
Patient	0.4	8.7	0.6
Non-rigid registration (s)	1016	1035	16

Table 6.5: Surface accuracy and registration time statistics for the 20 patient-specific meshes. The accuracy of the generated patient meshes is compared with that of the atlas mesh.

JR	< 0.03	$0.03 - 0.2$	$0.2 - 0.4$	$0.4 - 0.6$	$0.6 - 0.8$	$0.8 - 1.0$
Atlas (%)	0.0	8.4	19.3	37.5	30.7	4.1
Patient (%)	0.7	7.9	19.7	38.1	29.8	3.9

Table 6.6: Mesh quality distribution for atlas mesh and the patient-specific meshes generated by the method proposed in this thesis.

image registration achieved submilimetric representation accuracy for patient's skin surface. The resulting mean surface error and standard deviation is quite close to that obtained using mono-modal image registration as in Table 6.3, which demonstrates the effectiveness of the proposed multi-modal scheme.

The average non-rigid registration time in this experiment is 16min, as opposed to 5min and 3min in previous two experiments. The computational time is longer mainly because the NMI similarity metric used in this experiment is more computationally expensive than the SAD used previously.

The quality statistics of the generated patient-specific meshes are compared with that of the atlas mesh as in Table 6.6 and Fig. 6.14. The generated meshes show little degradation as compared to the atlas mesh with 0.7% problematic elements and less than 2% degradation for each JR interval.

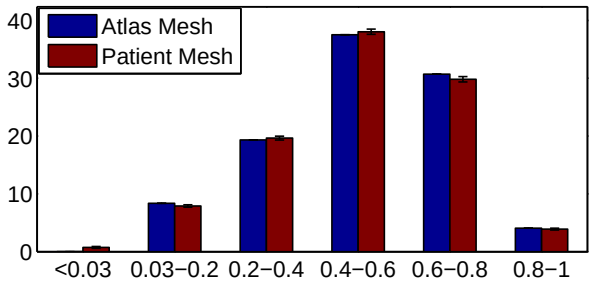

Figure 6.14: Mesh quality distribution for the atlas mesh and patient-specific meshes generated by the proposed method. For the patient meshes, the mean percentage of different JR interval is plotted, along with the standard deviation among the patients.

6.4.3.2 Qualitative Evaluation

The representation accuracy of the bone surface cannot be evaluated quantitatively; thus, it is evaluated visually in this experiment (Fig. 6.15). From Fig. 6.15, we can see that although the bone in MR images is quite difficult to segment, by using our multi-modal registration method, we can still generate a patient-specific mesh that match closely with the patient's bone structures. Four samples of generated patient meshes are shown in Fig. 6.16 together with the segmented patient skin surface.

6.4.3.3 Comparative Study

Generating FE models from MR images is of interest as MRI is able to simultaneously capture and depict bony and soft tissue structures, and the patient does not need to go through multiple imaging processes. It is preferred in clinical applications as it is more flexible and is radiation free.

To generate FE meshes from MR images, in traditional surface based mesh generation method, the bone structures need to be segmented from the patient

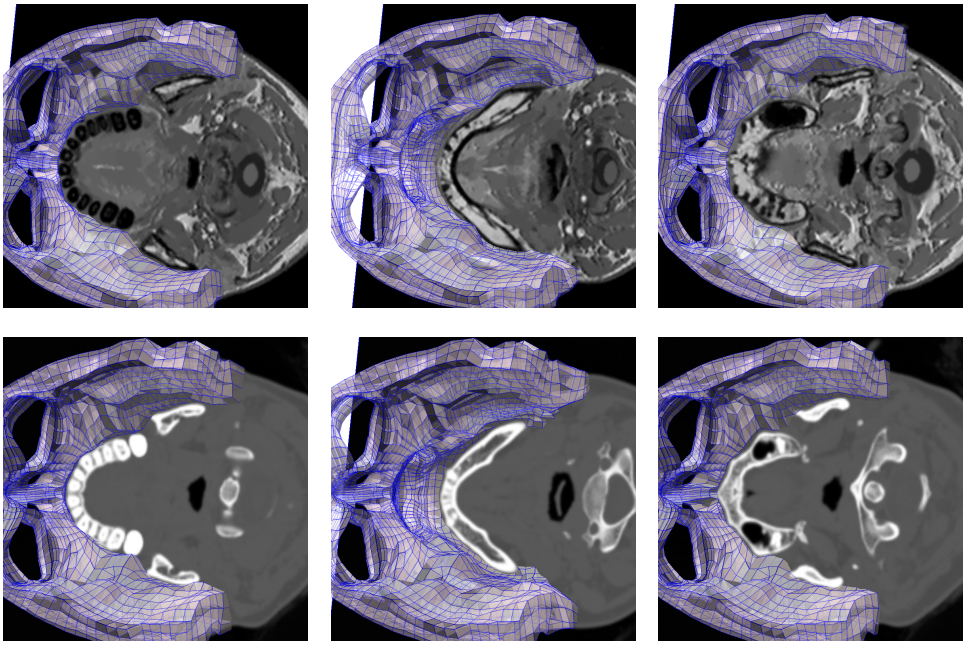

Figure 6.15: Qualitative evaluation of the bone representation accuracy. The generated patient mesh is overlaid with paitent image. From left to right, the fitness of the teeth, mandible and maxillary are shown. The mesh generated using CT images with mono-modal image registration in Section 6.3 is shown in the second row for comparison.

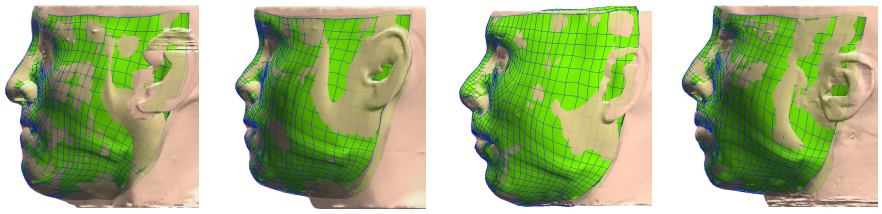

Figure 6.16: Thumbnails of 4 generated patient-specific FE meshes. The patient-specific FE meshes are shown together with the transparent skin surface of the patient.

image. However, bone segmentation can be very challenging from clinical MR images as the bone structures in MR images is of low resolution. The bone surfaces segmented from MR images are often incomplete. Thus, it is not possible to generate FE meshes of bone structures with MR image using traditional surface based methods.

In our method, the patient MR images do not need to be segmented. The atlas image together with the smoothness constraints can serve as a shape prior to help define the boundary of the bone structures even if the information contained in the patient MR image is incomplete. From our experiments, we have shown that our multi-modal method can successfully generate FE meshes with bone structures, i.e., the face model with skull surface, directly from the patient MR images. The accuracy and quality of the generated mesh are satisfactory and quite close to the one generated using mono-modal registration.

6.5 Conclusion

The proposed patient-specific FE mesh generation scheme was quantitatively and qualitatively evaluated on three different clinical cases, involving synthetic, mono-modal and multi-modal image registration. The patient-specific finite element meshes were automatically generated for all the cases within 2 to 17 minutes, either with synthetic images or real CT and MR images. A detailed parameter study on how the registration parameters may affect both the generated mesh accuracy and mesh quality is also presented, which provides useful information for the application of this method.

The image based mesh morphing method introduced in this article improves

the previous surface or landmarks based mesh morphing technique by eliminating the tedious and time consuming segmentation step, and combining the segmentation and mesh morphing into a single procedure. This feature also makes the surface representation accuracy of the produced FE mesh dependent only on the patient image quality by eliminating possible surface representation errors stemming from an inaccurate segmentation.

Although some binary image registration based methods have been proposed recently (Barber *et al.*, 2007; Lamata *et al.*, 2011), little attention was paid to mesh quality preservation or restoration for the generated meshes as smooth, diffeomorphic, mesh deformation is not guaranteed in these methods. However, this is crucial especially for complex FE meshes with a large number of elements, such as the face model in our experiment. In our scheme, the diffeomorphic constraint and the smoothness term largely preserves the generated mesh from unwanted distortions. Both the femur and face model achieved very small mesh quality degradation (0.8% problematic elements and less than 2% change in each JR interval). Although image based mesh morphing registers more information than surface based mesh morphing, which could lead to more distortions, our method managed to obtain better mesh quality than the surface based method in Bucki *et al.* (2010), where the maximal change in each JR interval was 4.1% for the femur model and 6.8% for the face model. The small amount of problematic elements could successfully be repaired manually in commercial software or through an automatic reparation algorithm (Bucki *et al.*, 2011).

In the proposed scheme, the generated mesh quality and accuracy rely on the accurate definition of the atlas mesh. The representative error between the

atlas mesh and atlas image will be passed on to the patient meshes, i.e., patient mesh quality will be affected by the quality of the atlas mesh. Therefore if a high quality atlas mesh is used, high quality patient-specific FE meshes can be generated. The strong point is that this modeling effort only needs to be done once for each anatomy. Since the procedure is segmentation free, it significantly simplifies the FE mesh generation process and also offers the possibility of incremental atlas mesh enhancement that immediately translates into finer patient specific FE models with absolutely no effect on the complexity of the FE model generation procedure itself, as explained below. In surface/landmark based registration schemes, if a new feature needs to be modeled in the atlas mesh, it will also have to be segmented/pinpointed in every patient's dataset in order to be properly registered. Thus, the use of a more comprehensive/realistic atlas model involves heavier image processing of patient data through the required segmentation overhead. In our image based scheme model enhancement needs only to be done in the atlas image space and the subsequent patient models will automatically be updated with the new features, as long as the latter are clearly visible in the atlas images. New features added to the atlas only need to be segmented in atlas space and will automatically be available in patient space through the image registration process.

Another advantage of our method is that it can encode any similarity measure without customization of optimization method, which makes it convenient to extend our scheme to multi-modality registration, as in Section 6.4. This feature is of interest, since for an atlas mesh built on a certain image modality, for example a CT image, different patient image modalities can be used (CT or MRI). This give the clinicians more freedom to choose the appropriate image

modality for different patients, as certain image modalities may not be available for those patient. The shape information contain in one image modality along with the smoothness constraints in the registration scheme may also help to define the shape in another image modality, which is otherwise hard to obtain.

Chapter 7

Conclusion and Future Work

This chapter concludes the thesis and suggests several directions for future work. Section 7.1 summarizes the technical contributions achieved in this thesis. Section 7.2 proposes a few possible improvements that can be made to our current method.

7.1 Conclusion

The aim of our project is to develop a 3D image driven mesh morphing method, which can automatically generate patient-specific FE mesh from patient medical image. Our work mainly consists of two parts: (1) pre-processing of the MR image with the proposed robust anisotropic filtering framework, and (2) volume image registration based automatic FE mesh generation method.

In the pre-processing step, we proposed a robust AD filtering framework with automatic parameter value selection strategy for MR image denoising and enhancement. Different from traditional analytical methods (Black *et al.*, 1998; Perona & Malik, 1990; Samsonov & Johnson, 2004), we proposed to estimate the optimal parameter value of the AD filter through an optimization step on a

synthetic image model. The proposed approach was validated using both simulated and real MR images. The synthetic image model proposed in our scheme was shown to be highly suitable for the purpose of parameter optimization. The parameter values selected using the proposed method can give rise to results quite similar to traditional manually tuned parameters. From experiments on simulated MR images, we are also able to determine a proper decreasing rate for the dynamic parameters as well as the parameter search range. The experimental results on the simulated MR images confirm that our method outperforms most state-of-the-art MR image denoising methods (Aja-Fernández *et al.*, 2008; Krissian & Aja-Fernández, 2009; Manjón *et al.*, 2008) in both quantitative measurements and visual evaluation. By testing on real MR images of different organs with differently noise levels, we demonstrated that our method is sufficiently general to be applied to a variety of MR images.

In the FE mesh generation step, we proposed an image registration based mesh morphing method. Different from traditional mesh morphing method (Bucki *et al.*, 2010; Couteau *et al.*, 2000), which deforms the atlas FE mesh to presegmented patient organ surface or landmarks, we proposed to deform the atlas FE mesh according to the displacement field obtained by registering the atlas and patient images. The proposed scheme improves traditional automatic FE mesh generation methods by skipping the tedious and often difficult image segmentation step. Moreover, it makes the registration process independent of the atlas mesh structure, which allows the atlas to be gradually refined without altering the registration process. To reduce the distortion caused by the mesh deformation, a new smoothness term is also proposed in our scheme. The proposed scheme is implemented with an efficient optimization method which does not

need to be customized for different similarity metrics, thus makes it convenient to adapt our method to multi-modal imagery. By testing the proposed method on three diffident clinical cases involving synthetic, mono-modal, and multi-modal image registration, we demonstrated that our method is sufficiently general to be used in different clinical situations. Results show that the FE mesh generated using our method outperforms that of the state-of the-art surface based mesh morphing method (Bucki *et al.*, 2010) in both mesh representation accuracy and quality.

7.2 Future Work

From the aspect of experimental evaluation, quantitative evaluation of the bone representation accuracy on the multi-modality image registration based mesh morphing is needed for the face model in Section 6.4. This can be done by manual or semi-automatic segmentation of the skull surface from the MR head image.

A further improvement of the current method will be the integration of the mesh untangling step into the registration procedure itself, rather than a post-processing step that can possibly degrade surface accuracy. This could be achieved by formulating the FE mesh distortion measure as an energy term that further constrains mesh deformation to avoid excessive Jacobian Ratio (JR) degradations. In this way, an accurate patient-specific mesh could be generated from medical images in one step with no problematic elements, and can be directly used in finite element analysis.

In the proposed image registration based mesh morphing method, the atlas mesh deformation is driven by intensity information alone. This method can be

automatic and effective for organs with good contrast. However, when the organ of interest in the medical image lacks distinct boundary features, the patient's medical image alone cannot provide sufficient information to achieve an accurate atlas mesh deformation. For example, the boundary of the tongue in the MR image is difficult to identify as the intensity of the tongue is close to that of adjacent soft tissues. In model-based automatic image segmentation methods, this problem is often solved by incorporating information about prior knowledge of the shape and appearance of the organ of interest to restrict the deformation of the model in areas lacking image information (Heimann & Delingette, 2011). Minimal expert interventions can also be incorporated to increase the reliability of the segmentation (Stavness *et al.*, 2013). Thus, another possible extension of our method would be to investigate the possibility to incorporate the shape priors and user intervention into our mesh morphing scheme so that our method can also be used in patient's medical image with low contrast.

References

AHMED, M.N., YAMANY, S.M., MOHAMED, N., FARAG, A.A. & MORIARTY, T. (2002). A modified fuzzy c-means algorithm for bias field estimation and segmentation of MRI data. *IEEE Transactions on Image Processing*, **21**, 193–199. 53, 67

AJA-FERNÁNDEZ, S., SAN-JOSÉ-ESTÉPAR, R., ALBEROLA-LÓPEZ, C. & WESTIN, C.F. (2006). Image quality assessment based on local variance. In *28th IEEE EMBC*, 4815–4818, New York. 62

AJA-FERNÁNDEZ, S., LOPEZ, C.A. & WESTIN, C.F. (2008). Noise and signal estimation in magnitude MRI and Rician distribution images: A LMMSE approach. *IEEE Transactions on Image Processing*, **17**, 1383–1389. 46, 56, 61, 154

ASHBURNER, J. (2007). A fast diffeomorphic image registration algorithm. *Neuroimage*, **38**, 95–113. 41

ASHBURNER, J. & FRISTON, K.J. (1999). Nonlinear spatial normalization using basis functions. *Human brain mapping*, **7**, 254–266. 33

AVANTS, B.B., EPSTEIN, C.L., GROSSMAN, M. & GEE, J.C. (2008). Symmetric diffeomorphic image registration with cross-correlation: evaluating automated labeling of elderly and neurodegenerative brain. *Medical image analysis*, **12**, 26–41. 41

BALLESTER, G., ZISSERMAN, A. & BRADY, M. (1998). Measurement of brain structures based on statistical and geometrical 3d segmentation. In *Medical Image Computing and Computer-Assisted InterventationMICCAI98*, 499–508, Springer. 26

BARBER, D.C., OUBEL, E., FRANGI, A.F. & HOSE, D.R. (2007). Efficient computational fluid dynamics mesh generation by image registration. *Medical Image Analysis*, **11**, 648–662. 79, 150

BEG, M.F., MILLER, M.I., TROUVÉ, A. & YOUNES, L. (2005). Computing large deformation metric mappings via geodesic flows of diffeomorphisms. *International journal of computer vision*, **61**, 139–157. 41

BENZLEY, S.E., PERRY, E., MERKLEY, K., CLARK, B. & SJAARDEMA, G.D. (1995). A comparison of all hexagonal and all tetrahedral finite element meshes for elastic and elastoplastic analysis. In *4th International Meshing Roundtable*. 11

BLACK, M.J., SAPIRO, G., MARIMONT, D.H. & HEEGER, D. (1998). Robust anisotropic diffusion. *IEEE Transactions on Image Processing*, **7**, 421–432. 46, 61, 69, 73, 153

BUADES, A., COLL, B. & MOREL, J. (2005). A review of image denoising algorithms, with a new one. *SIAM Journal on Multiscale Modeling and Simulation*, **4**, 490–530. 61

BUCKI, M., LOBOS, C. & PAYAN, Y. (2010). A fast and robust patient specific finite element mesh registration technique: Application to 60 clinical cases. *Medical Image Analysis*, **14**, 303–317. xvii, xxi, 5, 12, 22, 23, 39, 80, 81, 87, 91, 107, 114, 116, 118, 130, 131, 132, 150, 154, 155

BUCKI, M., LOBOS, C., PAYAN, Y. & HITSCHFELD, N. (2011). Jacobian-based repair method for finite element meshes after registration. *Engineering with Computers*, **27**, 285–297. 91, 101, 141, 150

CACHIER, P., MANGIN, J.F., PENNEC, X., RIVIÈRE, D., PAPADOPOULOS-ORFANOS, D., RÉGIS, J. & AYACHE, N. (2001). Multisubject non-rigid registration of brain mri using intensity and geometric features. In *Medical Image Computing and Computer-Assisted Intervention–MICCAI 2001*, 734–742, Springer. 27

CANNY, J. (1986). A computational approach to edge detection. *IEEE Transactions on Pattern Analysis and Machine Intelligence*, **8**, 679–698. 45

CARTER, T.J., SERMESANT, M., CASH, D.M., BARRATT, D.C., TANNER, C. & HAWKES, D.J. (2005). Application of soft tissue modelling to image-guided surgery. *Medical Engineering & Physics*, **27**, 893909. 12

CASH, D.M. & MIGA, M.I. (2005). Compensating for intraoperative soft-tissue deformation using incomplete surface data and finite elements. *IEEE Transactions on Medical Imaging*, **24**, 1479–1491. 2, 12

CASTELLANO-SMITH, A.D., HARTKENS, T., SCHNABEL, J., HOSE, D.R., LIU, H., HALL, W.A., TRUWIT, C.L., HAWKES, D.J. & HILL, D.L.G. (2001). Constructing patient specific models for correcting intraoperative brain deformation. In *Medical Image Computing and Computer-Assisted Intervention*, vol. 2208, 1091–1098. 2

CATTÉ, F., LIONS, P.L., MOREL, J.M. *et al.* (1992). Image selective smoothing and edge detection by nonlinear diffusion. *SIAM Journal on Numerical Analysis.*, **29**, 182–193. 45, 46, 49

CHABANAS, M. & PAYAN, Y. (2000). A 3d finite element model of the face for simulation in plastic and maxillo-facial surgery. In *Medical Image Computing and Computer-Assisted Intervention–MICCAI 2000*, 1068–1075, Springer. 19

CHABANAS, M., LUBOZ, V. & PAYAN, Y. (2003). Patient specific finite element model of the face soft tissues for computer-assisted maxillofacial surgery. *Medical Image Analysis*, **7**, 131–151. xix, 2, 14, 19, 133

CHEN, M., KANADE, T., POMERLEAU, D. & SCHNEIDER, J. (1999). 3-d deformable registration of medical images using a statistical atlas. In *Medical Image Computing and Computer-Assisted Intervention–MICCAI99*, 621–630, Springer. 27

COCOSCO, C.A., KOLLOKIAN, V., KWAN, R.K.S., PIKE, G.B. & EVANS, A.C. (1997). Brainweb: Online interface to a 3D MRI simulated brain database. *NeuroImage*, **5**, 425. 59

COUTEAU, B., HOBATHO, M., DARMANA, R., BRIGNOLA, J. & ARLAUD, J. (1998). Finite element modelling of the vibrational behaviors of the human femur using ct based individualized geometrical and material properties. *Journal of Biomechanics*, **31**, 383–386. 123

COUTEAU, B., PAYAN, Y. & LAVALLÉE, S. (2000). The mesh-matching algorithm: An automatic 3D mesh generator for finite element structures. *Journal of Biomechanics*, **33**, 1005–1009. 22, 23, 154

CREANE, A., MAHER, E., SULTAN, S., HYNES, N., KELLY, D.J. & LALLY, C. (2010). Finite element modeling of diseased carotid bifurcations generated from in vivo computerised tomographic angiography. *Computers in Biology and Medicine*, **40**, 419–429. 21

CROUCH, J.R., PIZER, S.M., CHANEY, E.L., HU, Y., MAGERAS, G.S. & ZAIDER, M. (2007). Automated finite-element analysis for deformable registration of prostate images. *IEEE Transactions on Medical Imaging*, **26**, 1379–1390. 21

DELINGETTE, H. (1999). General object reconstruction based on simplex meshes. *International Journal of Computer Vision*, **32**, 111–146. 25, 26

FANG, Q. & BOAS, D.A. (2009). Tetrahedral mesh generation from volumetric binary and gray-scale images. In *ISBI'09 Proceedings of the 6th IEEE International Conference on Symposium on Biomedical Imaging: From Nano to Macro*, 1142–1145, Boston, MA. 20

FERNANDEZ, J.W., MITHRARATNE, P., THRUPP, S.F., TAWHAI, M.H. & HUNTER, P.J. (2004). Anatomically based geometric modelling of the

musculo-skeletal system and other organs. *Biomechanics and Modeling in Mechanobiology*, **2**, 139–155. 22

FERRANT, M., WARFIELD, S., NABAVI, A., JOLESZ, F. & KIKINIS, R. (2000). Registration of 3D intraoperative MR images of the brain using a finite element biomechanical model. vol. 1935/2000, 249–258. 20

FIELD, D.A. (2000). Qualitative measure for initial meshes. *International Journal for Numerical Methods in Engineering*, **47**, 887–906. 15, 17, 91

FOULONNEAU, A., CHARBONNIER, P. & HEITZ, F. (2009). Multi-reference shape priors for active contours. *International Journal of Computer Vision*, **81**, 68–81. 25

GEMAN, S. & GEMAN, D. (1984). Stochastic relaxation gibbs distributions and the bayesian restoration of images. *IEEE Transactions on Pattern Analysis and Machine Intelligence*, **6**, 721–741. 97

GERIG, G., KUBLER, O., KIKINIS, R. & JOLESZ, F.A. (1992). Nonlinear anisotropic filtering of MRI data. *IEEE Transactions on Medical Imaging*, **11**, 221–232. 44, 45

GLOCKER, B., KOMODAKIS, N., TZIRITAS, G., NAVAB, N. & PARAGIOS, N. (2008). Dense image registration through mrfs and efficient linear programming. *Medical Image Analysis*, **12**, 731–741. 39, 87, 89, 93, 94, 97, 98

GRAVEL, P., BEAUDOIN, G. & GUISE, J.A. (2004). A method for modeling noise in medical images. *IEEE Transactions on Image Processing*, **23**, 1221–1232. 56

GUDBJARTSSON, H. & PATZ, S. (1995). The Rician distribution of noisy MRI data. *Magnetic Resonance in Medicine*, **34**, 910–914. 31, 56

GUIMOND, A., ROCHE, A., AYACHE, N. & MEUNIER, J. (2001). Three-dimensional multimodal brain warping using the demons algorithm and adaptive intensity corrections. *Medical Imaging, IEEE Transactions on*, **20**, 58–69. 27

HAJNAL, J.V. & HILL, D.L.G. (2010). *Medical image registration*. CRC press. 32

HAJNAL, J.V., SAEED, N., SOAR, E.J., OATRIDGE, A., YOUNG, I.R. & BYDDER, G.M. (1995). A registration and interpolation procedure for subvoxel matching of serially acquired mr images. *Journal of computer assisted tomography*, **19**, 289–296. 33

HEIMANN, T. & DELINGETTE, H. (2011). Model-based segmentation. In *Biomedical Image Processing*, 279–303, Springer. 156

HELLIER, P., BARILLOT, C., COROUGE, I., GIBAUD, B., GOUALHER, G.L., COLLINS, L., EVANS, A., MALANDAIN, G. & AYACHE, N. (2001). Retrospective evaluation of inter-subject brain registration. In *Medical Image Computing and Computer-Assisted Intervention*, 258–265. 27, 79

HERBULOT, A., JEHAN-BESSON, S., DUFFNER, S., BARLAUD, M. & AUBERT, G. (2006). Segmentation of vectorial image features using shape gradients and information measures. *Journal of Mathematical Imaging and Vision*, **25**, 365–386. 25

HERNANDEZ, M., BOSSA, M.N. & OLMOS, S. (2007). Registration of anatomical images using geodesic paths of diffeomorphisms parameterized with stationary vector fields. In *Computer Vision, 2007. ICCV 2007. IEEE 11th International Conference on*, 1–8, IEEE. 41

HILL, D.L., STUDHOLME, C. & HAWKES, D.J. (1994). Voxel similarity measures for automated image registration. In *Visualization in Biomedical Computing 1994*, 205–216, International Society for Optics and Photonics. 35, 36

HUGHES, T. (1987). *The Finite Element Method: Linear Static and Dynamic Finite Element Analysis*. Dover Publications. 11

JI, S., FORD, J.C., GREENWALD, R.M., BECKWITH, J.G., PAULSEN, K.D., FLASHMAN, L.A. & MCALLISTER, T.W. (2011). Automated subject-specific, hexahedral mesh generation via image registration. *Finite Elements in Analysis and Design*, **47**, 1178–1185. 24

KASS, M., WITKIN, A. & TERZOPOULOS, D. (1988). Snakes: Active contour models. *International journal of computer vision*, **1**, 321–331. 26

KELLY, S. (1998). Element shape testing. In *Ansys Theory Reference, Chap 13*, Ansys, USA. 101, 103

KERCKHOFFS, R.C.P., MCCULLOCH, A.D., OMENS, J.H. & MULLIGAN, L.J. (2009). Effects of biventricular pacing and scar size in a computational model of the failing heart with left bundle branch block. *Medical Image Analysis*, **13**, 362369. 11

KEYAK, J.H., MEAGHER, J.M., SKINNER, H.B. & MOTE, C.D. (1990). Automated three-dimensional finite element modeling of bone: A new method. *Journal of Biomedical Engineering*, **12**, 389–397. 20

KLEIN, S., STARING, M. & PLUIM, J.P.W. (2007). Evaluation of optimization methods for nonrigid medical image registration using mutual information and b-splines. *IEEE Transactions on Image Processing*, **16**, 2879–2890. 93

KNUPP, P. (2000a). Achieving finite element mesh quality via optimization of the jacobian matrix norm and associated quantities. ii - a framework for volume mesh optimization and the condition number of the jacobian matrix. *International Journal of for Numerical Methods in Engineering*, **48**, 1165–1185. 100, 101

KNUPP, P. (2000b). Hexahedral mesh untangling & algebraic mesh quality metrics. In *9th International Meshing Roundtable*, 173–183. 15

KOMODAKIS, N., TZIRITAS, G. & PARAGIOS, N. (2007). Fast, approximately optimal solutions for single and dynamic mrfs. *IEEE Computer Vision and Pattern Recognition Conference*, 18. 87, 94, 97

KOSIOR, J.C., KOSIOR, R.K. & FRAYNE, R. (2007). Robust dynamic susceptibility contrast MR perfusion using 4D nonlinear noise filters. *Journal of Magnetic Resonance Imaging*, **26**, 1514–1522. 44

KRISSIAN, K. & AJA-FERNÁNDEZ, S. (2009). Noise-driven anisotropic diffusion filtering of MRI. *IEEE Transactions on Image Processing*, **18**, 2265–2274. 46, 61, 66, 154

KWOK, W. & CHEN, Z. (2000). A simple and effective mesh quality metric for hexahedral and wedge elements. In *9th International Meshing Roundtable*. 15, 17, 91

LAMATA, P., NIEDERER, S., NORDSLETTEN, D., BARBER, D.C., ROY, I. & HOSE, D.R. (2011). An accurate, fast and robust method to generate patient-specific cubic hermite meshes. *Medical Image Analysis*, **15**, 801–813. 79, 100, 121, 150

LEDERMAN, C., JOSHI, A., DINOV, I., VESE, L., TOGA, A. & HORN, J.D.V. (2011). The generation of tetrahedral mesh models for neuroanatomical MRI. *NeuroImage*, **55**, 153–164. 20

LENGSFELD, M., BURCHARD, R., GUNTHER, D., PRESSEL, T., SCHMITT, J., LEPPEK, R. & GRISS, P. (2005). Femoral strain changes after total hip arthroplasty - patient-specific finite element analyses 12 years after operation. *Medical Engineering and Physics*, **27**, 649–654. 2

LEVENTON, M.E., GRIMSON, W.E.L. & FAUGERAS, O. (2000). Statistical shape influence in geodesic active contours. In *Computer Vision and Pattern Recognition, 2000. Proceedings. IEEE Conference on*, vol. 1, 316–323, IEEE. 25

LI, C. & SUN, Y. (2009). Nonrigid registration of myocardial perfusion MRI using pseudo ground truth. In *Medical Image Computing and Computer-Assisted Intervention*, vol. 5242, 165–172. 27, 79

LI, S.Z. (2001). *Markov Random Field Modeling In Image Analysis*. Springer Verlag Inc. 97

LI, X. & CHEN, T. (1994). Nonlinear diffusion with multiple edginess thresholds. *Pattern Recognition*, **27**, 1029–1037. 50, 51, 52

LOBOS, C., BUCKI, M., HITSCHFELD, N. & PAYAN, Y. (2007). Mixed-element mesh for an intra-operative modeling of the brain tumor extraction. In *16th International Meshing Roundtable*, Sandia National Laboratories, Springer, New York. 17

LORENZO-VALDÉS, M., SANCHEZ-ORTIZ, G.I., MOHIADDIN, R. & RUECKERT, D. (2002). Atlas-based segmentation and tracking of 3d cardiac mr images using non-rigid registration. In *Medical Image Computing and Computer-Assisted InterventionMICCAI 2002*, 642–650, Springer. 27

LUBOZ, V., PEDRONO, A., AMBARD, D., BOUTAULT, F., PAYAN, Y. & SWIDER, P. (2004). Prediction of tissue decompression in orbital surgery. *Clinical Biomechanics*, **19**, 202–208. 19

LUBOZ, V., CHABANAS, M., SWIDER, P. & PAYAN, Y. (2005). Orbital and maxillofacial computer aided surgery: Patient-specific finite element models to predict surgical outcomes. *Computer Methods in Biomechanics and Biomedical Engineering*, **8**, 259–265. 2, 15, 91, 133

MAES, F., COLLIGNON, A., VANDERMEULEN, D., MARCHAL, G. & SUETENS, P. (1997). Multimodality image registration by maximization of mutual information. *Medical Imaging, IEEE Transactions on*, **16**, 187–198. 36

MAINTZ, J.B.. & VIERGEVER, M.A. (1998). A survey of medical image registration. *Medical image analysis*, **2**, 1–36. 32

MALLADI, R., SETHIAN, J.A. & VEMURI, B.C. (1995). Shape modeling with front propagation: A level set approach. *Pattern Analysis and Machine Intelligence, IEEE Transactions on*, **17**, 158–175. 26

MANJÓN, J.V., CARBONELL-CABALLERO, J., LULL, J.J., GARCIA-MARTI, G., MARTI-BONMATI, L. & ROBLES, M. (2008). MRI denoising using non-local means. *Medical Image Analysis*, **12**, 514–523. 44, 45, 61, 154

MARR, D. & HILDRETH, E. (1980). Theory of edge detection. In *Proceedings of the Royal Society B*, 187–217. 49

MATTES, D., HAYNOR, D.R., VESSELLE, H., LEWELLYN, T.K. & EUBANK, W. (2001). Nonrigid multimodality image registration. In *Medical Imaging 2001: Image Processing*, San Diego, CA. 145

MENET, S., SAINT-MARC, P. & MEDIONI, G. (1990). B-snakes: Implementation and application to stereo. In *proceedings DARPA*, vol. 720, 726. 26

MIGA, M.I., PAULSEN, K.D., KENNEDY, F.E., HARTOV, A. & ROBERTS, D.W. (1999). Model-updated image-guided neurosurgery using the finite ele-

ment method: Incorporation of the falx cerebri. In *Medical Image Computing and Computer-Assisted Intervention*, vol. 1679, 900–909. 15

MOHAMED, A. & DAVATZIKOS, C. (2004). Finite element mesh generation and remeshing from segmented medical images. In *ISBI'04 Proceedings of the 6th IEEE International Conference on Symposium on Biomedical Imaging: From Nano to Macro*, vol. 1, 420–423. 20

MOLINA, N., BRIDSON, R., TERAN, J. & FEDKIW, R. (2003). A crystalline, red green strategy for meshing highly deformable objects with tetrahedra. In *12th International Meshing Roundtable*, Santa Fe, New Mexico, USA. 20

MONTAGNAT, J. & DELINGETTE, H. (1997). Volumetric medical images segmentation using shape constrained deformable models. In *CVRMed-MRCAS'97*, 13–22, Springer. 26

MONTAGNAT, J. & DELINGETTE, H. (2005). 4d deformable models with temporal constraints: application to 4d cardiac image segmentation. *Medical Image Analysis*, **9**, 87–100. 25

MONTAGNAT, J., DELINGETTE, H. & MALANDAIN, G. (1999). Cylindrical echocardiographic image segmentation based on 3d deformable models. In *Medical Image Computing and Computer-Assisted Intervention–MICCAI99*, 168–175, Springer. 25

MONTEIL, J. & BEGHDADI, A. (1999). A new interpretation and improvement of the nonlinear anisotropic diffusion for image enhancement. *IEEE Transactions on Pattern Analysis and Machine Intelligence*, **21**, 940–946. 45

MYRONENKO, A. & SONG, X. (2009). Image registration by minimization of residual complexity. In *Computer Vision and Pattern Recognition, 2009. CVPR 2009. IEEE Conference on*, 49–56, IEEE. 37

NAZARI, M., PAYAN, Y., PERRIER, P., CHABANAS, M. & LOBOS, C. (2008). A continuous biomechanical model of the face: A study of muscle coordinations for speech lip gestures. In *8th International Seminar on Speech Porduction*, Strasbourg, France. 19, 133

NIEDERER, S.A., PLANK, G., CHINCHAPATNAM, P., GINKS, M., LAMATA, P., RHODE, K.S., RINALDI, C.A., RAZAVI, R. & SMITH, N.P. (2010). Length-dependent tension in the failing heart and the efficacy of cardiac resynchronization therapy. *Cardiovascular Research*, **89**, 336–343. 11

NOWAK, R. (1999). Wavelet-based Rician noise removal for magnetic resonance imaging. *IEEE Transactions on Image Processing*, **8**, 1408–1419. 56, 57

OSHER, S. & SETHIAN, J.A. (1988). Fronts propagating with curvature-dependent speed: algorithms based on hamilton-jacobi formulations. *Journal of computational physics*, **79**, 12–49. 26

PATIL, S. & RAVI, B. (2005). Voxel-based representation, display and thickness analysis of intricate shapes. In *Ninth International Conference on Computer Aided Design and Computer Graphics*, Hong Kong. 123

PERONA, P. & MALIK, J. (1990). Scale-space and edge detection using anisotropic diffusion. *IEEE Transactions on Pattern Analysis and Machine Intelligence*, **12**, 629–639. 44, 45, 46, 48, 49, 61, 153

PETERSSON, K.M., NICHOLS, T.E., POLINE, J.B. & HOLMES, A.P. (1999). Statistical limitations in functional neuroimaging. *Philosophical Transactions of the Royal Society B*, **354**, 1261–1281. 44

ROBERT, D. & NOWAK (1999). Wavelet-based Rician noise removal for magnetic resonance imaging. *IEEE Transactions on Image Processing*, **8**, 629–639. 44

ROHLFING, T. & JR, C.R.M. (2001). Intensity-based non-rigid registration using adaptive multilevel free-form deformation with an incompressibility constraint. In *Medical Image Computing and Computer-Assisted Intervention–MICCAI 2001*, 111–119, Springer. 39

RUECKERT, D., SONODA, L.I., HAYES, C., HILL, D.L.G., LEACH, M.O. & HAWKES, D.J. (1999). Nonrigid registration using free-form deformations: Application to breast MR images. *IEEE Transactions on Image Processing*, **18**, 712–721. 28, 38, 93

RUECKERT, D., FRANGI, A.F. & SCHNABEL, J.A. (2001). Automatic construction of 3D statistical deformation models using non-rigid registration. In *Medical Image Computing and Computer-Assisted Intervention*, vol. 2008, 77–84. 27, 79

RUECKERT, D., ALIJABAR, P., HECKEMANN, R.A., HAJNAL, J.V. & HAMMERS, A. (2006). Diffeomorphic registration using b-splines. In *Medical Image Computing and Computer-Assisted Intervention*, vol. 4191, 702–709. 39, 87, 91, 92

SAITO, T. & TORIWAKI, J.I. (1994). New algorithms for euclidean distance transformation of an n-dimensional digitized picture with applications. *Pattern recognition*, **27**, 1551–1565. 111

SAMSONOV, A.A. & JOHNSON, C.R. (2004). Noise-adaptive nonlinear diffusion filtering of MR images with spatially varying noise levels. *Magnetic Resonance in Medicine*, **52**, 798–806. 46, 61, 153

SCHNABEL, J.A., RUECKERT, D., QUIST, M., BLACKALL, J.M., CASTELLANO-SMITH, A.D., HARTKENS, T., PENNEY, G.P., HALL, W.A., LIU, H. & TRUWIT, C.L. (2001). A generic framework for non-rigid registration based on non-uniform multi-level free-form deformations. In *Medical Image Computing and Computer-Assisted Intervention–MICCAI 2001*, 573–581, Springer. 38

SHANNON, C.E. (1949). Communication in the presence of noise. *Proceedings of the IRE*, **37**, 10–21. 34

SHEN, J.K., MATUSZEWSKI, B.J. & SHARK, L.K. (2005). Deformable image registration. In *Image Processing, 2005. ICIP 2005. IEEE International Conference on*, vol. 3, III–1112, IEEE. 32

SHEWCHUK, J. (2002). What is a good linear element? interpolation, conditioning, and quality measures. In *11th International Meshing Roundtable*, Sandia National Laboratories. 15, 17, 91

SHIM, V.B., PITTO, R.P., STREICHER, R.M., HUNTER, P.J. & ANDERSON, I.A. (2007). The use of sparse CT datasets for auto-generating accurate fe models of the femur and pelvis. *Journal of Biomechanics*, **40**, 26–35. 21

SIGAL, I.A., HARDISTY, M.R. & WHYNE, C.M. (2008). Mesh-morphing algorithms for specimen-specific finite element modeling. *Journal of Biomechanics*, **41**, 1381–1389. 22, 23

STAVNESS, I., NAZARI, M., PERRIER, P., DEMOLIN, D. & PAYAN, Y. (2013). Biomechanical modeling study of the effects of the orbicularis oris muscle and jaw posture on lip shape. *Journal of Speech, Language, and Hearing Research*, **56**, 878–890. 156

STUDHOLME, C., HILL, D.L.G. & HAWKES, D.J. (1999). An overlap invariant entropy measure of 3d medical image alignment. *Pattern Recognition*, **32**, 71–86. 37, 89, 90

TADDEI, F., PANCANTI, A. & VICECONTI, M. (2004). An improved method for the automatic mapping of computed tomography numbers onto finite element models. *Medical Engineering & Physics*, **26**, 61–69. 18

THEVENAZ, P. & UNSER, M. (2000). Optimization of mutual information for multiresolution image registration. *IEEE Transactions on Image Processing*, **9**, 2083–2099. 145

THIRION, J.P. (1998). Image matching as a diffusion process: an analogy with maxwell's demons. *Medical image analysis*, **2**, 243–260. 28, 39, 40

TSAI, A., YEZZI, J.A., WELLS, W., TEMPANY, C., TUCKER, D., FAN, A., GRIMSON, W.E. & WILLSKY, A. (2003). A shape-based approach to the segmentation of medical imagery using level sets. *Medical Imaging, IEEE Transactions on*, **22**, 137–154. 25

VERCAUTEREN, T., PENNEC, X., PERCHANT, A. & AYACHE, N. (2009). Diffeomorphic demons: Efficient non-parametric image registration. *NeuroImage*, **45**, S61–S72. 40, 87

VICECONTI, M., DAVINELLI, M., TADDEI, F. & CAPPELLO, A. (2004). Automatic generation of accurate subject-specific bone finite element models to be used in clinical studies. *Journal of Biomechanics*, **37**, 1597–1605. 21

WANG, H., DONG, L., O'DANIEL, J., MOHAN, R., GARDEN, A.S., ANG, K.K., KUBAN, D.A., BONNEN, M., CHANG, J.Y. & CHEUNG, R. (2005). Validation of an accelerated'demons' algorithm for deformable image registration in radiation therapy. *Physics in Medicine and Biology*, **50**, 2887. 40

WANG, V.Y., LAM, H.I., ENNIS, D.B., COWAN, B.R., YOUNG, A.A. & NASH, M.P. (2009). Modelling passive diastolic mechanics with quantitative mri of cardiac structure and function. *Medical Image Analysis*, **13**, 773784. 11

WANG, Z., BOVIK, A.C., SHEIKH, H.R. & SIMONCELLI, E.P. (2004). Image quality assessment: From error visibility to structural similarity. *IEEE Transactions on Image Processing*, **13**, 600–612. 62

WEATHERHILL, N.P. & HASSAN, O. (1994). Efficient three-dimensional delaunay triangulation with automatic point creation and imposed boundary constraints. *International Journal of Numerical Methods in Engineering*, **37**, 2005–2039. 20

WEI, D., SUN, Y., CHAI, P., LOW, A. & ONG, S.H. (2011). Myocardial segmentation of late gadolinium enhanced mr images by propagation of contours

from cine mr images. In *Medical Image Computing and Computer-Assisted Intervention–MICCAI 2011*, 428–435, Springer. 27

WEICKERT, J. (1998). *Anisotropic Diffusion in Image Processing*. ECMI Series, Teubner-Verlag, Stuttgart, Germany. 50

WELLS, W.M., VIOLA, P., ATSUMI, H., NAKAJIMA, S. & KIKINIS, R. (1996). Multi-modal volume registration by maximization of mutual information. *Medical image analysis*, **1**, 35–51. 36

WHITACKER, R.T. & PIZER, S.M. (1993). A multi-scale approach to nonuniform diffusion. *CVGIP: Image Understanding*, **57**, 99–110. 50, 51

WITKIN, A.P. (1983). Scale-space filtering. In *Proceedings of the 8th International Joint Cconference on Artificial Intelligence*, 1019–1022, Karlsruhe. 48

WITTEK, A., MILLER, K., KIKINIS, R. & WARFIELD, S.K. (2007). Patient-specific model of brain deformation: Application to medical image registration. *Journal of Biomechanics*, **40**, 919–929. 14, 19

WU, M.J., CARMICHAEL, O., LOPEZ-GARCIA, P., CARTER, C.S. & AIZENSTEIN, H.J. (2006). Quantitative comparison of AIR, SPM, and the fully deformable model for atlas-based segmentation of functional and structural MR images. *Human Brain Mapping*, **27**, 747–754. 27, 79

YOSIBASH, Z., PADAN, R., JOSKOWICZ, L. & MILGROM, C. (2007). A ct-based high-order finite element analysis of the human proximal femur com-

pared to in-vitro experiments. *Journal of Biomechanical Engineering*, **129**, 297–309. 12

ZALZAL, P., PAPINI, M., BACKSTEIN, D. & GROSS, A.E. (2008). Anterior femoral notching during total knee arthroplasty: A finite element analysis. *Journal of Bone and Joint Surgery*, **British 90-B**. 2, 122

ZHANG, Y., BAJAJ, C. & SOHN, B.S. (2005). 3D finite element meshing from imaging data. *Computer Methods in Applied Mechanics and Engineering*, **194**, 5083–5106. 20

ZHANG, Y., HUGHES, T. & BAJAJ, C. (2008). Automatic 3D mesh generation for a domain with multiple materials. In *16th International Meshing Roundtable*. 20

ZHU, C., BYRD, R.H., LU, P. & NOCEDAL, J. (1997). Algorithm 778: L-bfgs-b: Fortran subroutines for large-scale bound-constrained optimization. *ACM Transactions on Mathematical Software (TOMS)*, **23**, 550–560. 111

ZHUANG, X., HAWKESA, D.J., CRUMA, W.R., BOUBERTAKH, R., URIBE, S., ATKINSON, D., BATCHELOR, P., SCHAEFFTER, T., RAZAVI, R. & HILL, D.L.G. (2008a). Robust registration between cardiac MRI images and atlas for segmentation propagation. In *Proceedings of SPIE*, vol. 6914. 27, 79

ZHUANG, X., RHODE, K., ARRIDGE, S., RAZAVI, R., HILL, D., HAWKES, D. & OURSELIN, S. (2008b). An atlas-based segmentation propagation framework using locally affine registration-application to automatic whole heart segmentation. In *Medical Image Computing and Computer-Assisted Intervention*, vol. 5242, 425–433. 27, 79

ZIENKIEWICZ, O. & TAYLOR, R. (2000). *The Finite Element Method: The Basics, fifth ed.*. Butterworth-Heinemann, Oxford, UK. 11

ZIENKIEWICZ, O.C. & TAYLOR, R.L. (1989). *The Finite Element Method. Basic Formulation and Linear Problems*. MacGraw-Hill, Maidenhead, UK. 15

PUBLICATION LIST

Publication List

[1] TONG C., SUN Y., PAYET N. & ONG S.H. (2012). A General Strategy for Anisotropic Diffusion in MR Image Denoising and Enhancement. *Magnetic Resonance Imaging*, **30**, 1381–1393.

[2] TONG C., BUCKI M., ONG S.H. & PAYAN Y. (2013). Patient-Specific Finite Element Mesh Generation Based on Volume Image Registration. *Medical Image Analysis*, **Under review**.